Dynamics of Electrons and Excitons in Nanoclusters and Molecules Studied by Many-Body Green's Function Theory

by

Yi He

Submitted to the Department of Mechanical Engineering
in partial fulfillment of the requirements for the degree of

Doctor of Philosophy in Mechanical Engineering

at the

MASSACHUSETTS INSTITUTE OF TECHNOLOGY

February 2012

Author .....
Department of Mechanical Engineering
Jan 31, 2012

Certified by .....
Taofang Zeng
Principal Research Scientist
Thesis Supervisor

Accepted by .....
David E. Hardt
Chairman, Department Committee on Graduate Theses

Dynamics of Electrons and Excitons in Nanoclusters and Molecules Studied by Many-Body Green's Function Theory

by

Yi He

Submitted to the Department of Mechanical Engineering
on Jan 31, 2012, in partial fulfillment of the
requirements for the degree of
Doctor of Philosophy

Abstract

The development of efficient and economic photovoltaic (PV) systems harvesting solar energy is one of the grand challenges for engineering and scientific researchers. The theoretical conversion limit of a single-junction solar cell is 31% according to Shockley and Queisser (SQ), which the most advanced single-junction PV devices are approaching. Thus it is important to develop new methods and devices that can exceed the SQ limit. An economic strategy that may potentially break the SQ limit is to make use of the unique properties of semiconductor nanoclusters to fabricate PV devices.

The physics of semiconductor nanoclusters such as the dynamics of electrons and excitons are the fundamentals for fabricating nanocluster-based PV devices. Although the theories and numerical approaches have been long established for three-dimensional (3D) bulk materials, two-dimensional (2D) graphene-like structures and one-dimensional (1D) nanotubes, the computational methods for zero-dimensional (0D) finite systems based on the most advanced physical theory are not well established.

In the thesis, the computational approaches and methods based on the many-body Green's function theory are developed for 0D nanoclusters and molecules. The numerical implementations for the calculation of electronic inelastic scattering rates in nanoclusters are established. An efficient computational approach for the calculation of excitonic inelastic scattering rates in nanoclusters is also developed. Both the single-phonon and the multiple-phonon nonradiative relaxation mechanisms in nanoclusters are investigated. It is demonstrated that the nonradiative relaxation of one-particle states and two-particle states are distinctive due to the difference between the density-of-states of one-particle states and two-particle states.

Based on the numerical method established in the thesis, a strategy is proposed to reduce the electron-phonon coupling in nanoclusters by pushing valence electron away from nuclei with core electrons in heavy atoms, which is demonstrated with the lead chalcogenide nanoclusters, and porphyrin molecule and a porphyrin derivative.

Acknowledgments

Completion of a doctoral dissertation is like a marathon journey. I would not have completed my PhD thesis without kind help from people around me.

First, I would like to express my deepest gratitude to my advisor, Prof. Taofang Zeng, to provide me a great opportunity to study at MIT. With his continued support, encouragement and guidance, he helps me move forward with my research.

Next, I would like to thank my thesis committee members, Prof. Mildred Dresselhaus, Prof. Marc Baldo, Prof. Gang Chen and Prof. Nicolas Hadjiconstantinou. I am particularly grateful to Prof. Dresselhaus for her invaluable advices and suggestions, which substantially improved my thesis. Help and support of other thesis committee members are very important, and I really appreciate insightful comments from Prof. Baldo, Prof. Chen and Prof. Hadjiconstantinou. Also, I am very grateful to Prof. Patrick Lee for the inspiring discussion about the model used in the thesis.

Finally, I am particularly indebted to my wife, Tao, my parents and father in law for their support, understanding and encouragement in my hard times. It is their confidence in me that has given me courage and strength to complete the thesis.

Contents

List of Figures

Chapter 1

Introduction

1.1 Dynamics of Electrons and Excitons in Nanostructures

The development of efficient and economic photovoltaic (PV) systems harvesting solar energy is one of the grand challenges for engineering and scientific researchers.[1-3] The mechanism of a general single-junction semiconductor PV device is schematically illustrated in Fig. 1-1, where an absorbed photon produces an electron-hole pair. The electron-hole pair then relaxes to the edges of the conduction band and the valence band, separates at the heterojunction, and generates a usable photovoltage. The theoretical conversion limit for this type of solar cell is 31% according to Shockley and Queisser (SQ).[4] In other words, 69% of solar energy is lost. There are several pathways for the energy loss. One is from the incident photons with energy larger than the bandgap of the semiconductor, where extra photon energy is converted to heat through the non-radiative electron-phonon interaction as shown in Fig. 1-1. Another pathway is through the low-energy photons in the sunlight. These photons do not have sufficient energy to promote electrons to the conduction band, and they merely pass through (or even worse, heat up) the device. These two pathways account for the majority of the energy loss of the incoming solar energy. A small fraction of the energy loss is from the direct recombination of the electron-hole pair before the pair is separated at the heterojunction.

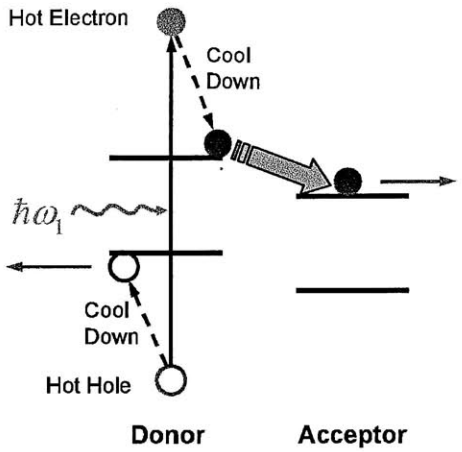

Figure 1-1. Mechanism of a general single-junction semiconductor PV device.

The currently best single-junction PV devices are approaching the SQ limit,[5] and thus it is necessary to develop new methods and devices that can exceed the limit of the single-junction. Some new concepts have been proposed. Most of these new concepts aim at the reduction of the energy loss during the electron and hole relaxation processes as shown in Fig. 1-1. An approach to enhance the efficiency beyond the SQ limit is to build a stack of multiple junctions with compensated bandgaps.[6] The theoretical limit for a PV device with infinite junctions is predicted to be 66%.[7] However, the manufacturing of multiple junctions usually requires expensive CVD processes. Thus tandem cells are used only in extreme situations where the power-to-weight ratio is the major concern.

Another strategy for enhancing PV efficiency is to take advantage of the unique properties of semiconductor nanoclusters to fabricate PV devices, whose efficiencies can potentially break the SQ limit, with economic production costs. The underlying mechanism of the semiconductor nanocluster-based solar cells is to utilize the energy of the hot carriers before these carriers relax to the band edges. If a hot carrier can be extracted from the donor to the acceptor before its thermalization, the photovoltage can be potentially enhanced (Fig. 1-2a).[8,9] Alternatively, when a hot carrier can promote another electron from the valence band to the conduction band through a reverse Auger process, the photocurrent can be increased (Fig. 1-2b).[10,11] The latter is

also known as the multiple exciton generation (MEG) process. If all photons with energies larger than twice of the bandgap generate two excitons, the theoretical limit will be 45%,[7] instead of the SQ limit of 31%.

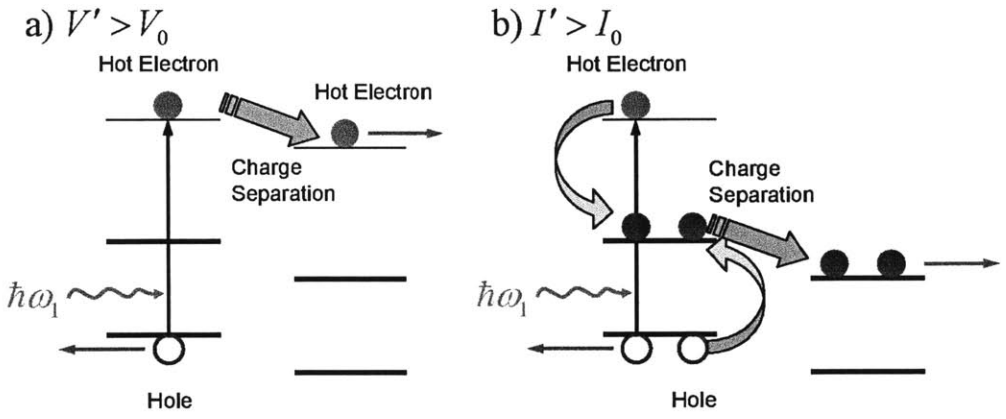

Figure 1-2. Two schemes to exceed the QF limit: a) hot electron capture for enhancing photovoltage and b) multiple exciton generation for enhancing photocurrent.

For understanding the hot electron capture and multiple exciton generation processes, an analogy can be made between a semiconductor nanostructure composed of electrons and nuclei and a simple heat engine composed of a working fluid and a cylinder/piston setup. As shown in Fig. 1-3a, electrons flow through the external circuit and do some useful electrical work due to the driving force (incident photons). Their role is exactly the same as the working fluid pushing the piston of the heat engine as shown in Fig. 1-3b. On the other hand, nuclei are necessary to hold those electrons, which are similar to the cylinder containing the working fluid.

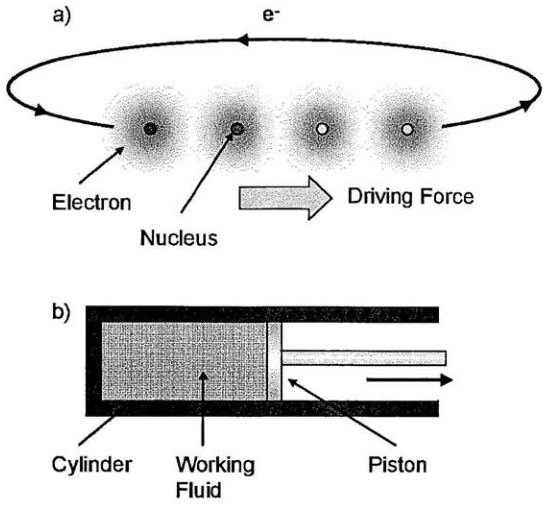

Figure 1-3. Schematic plots of a) a semiconductor nanostructure composed of electrons and nuclei and b) a simple heat engine composed of a working fluid and a cylinder/piston setup.

With the analogy above, the conventional single-junction photovoltaic devices in Fig. 1-1 are equivalent to a diabatic heat engine as shown in Fig. 1-4a, where the cylinder temperature is T_0 and the working fluid always cools down to this temperature via a fast heat exchange with the cylinder before it pushes the piston and does some useful mechanical work. The hot-electron capture mechanism in Fig. 1-2a is equivalent to a heat engine, as shown in Fig. 1-4b, where the heat exchange rate between the working fluid and the cylinder is small, so that the working fluid is allowed to push the piston before its complete cooling to T_0. More useful work can be extracted in this way due to a higher working pressure. The multiple exciton generation mechanism is equivalent to a heat engine as shown in Fig. 1-4c, where the working fluid is not allowed to push the piston before its temperature cools down to T_0, as in the case of Fig. 1-4a. However, the working fluid molecules can cool down through a decomposition reaction, which produces more independent molecules and outputs more mechanical work with increased volume.

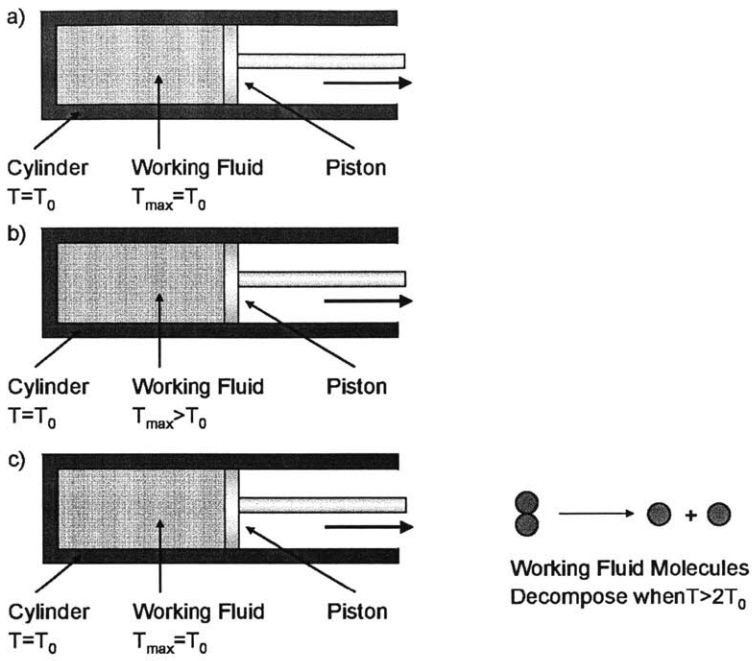

Figure 1-4. Heat engine analogies of a) conventional single-junction photovoltaic devices, b) the hot-electron capture mechanism and c) the multiple exciton generation mechanism. In each case the same process is involved.

To design a good heat engine, both the proper properties of the working fluid and of the thermal interaction between the working fluid and the cylinder/piston setup are required. The same fundamentals are applicable to the development of an efficient electricity generator based on semiconductor nanostructures. The difference between the two systems is that, for the semiconductor nanostructures the liquid/gas working fluid and the cylinder/piston setup are replaced by the "electron sea" and various nuclei, which demonstrate strong quantum effects and can only be investigated appropriately by quantum mechanics. Although the quantum theories and numerical approaches for 3D, 2D and 1D materials have been long established, computations based on quantum theories for 0D nanoclusters are relatively scarce. In some cases, even the basic computational methods are missing. With the wider applications of nanoclusters and the growing interest in semiconductor nanoclusters, it becomes very important to build up a comprehensive computational and theoretical tool kit for two important physical processes in nanoclusters, namely the dynamic properties of electrons/holes (the working fluid) and the interaction between electrons/holes with

their environment - phonons (or the interaction between the working fluid and the cylinder/piston setup).

There is only one fluid, namely the electron sea, which can be used as the energy carrier. However, we do have different working fluids as the electrons behave quite differently when they are excited in different ways. One possible way is to add an electron to the system, or remove an electron from a multi-electron system. These correspond to electron or hole excitations, also known as quasiparticle or one-particle excitations. Another possible way is to promote an electron from the valence band to the conduction band, which leads to an electron-hole pair with a coulomb interaction between them. This state is known as an excitonic excitation. A collective oscillation mode of a multi-electron system is also possible, which corresponds to a plasmon excitation.

1.2 Objective of the thesis

In this doctoral thesis, most efforts are focused on the excitonic excitation, as it is the media between the energy input (photons) and the energy output (electricity), which plays the same role as the working fluid in the heat engine. More specifically, we will study the dynamics of excitonic states, including how fast an exciton can spontaneously split into two excitons through inelastic scattering, and how fast an exciton can exchange energy with phonons through nonradiative relaxation. The heat engine equivalent is shown in Fig. 1-4c.

It should be emphasized that an exciton excitation can be understood more readily as the combination of two one-particle excitations. More importantly, the theories and numerical simulations of excitonic states have to be built up based on those of one-particle states. Therefore, this thesis will also cover the dynamics of the one-particle excitation, although this type of excitation is rarely utilized in electricity generation.

The purpose of the doctoral thesis is to integrate the state-of-the-art theoretical approaches and to develop new theoretical and computational strategies based on the many-body Green's function theory and perturbation theory. The approaches developed will be applied to the quantitative investigation of the dynamics of electrons and excitons in nanoclusters and molecules.

There are several reasons motivating us to develop such a comprehensive took kit for the subject:

1. Although electronic energies in finite systems (0D materials without periodic boundary conditions) have been studied intensively, efforts to investigate electronic dynamics, i.e. inelastic scattering rates are rare. Until the work of this thesis, a well recognized strategy for the calculation is very difficult to find.
2. Theoretical works on the dynamics of excitons in finite systems, i.e. inelastic scattering rates of excitons in 0D materials have not been reported. No literatures can be found.
3. Although theories for single-phonon and multiple-phonon nonradiative relaxation mechanisms have been established by physics-related and chemistry-related studies respectively, there is no united theory or approach to combine both mechanisms in 0D materials such as nanoclusters and molecules.
4. Both electron-phonon and exciton-phonon interactions are all interpreted in the framework of one-particle picture, which is problematic for nonradiative relaxation of high-energy excitons.

1.3 Outline of the thesis

We shall first establish the computational methodology and approach, which are described in chapters 2, 3, and 4. We then apply our approach to study some selected nanoclusters and molecules to demonstrate the proof of concept of reducing electron phonon interaction in chapters 5 and 6.

In chapter 2, the *GW* method based on the many-body Green's function theory is

introduced. The influence of the self-consistency of the one-particle Green's G on the calculations of electronic inelastic scattering rates in nanoclusters is discussed. The necessity of the self-consistency of G for the simulations of finite systems is also discussed and further demonstrated via the calculations of the electronic inelastic scattering rates in magnesium clusters.

In chapter 3, we establish a computation approach for solving the dynamic Bethe-Salpeter equation (DBSE), one of the basic equations for the dynamics of excitons. A simplification strategy is put forward for the estimation of the excitonic inelastic scattering rates in 0D finite systems. The excitonic inelastic decay rates in a semiconductor nanocluster Si_{20} are investigated. Results obtained by our established simplification strategy are shown to be very close to those obtained by the DBSE method. With much less computational cost than DBSE, our method provides a fast way for accurate calculations of the excitonic inelastic scattering rates. The approach can be widely used for calculations of dynamics, i.e. excitonic inelastic scattering rates in larger systems. Without our approach or simplification, calculations for inelastic scattering rates in such systems are essentially infeasible.

In chapter 4, we establish a unified formulation for electron-phonon and exciton-phonon interaction in nanoclusters by including both single-phonon decay mechanism and multiple-phonon decay mechanisms. We show that the single-phonon and multiple-phonon relaxation mechanisms should be studied separately, as they correspond to two types of physical processes and have totally different spectral lineshapes. The single-phonon relaxation mechanism shall correspond to a Lorentzian function, which comes as the imaginary part of an electron-phonon self-energy term. The multiple-phonon relaxation mechanism, on the other hand, shall be related to a Gaussian function, since it is essentially a thermal process and involves an anharmonic effect (displacement of the potential energy surface in finite systems). It is also demonstrated that the formulas derived for the two relaxation mechanisms share a general form at the delta-function limit.

In chapter 5, we propose a possible mechanism for reducing the electron-phonon coupling in semiconductor nanoclusters by calculating some chalcogenides. The strategy is based on the mechanism that the valence electrons in heavier atoms are pushed farther away from nuclei by the core electrons and thus are less sensitive to the movement of nuclei. This may suppress the energy exchange rate between electrons and phonons, and lead to "quantum thermal insulation". This strategy is called "valence-electron-separation". As an example, electronic and excitonic nonradiative relaxation rates in lead chalcogenide nanoclusters (PbX)36 (X=S, Se and Te) are calculated by the numerical methods developed in Chap. 4. The simulation results show that electronic and excitonic nonradiative relaxation rates are lower in clusters with heavier atoms, and thus demonstrate the feasibility of the valence-electron-separation strategy.

In chapter 6, excitonic nonradiative relaxation rates in a porphyrin molecule and a porphyrin derivative are calculated by the numerical methods developed in Chap. 4. The simulation results show that the excitonic nonradiative relaxation rates in a porphyrin derivative with heavier atoms are lower than those in a porphyrin molecule. The results further demonstrate the strategy proposed in Chap. 5 that exciton-phonon interaction can be reduced by pushing valence electrons away from their nuclei with more core electrons in heavier atoms.

In chapter 7, a summary of the findings in this thesis is presented.

1.4 Contribution of the thesis

The thesis addresses the dynamics of excitons in nano-clusters from two different aspects: the methodology and its applications.

Methodology

1. The numerical implementations for the calculation of the electronic inelastic scattering rates in nanoclusters are developed based on the many-body Green's function theory.

2. An efficient computational approach – a simplification strategy for the calculation of excitonic inelastic scattering rates in nanoclusters is developed. This strategy allows moderate computational resource for those tasks that were essentially infeasible before.

3. The computational approach and strategy developed include both the single-phonon and the multiple-phonon relaxation mechanisms for the study of nonradiative relaxation rates of electronic and excitonic states in nanoclusters.

4. We uncover the fundamentally distinctive processes for the nonradiative relaxation of one-particle states and two-particle states, which is attributed to significant differences between the DOSs of one-particle states and two-particle states.

Application

1. A method or strategy is proposed to reduce the electron-phonon coupling in nanoclusters to enhance the efficiency of nanocluster-based photovoltaics by pushing valence electron away from nuclei with core electrons in heavy atoms.

2. The proposed method or strategy is demonstrated with the numerical simulations of lead chalcogenide nano clusters.

3. The proposed method or strategy is demonstrated with the numerical simulations of porphyrin molecule and a porphyrin derivative.

Chapter 2

Inelastic scattering relaxation rates of electrons in nanoclusters studied by many-body Green's function theory

2.1 Introduction

2.1.1 Inelastic scattering of one-particle states

One-particle excitations of a multi-electron system can be obtained by adding an electron to the system, or removing an electron from it. A one-particle state can further decay through two typical pathways, namely inelastic scattering and nonradiative relaxation. Here inelastic scattering means that a high-energy one-particle state jumps into a low-energy one-particle state, with its extra energy promoting another electron from the valence band to the conduction band. The nonradiative relaxation, on the other hand, means that a high-energy one-particle state jumps into a low-energy one-particle state, with its extra energy promoting collective oscillation modes of nuclei, namely phonons. During the nonradiative relaxation process, some useful energy is dissipated due to the thermalization. In this chapter, we solely work on the inelastic scattering process of one-particle states. The energy exchange rate between the electrons and phonons will be discussed in Chap. 4.

Inelastic scattering relaxation of electrons in condensed matter systems is a phenomenon that is technically and fundamentally important in many physical and chemical processes.[12] Inelastic scattering rates of hot electrons (holes) in bulk metals and metallic surfaces have been widely investigated both experimentally and theoretically for several decades.[13-15] As zero-dimensional materials, nanoclusters demonstrate electronic structures distinct from their bulk counterparts.[16] A natural

question arises about whether the dynamics of the electrons in a confined system is also different from the bulk. Yet the understanding about the electronic inelastic scattering processes in nanoclusters is quite limited.

It is known that, confined systems exhibit discrete electronic levels, which results in fewer states available for the transition of electrons. Thus hot electrons may have lower inelastic scattering relaxation rates as compared to electrons in the bulk. On the other hand, the screening effect is weakened in small metallic clusters due to the smaller number of electrons, which shall increase the inelastic scattering rates of electrons. Therefore the inelastic scattering rates of a hot electron in a cluster can be either smaller or larger than that in corresponding bulk materials due to the two competing effects.[14]

Experimentally, time-resolved two-photon photoemission (TR-2PPES) has been applied to measure the relaxation dynamics of electrons in nanoparticles and nanoclusters.[17] TR-2PPES is a two-photon technique, which excites the sample into its intermediate state with the first laser pulse and extracts a photoelectron from the sample with the second laser pulse. The decay dynamics of the intermediate states of materials can thus be characterized by varying the temporal delay between the two laser pulses. However, even with such an advanced technique, the fundamentals for the process remain unclear. Firstly, the intermediate state is still a neutral excited state, containing an electron and a hole. This is essentially an excitonic state. Whether the decay of this state is solely due to the electron or the hole cannot be distinguished. Also, it is difficult to distinguish the decay of inelastic scattering and that of nonradiative relaxation. Therefore numerical simulations based on fundamental theories is essential for the understanding of the experimental results.

2.1.2 Methods for one-particle states

There are various theoretical approaches for the simulation of electronic properties of a multi-electron system. Over the past several decades, the density functional

theory (DFT) has been widely used for calculating ground-state properties of molecules and solids.[18] Within the framework of DFT, the original many-body system is replaced by a non-interacting reference system composed of independent particles. Thus the complicated exchange-correlation term in the electronic Hamiltonian becomes a simple local potential. This simplification reduces the computational cost significantly, and thus enables the use of DFT, a prevailing simulation method. However, there are two reasons to develop a more advanced method for the problem encountered in this thesis. Firstly, a well known issue of DFT is its tendency to underestimate the electronic band gaps. Actually the electronic eigenvalues obtained by DFT usually differ notably from the excitation energies of one-particle states obtained by photoemission experiments. Secondly, the original exchange-correlation term in the electronic Hamiltonian is frequency-dependent, while the local potential of DFT is not. Thus DFT is basically incapable of handling any dynamic properties of one-particle states, such as electronic inelastic scattering rates, which are exactly what we need.

The *GW* method was derived from many-body Green's function theory to overcome the limitations and drawbacks of DFT. The name of *GW* comes from the fact that the exchange-correlation term, which is over-simplified in DFT, is now expressed as the product of a one-particle Green's function G and a dynamically screened Coulomb interaction W. The concept was first applied to electron gas by Quinn and Ferrell.[19] In 1965, Hedin developed a systematic and rigorous method for the expansion of the exchange-correlation term, and established a set of integral equations.[20] By taking the first term of the expansion, the *GW* approximation (*GW*A) was formally introduced. The *GW* method is physically sound because it is qualitatively valid in some limiting cases, including isolated atoms and an electron gas. The *GW* method has been proven to be accurate for the simulations of electronic energies of a vast range of materials.[21-24] The superiority of the *GW* method over DFT arises from the fact that the non-local and dynamic features of the self-energy are preserved for each one-particle state in the *GW* implementation, but not in the

DFT scheme.

The dynamics of electrons, i.e. the inelastic scattering rates or inelastic scattering lifetimes (inverses of the rates) in bulk materials, especially bulk metals, have been investigated by the *GW* method.[14,15] Electronic inelastic scattering rates in two-dimension (2D) and one-dimension (1D) structures, such as graphene[25,26] and carbon nanotubes[27] have also been calculated with the GW method. Recently, effort has been made to apply the *GW* method to the electronic inelastic scattering rates in a finite jellium sphere in nanoscale.[28] In such a zero-dimensional (0D) structure, it was found that the electronic inelastic scattering lifetimes in a finite jellium nano-sphere are in the femtosecond time scale. As far as we know, applications of the *GW* method to study electronic inelastic scattering rates in 0D nanoclusters have not been reported. Furthermore, strategy and methodology for the simulations of electronic inelastic scattering rates in nanoclusters cannot be found in literatures until now. As has been introduced in Chap. 1, understanding of the electronic inelastic scattering rates in nanoclusters (or quantum dots) is required to build efficient solar cells. Thus the development of appropriate theoretical and numerical methods becomes necessary.

In this chapter, *GW*-based strategy for electronic inelastic scattering rates in finite 0D nanoclusters are discussed and established. Because almost all literature studying the electronic inelastic scattering rates are only about metallic systems, metallic nanoclusters are used as examples in this chapter in order to compare and verify the calculations. We will start from many-body Green's function theory. After the discussion of the self-consistency of G (one-particle Green's function), the inelastic scattering lifetimes of electrons and holes in two Mg clusters are calculated, and the physical characteristics of the electronic inelastic scattering decay in nanoclusters are presented.

2.2 Many-body Green's function theory

2.2.1 One-particle Green's function

The concept of the Green's function (also known as the propagator) is the most fundamental quantity in many-body theory. The one-particle Green's function is defined as[29]

$$G(\mathbf{r},t;\mathbf{r}',t') = -i\langle N,0|T\left[\hat{\psi}_H(\mathbf{r},t)\hat{\psi}_H^{\dagger}(\mathbf{r}',t')\right]|N,0\rangle \tag{2.1}$$

where $|N,0\rangle$ is the ground state of a N-particle system. $\hat{\psi}_H(\mathbf{r},t)$ and $\hat{\psi}_H^{\dagger}(\mathbf{r}',t')$ are the field operators in the Heisenberg picture. Thus

$$\hat{\psi}_H(\mathbf{r},t) = e^{i\hat{H}t/\hbar}\hat{\psi}_S(\mathbf{r})e^{-i\hat{H}t/\hbar} \tag{2.2a}$$

$$\hat{\psi}_H^{\dagger}(\mathbf{r}',t') = e^{i\hat{H}t'/\hbar}\hat{\psi}_S^{\dagger}(\mathbf{r}')e^{-i\hat{H}t'/\hbar} \tag{2.2b}$$

where $\hat{\psi}_S(\mathbf{r})$ and $\hat{\psi}_S^{\dagger}(\mathbf{r}')$ are the corresponding field operators in the Schrodinger picture, and $\hat{H}$ is the Hamiltonian of the system. $\hat{\psi}_H(\mathbf{r},t)$ annihilates a particle (or creates a hole) at r at time t, and is called annihilation operator. $\hat{\psi}_H^{\dagger}(\mathbf{r}',t')$ creates a particle at r' and t', and is called creation operator. T is the time-ordering operator,

$$T\left[\hat{\psi}_H(\mathbf{r},t)\hat{\psi}_H^{\dagger}(\mathbf{r}',t')\right] = \begin{cases} \hat{\psi}_H(\mathbf{r},t)\hat{\psi}_H^{\dagger}(\mathbf{r}',t') & t > t' \\ \hat{\psi}_H^{\dagger}(\mathbf{r}',t')\hat{\psi}_H(\mathbf{r},t) & t < t' \end{cases} \tag{2.3}$$

Assume that we have a complete set of eigenstates $\{|M,i\rangle\}$ (ith excited state of a system with M electrons). Then we can insert them between $\hat{\psi}_H(\mathbf{r},t)$ and $\hat{\psi}_H^{\dagger}(\mathbf{r}',t')$ in Eq. (2.1),

$$G(\mathbf{r},t;\mathbf{r}',t') \equiv -i\sum_{M,i}\begin{bmatrix}\theta(t-t')\langle N,0|\hat{\psi}_H(\mathbf{r},t)|M,i\rangle\langle M,i|\hat{\psi}_H^{\dagger}(\mathbf{r}',t')|N,0\rangle \\ +\theta(t'-t)\langle N,0|\hat{\psi}_H^{\dagger}(\mathbf{r}',t')|M,i\rangle\langle M,i|\hat{\psi}_H(\mathbf{r},t)|N,0\rangle\end{bmatrix} \tag{2.4}$$

where $\theta(t-t')$ is the step function and it has an integral representation

$$\theta(t-t') = -\lim_{\eta\to 0^+}\int_{-\infty}^{\infty}\frac{d\omega}{2\pi i}\frac{e^{-i\omega(t-t')}}{(\omega+i\eta)} \tag{2.5}$$

The matrix elements $\langle N,0|\hat{\psi}_H(\mathbf{r},t)|M,i\rangle$ and $\langle M,i|\hat{\psi}_H^{\dagger}(\mathbf{r}',t')|N,0\rangle$ are not vanishing only when $M=N+1$. $\langle N,0|\hat{\psi}_H^{\dagger}(\mathbf{r}',t')|M,i\rangle$ and $\langle M,i|\hat{\psi}_H(\mathbf{r},t)|N,0\rangle$ are not vanishing only when $M=N-1$.

Substitute Eqs. (2.2) and (2.5) into Eq. (2.4) and perform a Fourier transformation. We can then obtain

$$G(\mathbf{r},\mathbf{r}';E) = \sum_n \frac{\varphi_n(\mathbf{r})\varphi_n(\mathbf{r}')}{E-E_n+i\eta_n 0^+} \tag{2.6}$$

where E_i and φ_i are, respectively, the energy and wavefunction of the ith quasiparticle (QP). The coefficient η_n is +1 for unoccupied states and −1 for occupied states.

The equation of motion for an operator $\hat{O}$ in the Heisenberg picture is

$$i\frac{\partial\hat{O}}{\partial t} = \hat{O}\hat{H}-\hat{H}\hat{O} = \left[\hat{O},\hat{H}\right] \tag{2.7}$$

Substituting Eq. (2.1) into the equation of motion and performing a Fourier transformation, we have

$$\left(\hat{T}+V_{ext}+V_H-E\right)G(\mathbf{r},\mathbf{r}';E)+\int d\mathbf{r}''\Sigma_{xc}(\mathbf{r},\mathbf{r}'';E)G(\mathbf{r}'',\mathbf{r}';E) = \delta(\mathbf{r},\mathbf{r}') \tag{2.8}$$

where $\hat{T}$ is the electron kinetic energy, V_{ext} is the external potential and V_H is the Hartree potential. $\Sigma_{xc}(\mathbf{r},\mathbf{r}'';E)$ is the exchange-correlation self-energy with all nonlocal and dynamic properties preserved. Then one-particle energy E_i and wavefunction φ_i can be obtained by solving the quasiparticle (QP) equation

$$\left(\hat{T}+V_{ext}+V_H\right)\varphi_i(\mathbf{r})+\int d\mathbf{r}'\Sigma_{xc}(\mathbf{r},\mathbf{r}';E_i)\varphi_i(\mathbf{r}')=E_i\varphi_i(\mathbf{r}) \tag{2.9}$$

2.2.2 Hedin's equations

Eq. (2.8) defines the exchange-correlation self-energy Σ_{xc}. However it can not be used to solve Eq. (2.9) where an explicit form of Σ_{xc} is required for the numerical implementation. To solve Eq. (2.9), the inverse dielectric function is introduced

$$\varepsilon^{-1}(1,2)=\frac{\delta V_{eff}(1)}{\delta V_{ext}(2)} \tag{2.10}$$

where 1 means $(\mathbf{r}_1,t_1)$, $\delta V_{eff}(1)$ is the change of the effective potential at $(\mathbf{r}_1,t_1)$ due to the perturbation of the external potential $\delta V_{ext}(2)$ at $(\mathbf{r}_2,t_2)$. We can also define the reducible polarizability $\Pi(1,2)$ as

$$\Pi(1,2)=\frac{\delta n(1)}{\delta V_{ext}(2)} \tag{2.11}$$

where $\delta n(1)$ is the change of the charge density at $(\mathbf{r}_1,t_1)$ due to the perturbation of the external potential $\delta V_{ext}(2)$ at $(\mathbf{r}_2,t_2)$. With rearrangement we can get a set of coupled integral equations named after Hedin,[20]

$$\Sigma_{xc}(1,2)=i\int d(34)G(1,3)W\left(4,1^+\right)\Gamma(3,2;4) \tag{2.12a}$$

$$P(1,2) = -i\int d(34)G(1,3)G(4,1^+)\Gamma(3,4;2) \tag{2.12b}$$

$$W(1,2) = V(1,2) + \int d(34)V(1,3)P(3,4)W(4,2) \tag{2.12c}$$

$$\Gamma(1,2;3) = \delta(1,2)\delta(1,3) + \int d(4567)\frac{\delta\Sigma_{xc}(1,2)}{\delta G(4,5)}G(4,6)G(7,5)\Gamma(6,7;3) \tag{2.12d}$$

where $P(1,2)$ is the irreducible polarizability, $W(1,2)$ is the screened Coulomb interaction, $V(1,2)$ is the Coulomb interaction, $\delta(1,2)$ is the delta function, and $\Gamma(1,2;3)$ is the vertex function containing 3 variables, with the third one distinguished from the first two by a semicolon. 1^+ means $\mathbf{r}_1$ and t_1+0^+, the infinitesimal time 0^+ is introduced to maintain the correct order when dealing with the time-ordering operator.

2.2.3 Approximation of Γ

Hedin equations are still too complicated to be solved. Thus an approximation has to be made to simplify the equation set (2.12). Usually we can start with the approximation for Eq. (2.12d), and the simplest one is

$$\Gamma(1,2;3) \approx \delta(1,2)\delta(1,3). \tag{2.13}$$

where $\delta(1,2)$ is the delta function and it is not vanishing only when $\mathbf{r}_1 = \mathbf{r}_2$ and $t_1 = t_2$.

Then we have

$$P(1,2) \approx -iG(1,2)G(2,1^+) = P_0(1,2) \tag{2.14}$$

where $P_0(1,2)$ is the independent-particle polarizability (no particle-particle interaction), and its Fourier transformation can be written as[30]

$$P_0(\mathbf{r},\mathbf{r}';E)=2\sum_{v,c}\varphi_v(\mathbf{r})\varphi_c^*(\mathbf{r})\varphi_v^*(\mathbf{r}')\varphi_c(\mathbf{r}')\left[\frac{1}{E-(\varepsilon_c-\varepsilon_v-i0^+)}-\frac{1}{E+(\varepsilon_c-\varepsilon_v-i0^+)}\right] \tag{2.15}$$

where E is the energy, $\varphi(\mathbf{r})$ and ε are wavefunctions and energies of one-particle states obtained by density functional theory (DFT). The subscript 'c' and 'v' stand for unoccupied states (conduction band) and occupied states (valence band).

Under this approximation, the screened Coulomb interaction and the exchange-correlation self-energy becomes

$$W(1,2)\approx V(1,2)+\int d(34)V(1,3)\Pi(3,4)V(4,2) \tag{2.16}$$

$$\Sigma_{xc}(1,2)\approx iG(1,2)W(2,1^+) \tag{2.17}$$

This is the so-called *GW* approximation (*GW*A). Note that the reducible polarizability $\Pi(1,2)$ in Eq. (2.11) is solved from the random phase approximation (RPA):

$$\Pi(1,2)=P_0(1,2)+\int d(34)P_0(1,3)V(3,4)\Pi(4,2). \tag{2.18}$$

Thus the approximation Eq. (2.13) is noted as RPA/*GW*A. The Fourier transformation of Π can be expressed as the summation of electron-hole excitation modes[31]

$$\Pi(\mathbf{r},\mathbf{r}';E)=2\sum_{s}\rho_s(\mathbf{r})\rho_s^*(\mathbf{r}')\left[\frac{1}{E-(\omega_s-i0^+)}-\frac{1}{E+(\omega_s-i0^+)}\right] \tag{2.19}$$

where

$$\rho_s(\mathbf{r})=\sum_{v,c}R_s^{v,c}\varphi_v^*(\mathbf{r})\varphi_c(\mathbf{r}) \tag{2.20}$$

is the particle-hole amplitude for the *s*th particle-hole excitations. The eigenvectors

$\mathbf{R}_s^{v,c}$ and eigenvalues ω_s in Eqs. (2.19) and (2.20) are determined through Eq. (2.18). Note that Π reflects the behavior of the electron-hole excitations of a system, and essentially involves two-particle properties. It will be discussed more in the next chapter.

Another approximation for Eq. (2.12d) is based on the density functional theory (DFT), where the exchange-correlation self-energy $\Sigma_{xc}(1,2)$ is simplified to a local exchange-correlation potential,

$$\Sigma_{xc}(1,2) \approx V_{xc}(1)\delta(1,2). \tag{2.21}$$

where $V_{xc}(1)$ is the exchange-correlation potential from DFT. $\delta(1,2)$ means $\delta(\mathbf{r}_1,\mathbf{r}_2)\delta(t_1,t_2)$ Note that $\Sigma_{xc}(1,2)=\Sigma_{xc}(\mathbf{r}_1,t_1;\mathbf{r}_2,t_2)$ is non-local and time-dependent, while $V_{xc}(1)$ is local and essentially time-independent.

Substitute Eq. (2.21) into Eq. (2.12d), we can get

$$\Gamma(1,2;3) \approx \delta(1,2)\delta(1,3) - i\int d(45)\delta(1,2)f_{xc}(1)G(1,4)G(5,1^+)\Gamma(4,5;3) \tag{2.22}$$

where

$$f_{xc}(1) = \frac{\delta V_{xc}(1)}{\delta n(1)} \tag{2.23}$$

Note that V_{xc} is the exchange-correlation function in DFT, and f_{xc} is the derivative of V_{xc} of the electronic spatial density n.

Here Eqs. (2.16) and (2.17) still hold, while now the reducible polarizability Π in Eq. (2.14) should be solved from the time-dependent adiabatic local density approximation (TDLDA)

$$\Pi(1,2) = P_0(1,2) + \int d(34) P_0(1,3)\left[V(3,4) + f_{xc}(3)\delta(3,4)\right]\Pi(4,2). \qquad (2.24)$$

Thus the approximation Eq. (2.22) is noted as TDLDA/*GW*Γ, where Γ means that the vertex function is more than just a delta function. The Fourier transformation of Π in this case still can be expressed as Eq. (2.19), but the numerical values may be different.

It should be emphasized that RPA/*GW*A in Eq. (2.13) and TDLDA/*GW*Γ in Eq. (2.24) are two different levels of approximation. It has been demonstrated that the mixtures of the two methods, namely RPA/*GW*Γ or TDLDA/*GW*A, are not suggested.[32]

2.2.4 *GW* implementations

The electronic energies of a many-body system can be obtained by solving the quasiparticle (QP) equation Eq. (2.9). In practical implementation, this equation is solved based on the results of the density functional theory (DFT)

$$\left(\hat{T} + V_{ext} + V_H\right)\varphi_i(\mathbf{r}) + V_{xc}(\mathbf{r})\varphi_i(\mathbf{r}) = \varepsilon_i\varphi_i(\mathbf{r}) \qquad (2.25)$$

where ε_i and φ_i are the eigenvalue and eigenfunction of the *i*th electronic state obtained by DFT, respectively, and $V_{xc}(\mathbf{r})$ is the exchange-correlation potential. With the assumption that the DFT eigenfunctions agree well with the QP wavefunctions in most cases,[23] the QP energies are usually solved with a perturbative method to the first order

$$\left\langle \varphi_i \middle| \Sigma_{xc}(\mathbf{r},\mathbf{r}';E_i) \middle| \varphi_i \right\rangle - \left\langle \varphi_i \middle| V_{xc}(\mathbf{r}) \middle| \varphi_i \right\rangle = E_i - \varepsilon_i \qquad (2.26)$$

The self-energy term $\left\langle \varphi_i \middle| \Sigma_{xc} \middle| \varphi_i \right\rangle$ in Eq. (2.26) can be separated as an energy-independent exchange part $\left\langle \varphi_i \middle| \Sigma_x \middle| \varphi_i \right\rangle$ and an energy-dependent correlation

part $\langle\varphi_i|\Sigma_c|\varphi_i\rangle$. The latter is evaluated as[33]

$$\langle\varphi_i|\Sigma_c(\mathbf{r},\mathbf{r}';E)|\varphi_i\rangle=\sum_n\sum_s\frac{a_{n,s,i}}{E-E_n-\omega_s\eta_n} \tag{2.27}$$

where $a_{n,s,i}$ equals $2\langle\varphi_i\varphi_n|V|\rho_s\rangle\langle\rho_s|V|\varphi_i\varphi_n\rangle$ for the *GW*A implementation, and $2\langle\varphi_i\varphi_n|(V+f_{xc})|\rho_s\rangle\langle\rho_s|V|\varphi_i\varphi_n\rangle$ for the *GW*Γ implementation.

The imaginary parts of the QP energies can be obtained by applying analytical continuation of $\Sigma_c(\mathbf{r},\mathbf{r}';E)$ in the complex energy plane, and the complex QP energy $E_i-i\eta_i\gamma_i$ is calculated by solving a complex equation set numerically

$$\mathrm{Re}\langle\varphi_i|\Sigma_{xc}(E_i-i\eta_i\gamma_i)|\varphi_i\rangle-\langle\varphi_i|V_{xc}|\varphi_i\rangle=E_i-\varepsilon_i \tag{2.28a}$$

$$\left|\mathrm{Im}\langle\varphi_i|\Sigma_{xc}(E_i-i\eta_i\gamma_i)|\varphi_i\rangle\right|=\gamma_i \tag{2.28b}$$

where γ_i is exactly the relaxation rate of the *i*th electron (hole) due to the inelastic electron-electron scattering. The corresponding lifetime is evaluated as[30]

$$\tau_i=(2\gamma_i)^{-1} \tag{2.29}$$

2.3 Numerical details

In this chapter we will use two Mg clusters, Mg_{10} and Mg_{40}, as examples to demonstrate the method developed for the simulation of electronic inelastic scattering rates in finite 0D clusters. There are several reasons to choose Mg clusters. Firstly, bulk magnesium is close to free electron gas (FEG), and any results about electronic inelastic scattering rates in FEG in literature can be used as reference. Secondly, the electronic inelastic scattering rates in bulk Mg have been calculated by the *GW* method. Thus we can compare the difference between the electronic inelastic

scattering rates in 0D and 3D systems. Thirdly, experimental data of ionization potentials and electronic affinities of various Mg clusters have been invested experimentally and theoretically, which can be used to check the accuracy of the *GW* code developed by ourselves.

The ground state DFT calculations within the local density approximation (LDA) are performed using the SIESTA code.[35] The core electrons [$1s^2 2s^2 2p^6$] of Mg are replaced by the nonlocal norm-conserving pseudopotential based on the Troullier-Martins scheme.[36] A double-ζ polarization (DZP) basis set of numerical atomic orbitals is used for the valance electrons of Mg. The cutoff radii are 10.0 a.u. for both *s*- and *p*-orbitals. The structures are optimized by simulated annealing using molecular dynamics with an exponential cooling schedule, followed by the conjugated gradient algorithm with the maximum force tolerance of 0.01 eV/Å. The optimized structures of Mg_{10} and Mg_{40} are illustrated in Fig. 2-1.

All integrals are evaluated on a uniform grid in real space with a grid spacing of 0.6 a.u., which has been tested to give QP energies with an accuracy of 0.1 eV. The exchange integrals $\int d\mathbf{r}\int d\mathbf{r}'\varphi_i(\mathbf{r})\varphi_j(\mathbf{r})V(\mathbf{r},\mathbf{r}')\varphi_k(\mathbf{r}')\varphi_l(\mathbf{r}')$ are evaluated by solving Poisson equations first with the multigrid method.[37] The convergence of the QP calculation usually requires a large number of unoccupied states for the evaluation of the polarizability. Thus a COHSEX remainder scheme[33] has been applied to accelerate the convergence of the correlation part $\langle\varphi_i|\Sigma_c|\varphi_i\rangle$.

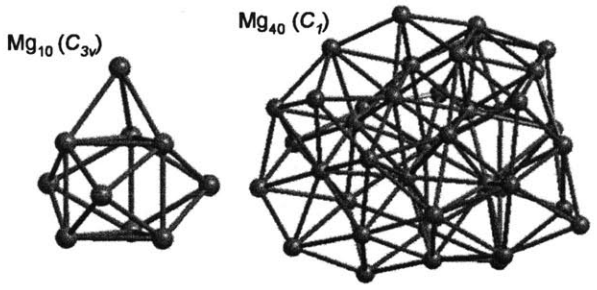

Figure 2-1. Optimized structures of Mg_{10} and Mg_{40}. The labels in parentheses correspond to the point group symmetries of the clusters.

2.4 Results and discussion

2.4.1 Effects of self-consistency on quasiparticle energies and lifetimes

In the quasiparticle (QP) calculations, a ready starting point is the approximation for G

$$G(\mathbf{r},\mathbf{r}';E) \approx G_0(\mathbf{r},\mathbf{r}';E) = \sum_n \frac{\varphi_n(\mathbf{r})\varphi_n(\mathbf{r}')}{E-\varepsilon_n+i\eta_n 0^+} \tag{2.30}$$

where ε_n are DFT energies of one-particle states. From G_0 we can calculate W and thus Σ_{xc} and GW energies E_n of one-particle. However introduction of Eq. (2.30) brings an uncertainty: whether we should recalculate every quantity with the updated G until its convergence, namely self-consistency. It has been shown that the self-consistency cycles including W ($G \rightarrow W \rightarrow \Sigma_{xc} \rightarrow G$) may deteriorate the agreements between the simulated results and experimental data.[38] So in this study, we take W as constant and focus on the effect of self-consistency of G ($G \rightarrow \Sigma_{xc} \rightarrow G$) on the QP properties. For comparison, we solve Eq. (2.28) only once in the non-self-consistent calculation. In the self-consistent calculation, however, G is updated after each cycle until its convergence. We speculate the influence of the self-consistency on the calculations of the QP lifetimes as follows.

According to Eqs. (2.27) and (2.28), the decay rate of the ith QP can be written as a summation

$$S_i = 2\left|\sum_n \sum_s \frac{a_{n,s,i}\gamma_i}{(E_i - E_n - \omega_s\eta_n)^2 + \gamma_i^2}\right| \tag{2.31}$$

The quantity $E_i - E_n - \omega_s\eta_n$ in each denominator indicates the coupling of the ith QP with the nth state through the sth excitonic excitation of the system. A large

contribution is expected when $E_i - E_n$ and $\omega_s \eta_n$ are very close to each other. If G_0 is used, then $E_i - \varepsilon_n - \omega_s \eta_n$ will replace $E_i - E_n - \omega_s \eta_n$, which diminishes the underlying physics of the summation, since the Kohn-Sham system used in DFT is only an artificial non-interacting reference system, and the ε_n, energies of DFT electronic states, do not have any clear physical meaning.

Secondly, the self-consistency is better off in terms of the poles of the summation S_i. For a given QP with energy E_i, simplifying E_n to ε_n changes the positions of the poles from $E_n + \omega_s \eta_n$ to $\varepsilon_n + \omega_s \eta_n$. This only has a minor effect on $\mathrm{Re}\langle \varphi_i | \Sigma_c | \varphi_i \rangle$, which is determined by the ensemble of the poles including those lying far away from E_i. However, the simplification may cause considerable error to $\left| \mathrm{Im}\langle \varphi_i | \Sigma_c | \varphi_i \rangle \right|$, which is mostly determined by the arrangement of the poles in the vicinity of E_i. The effect is illustrated schematically in Fig. 2-2, where the unoccupied (occupied) energy levels ε_n obtained by DFT are shifted up (down) to yield the QP energy levels E_n. Yet the poles $\varepsilon_n + \omega_s \eta_n$ are not moved together, leading to misplaced poles around a given energy level E_i, especially for the highest occupied molecular orbital (HOMO) and the lowest unoccupied molecular orbital (LUMO). In Fig. 2-2, the LUMO and HOMO QP energy levels are adjacent to some of the poles $\varepsilon_n + \omega_s \eta_n$. This situation will not happen if the poles $E_n + \omega_s \eta_n$ are instead used, since $E_n + \omega_s \eta_n$ will move together with the E_n's and maintain their relative positions correctly.

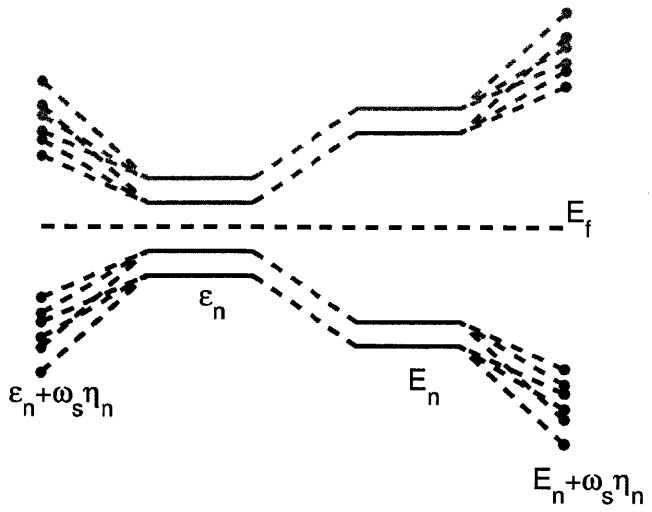

Figure 2-2. Schematic plot for the relation among the DFT energies ε_n's and hence the derived poles $\varepsilon_n + \omega_s \eta_n$, the QP energies E_n's and hence the derived poles $E_n + \omega_s \eta_n$. Each color defines a set including an energy level and the poles accompanying the energy level. To maintain the correct orders, E_n's should be used together with $E_n + \omega_s \eta_n$. A mixture between E_n's and $\varepsilon_n + \omega_s \eta_n$ changes the pole arrangement in the vicinity of a QP energy level, which may introduce notable errors for the QP lifetime.

2.4.2 QP energies and lifetimes in Mg clusters

The QP energies and lifetimes of the HOMOs and LUMOs of the Mg_{10} and Mg_{40} simulated by both the *GW*A and the *GW*Γ methods are listed in Table 2.1. The results obtained without the self-consistency are denoted with G_0. Eigenvalues from DFT with local density approximation (LDA) are also listed. When the decay rate of a QP is vanishingly small, its lifetime is denoted by ∞, indicating a rather long lifetime if only electron-electron inelastic scattering is considered. The relative effect of the self-consistency over the non-self-consistency on the QP energies can be readily read out from Table 2.1. In general, the energy differences between the results obtained with and without the self-consistency are insignificant especially for the larger cluster

Mg_{40}, which is consistent with our analysis about $\mathrm{Re}\langle\varphi_i|\Sigma_c|\varphi_i\rangle$ in the above section.

Table 2.1: QP energies and lifetimes of the HOMOs and LUMOs of Mg_{10} and Mg_{40} clusters calculated by the *GW*A and the *GW*Γ methods with both self-consistency (denoted with G) and non-self-consistency (denoted with G_0). The subscript in the first column stands for the number of Mg atoms in the cluster. DFT/LDA energies are also listed in the last column.

	G_0WA		*GW*A		$G_0W\Gamma$		*GW*Γ		LDA
	E(eV)	τ (fs)	E(eV)	τ (fs)	E(eV)	τ (fs)	E(eV)	τ (fs)	ε(eV)
$HOMO_{10}$	-5.80	∞	-5.95	∞	-5.41	∞	-5.47	∞	-4.26
$LUMO_{10}$	-2.14	∞	-2.06	∞	-1.79	∞	-1.49	∞	-2.93
$HOMO_{40}$	-5.16	6.4	-5.31	∞	-4.73	16	-4.75	∞	-3.98
$LUMO_{40}$	-3.31	27	-3.35	∞	-2.89	12	-2.79	∞	-3.74

On the other hand, the net effect of the self-consistency on the QP lifetimes, is strongly size-dependent. For Mg_{10}, no change has been observed in both the *GW*A and the *GW*Γ calculations. However, the results have been qualitatively changed in the case of Mg_{40}. As discussed in last section, the QP lifetime is very sensitive to the poles in the vicinity of the QP energy. According to Fig. 2-2, the degree of the misplacement of the poles around the HOMO and LUMO can be roughly estimated by comparing the *GW* correction over DFT $|\Delta E_i| = |E_i - \varepsilon_i|$ and the minimum frequency $\omega_{\min}$ of the reducible polarizability. The error of τ_i is insignificant when $|\Delta E_i|$ is smaller or comparable with $\omega_{\min}$, while it becomes significant when $|\Delta E_i|$ is larger than $\omega_{\min}$. This can be verified by comparing $|\Delta E_i|$ in Table 2.1 with $\omega_{\min}$'s, which are 1.50 (TDLDA) and 1.58 (RPA) eV for Mg_{10}, 0.27 (TDLDA) and 0.29 eV (RPA) for Mg_{40}.

Table 2.1 also illustrates the numerical difference between the two QP methods adopted in this chapter. The net effect of the *GW*Γ over the *GW*A is an upward energy shift, almost rigid for both the HOMO and LUMO. Furthermore, the upward energy shift is observed consistently for all occupied and unoccupied states as shown in Fig.

2-3, where the energy levels of Mg_{40} obtained by the LDA, *GW*A and *GW*Γ methods are plotted. This energy shift, a feature of the *GW*Γ method, has also been reported in bulk silicon,[32] as well as in a benzene molecule.[33] It can be explained using Eq. (2.27), where the *GW*Γ method adds a negative quantity $2\langle\varphi_i\varphi_n|f_{xc}|\rho_s\rangle\langle\rho_s|V|\varphi_i\varphi_n\rangle$ as an extra term to each numerator and thus introduces unidirectional shifts to all E_n's. Thomas *et al.* have measured the photoelectron spectra (PES) of Mg_n^- clusters.[39] The first PES peak of Mg_n^- can be used as a reference for the electronic affinity (EA) of Mg_n, neglecting the structural relaxation due to an extra electron. According to Ref 39, the EAs of Mg_{10} and Mg_{35} are about 1.70 and 2.85eV, respectively. To compare with these data, we perform the calculations for Mg_{35}. The EAs of Mg_{10} and Mg_{35} predicted by the *GW*Γ are 1.49 and 2.71 eV, respectively, and those obtained by the *GW*A are 2.06 and 3.27 eV, respectively. We also test the basis completeness by increasing the size of the basis set for the simulation of Mg_{10}, and find that the number of bases is not the source of the uncertainty for the EA of Mg_{10}. (The ionization potential of Mg_{10} obtained by the *GW*Γ with the basis set 4Z4P is 1.45 eV, which is slightly lower than that of the DZP result.) Jellinek et al. have calculated the ionization potential (IP) of neutral magnesium clusters with the gradient-corrected DFT.[40] The IP of Mg_{10} is obtained as 5.5 eV in Ref. 40, and 5.47 eV (*GW*Γ) and 5.95 eV (GWA) in this work. Summarizing above, we find that the *GW*Γ agrees with currently available data better than the *GW*A. Therefore our discussion will focus on the QP lifetimes of Mg_{40} obtained by the self-consistent *GW*Γ approach, since Mg_{10} does not have enough energy levels for drawing any convincing conclusions.

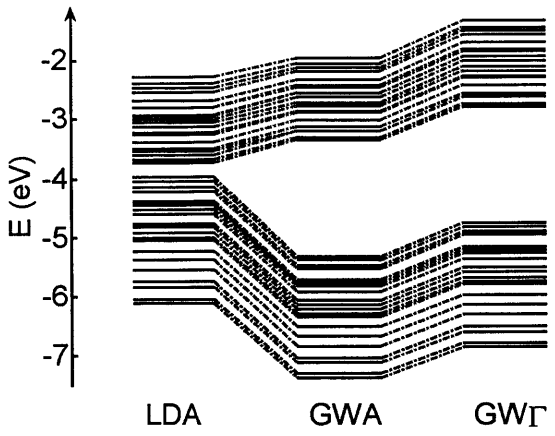

Figure 2-3. Energy levels of Mg_{40} calculated by the LDA, *GW*A and *GW*Γ methods. The net effect of the *GW*Γ over the *GW*A is an almost rigid upward shift in energy.

Inelastic scattering lifetimes τ_i and scaled lifetimes $\tau_i\left(E_i - E_F\right)^2$ of hot electrons and holes in Mg_{40} calculated by the *GW*Γ method are plotted versus the excitation energy $\left|E_i - E_F\right|$ in Figs. 2-4a and 2-4b, respectively. The behavior of electrons in many bulk metals can be described as a free electron gas (FEG). In a high-density FEG, the lifetimes of hot electrons with low excitation energies follow an inverse quadratic law as derived by Quinn and Ferell[19]

$$\tau_i^{\mathrm{QF}} = 263 r_s^{-5/2}\left(E_i - E_F\right)^{-2}\ \mathrm{eV}^2\ \mathrm{fs}. \tag{2.32}$$

where r_s is the electron-density parameter defined as $1/\overline{n} = (4/3)\pi r_s^3$, with $\overline{n}$ being the average electron density. Eq. (2.32) indicates a constant scaled lifetime $\tau_i\left(E_i - E_F\right)^2$ for all hot electrons, which is 22.8 fs eV^2 for bulk magnesium with r_s= 2.66. However, in the cluster Mg_{40}, the scaled QP lifetimes with low excitation energies ($\left|E_i - E_F\right| < 2.1$ eV) are longer than the lifetime obtained from Eq. (2.32) and are energy dependent. On the other hand, the pattern of scaled QP lifetimes with high excitation energies ($\left|E_i - E_F\right| \geq 2.1$ eV) are relatively flat. Thus the results indicate that there are two energy regimes as illustrated in Fig. 2-4: a low energy regime (R_{LE})

and a high energy one (R_{HE}), which will be discussed separately.

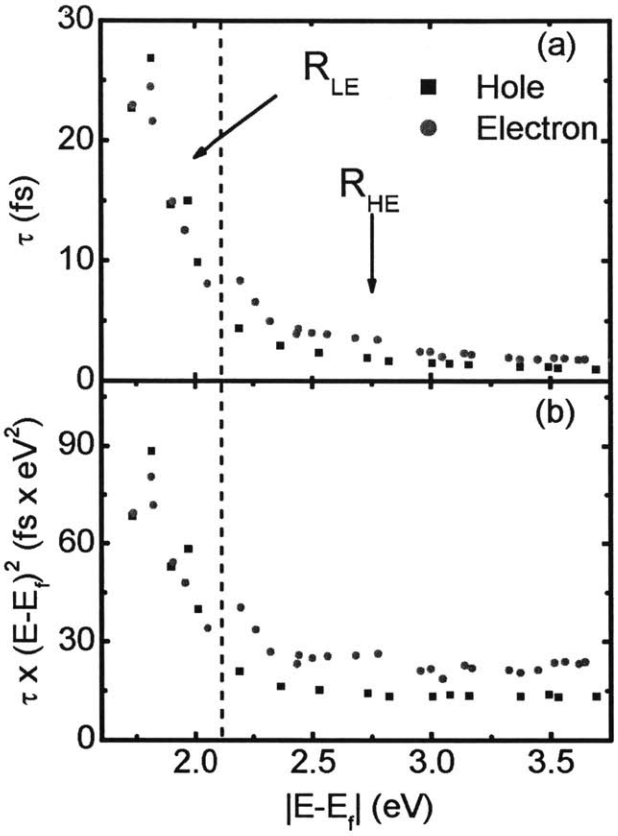

Figure 2-4. a) QP lifetimes and b) scaled QP lifetimes in Mg_{40} obtained by the self-consistent *GWΓ* approach. The vertical dashed line separates both plots into a low energy regime and a high energy regime.

As a general trend, the scaled QP lifetimes in the R_{LE} increase with decreasing $|E_i - E_F|$, and become notably longer than τ^{QF}. This is qualitatively different from the result obtained in the bulk magnesium with the *GW* method.[41] The latter, shows that the inelastic lifetimes of electrons with low excitation energies are close to (or shorter than) τ^{QF}. It has been noted that the QP scattering rate is determined by the two competing factors: the number of states for possible transitions of a hot electron, and the dynamical screening to the interaction between this hot electron and other electrons.[14] As shown in Fig. 2-3, the energy states of a small metallic cluster such as Mg_{40} are missing around the Fermi level due to the

confinement of the electrons, which is quite different from the bulk counterpart. This reduces the number of states available for transitions of all hot electrons (holes) in a cluster. The effect becomes dominant for those energy levels in the R_{LE} with low excitation energies, and thus leads to relatively long QP lifetimes, and the lower the excitation energy, the longer the lifetime. Also in the R_{LE} we find that the lifetimes of hot electrons and hot holes with the same $|E_i - E_F|$ are close to each other, which is similar to the results obtained from the free-electron gas (FEG) in the low excitation regime.[19]

In the regime R_{HE}, the scaled lifetimes of hot electrons fluctuate in the range of 21 to 24 fs eV^2 with increasing $|E_i - E_F|$, which are close to 22.8 fs eV^2 calculated from Eq. (2.32). In bulk Mg, the scaled lifetimes in the same energy regime increase from 25 to 30 fs eV^2 with increasing excitation energy.[41] It is speculated that the slight difference between the cluster and the bulk could be attributed to the electronic spill over effect, as the electron wavefunctions can stretch outside of a finite potential well. This effect is notable for small metallic clusters, and leads to lower electron densities and thus to shorter QP lifetimes.

Note that our results here are different from those in Ref. 28, where shorter lifetimes are found based on spherical jellium model calculations. The difference could be attributed to the definition of the QP excitation energy. In Ref. 28, it is defined as $|\varepsilon_i - \varepsilon_F|$, while for the nanocluster in this article, it is defined as $|E_i - E_F|$, which can be approximated as $|E_i - \varepsilon_i| + |\varepsilon_i - \varepsilon_F|$. The *GW* correction term $|E_i - \varepsilon_i|$ vanishes in an infinite uniform electron gas, yet it could be a large number in finite systems and can also be also strongly size-dependent, as can be seen in Table 2.1.

The scaled lifetimes of hot holes in the R_{HE} decrease slowly with increasing $|E_i - E_F|$. They are shorter than those of hot electrons with the same $|E_i - E_F|$, which also has been found in the case of the FEG.[14] In a finite system such as Mg_{40}, the

shorter hole lifetimes can be attributed to the smaller angular momentums of these holes, which leads to more possible transitions than for electrons. This is an analogy to the bulk, where we can attribute shorter hole lifetimes to the smaller momentums of holes.[42] Note that in simple *s-p* systems, there are no localized *d*-electrons. Correspondingly we have not observed any localized *d*-holes with longer lifetimes than those of electrons, as has been demonstrated in noble metals.[42,43]

2.5 Conclusion

In this chapter, the *GW* method based on the many-body Green's function theory is introduced. The influence of the self-consistency of the one-particle Green's G on the calculations of electronic inelastic scattering rates in nanoclusters is discussed. The necessity of the self-consistency of G for the simulations of finite systems is suggested and further demonstrated via the calculations of the electronic inelastic scattering rates in magnesium clusters.

In a nanocluster Mg_{40}, the inelastic scattering lifetimes of electrons and holes near the Fermi level are found to be longer than those in a free electron gas (FEG) with the same valence electron density, due to the lack of states available for any transitions. In the high excitation energy regime, inelastic scattering lifetimes of hot electrons are consistent with the inverse quadratic relation of Quinn and Ferrell.[19] In this regime, hot holes exhibit shorter scaled lifetimes compared with hot electrons, due to the smaller angular momenta of holes.

The two different approximate levels of the *GW* method, *GW*A and *GW*Γ are tested. It is found that the electronic energies of the *GW*Γ implementation are more close to available experimental data. The superiority of GWΓ over *GW*A for finite systems is consistent with the conclusions in the literature.[32,33] Thus the *GW*Γ method will be used in the following chapters without further justification.

Chapter 3

Inelastic scattering relaxation rates of excitons in nanoclusters studied by many-body Green's function theory

3.1 Introduction

3.1.1 Inelastic scattering of two-particle states

Two-particle excitations of a multi-electron system occur when an electron in the valence band is promoted to the conduction band. Similar to a one-particle state, a two-particle state can further decay through two typical pathways, i.e. inelastic scattering and nonradiative relaxation. Here inelastic scattering means that a high-energy two-particle state jumps into a low-energy two-particle state, while its extra energy promotes another electron from the valence band to the conduction band. The nonradiative relaxation, on the other hand, means that a high-energy two-particle state jumps into a low-energy two-particle state, while its extra energy produces collective oscillation modes of nuclei, namely phonons. During the nonradiative relaxation process, some useful energy is dissipated through thermalization. In this chapter, we focus on the inelastic scattering process of two-particle states. The energy exchange rate between the excitons and phonons will be discussed in Chap. 4.

The inelastic scattering rate of an exciton represents the rate that the exciton transfers its extra energy to another exciton. It can also be regarded as the rate that the exciton splits into two excitons spontaneously. Recalling that excitons in photovoltaic devices correspond to working fluids in heat engines, the splitting of excitons is equivalent to the decomposition of molecules of the working fluid, which is of special interest due to the potential to enhance the efficiencies for electricity generation.

Actually the strategy to improve the performance of photovoltaic devices based on the splitting of excitons in semiconductor nanoclusters has been proposed, which is also is known as the multiple exciton generation (MEG) process.[7] More specifically, during the MEG processes the initial energetic excitonic states created by an incident photon split through the inelastic scattering process and thus increase the photocurrent. Since MEG arises from excitonic inelastic scattering relaxation, the rate of MEG is essentially the excitonic inelastic relaxation rate, or the inverse of the excitonic inelastic scattering lifetime.

Investigations of the MEG processes in some semiconductor nanoclusters have been reported in recent years,[44,45] yet the fundamental of the process is far from clear. For example, there is still a controversy about the relation between the spatial confinement and the MEG performance.[46,47] The uncertainty comes from the following plausibility. Firstly, inside the semiconductor nanoclusters, the presence of a nonradiative relaxation process competes with an inelastic scattering process, and thus complicates the decay dynamics of high-energy excitons. Secondly, surrounding the semiconductor nanoclusters, the chemicals on the cluster surface and the solvent/substrate may significantly influence the excitonic states and the exciton-phonon coupling. Thirdly, it is difficult to perform flawless experiments and to obtain flawless experimental data. Ideally, each of the plausibilities shall be figured out and investigated, so that we can study the specific physics. However, in practice, all these issues are interwoven with each other and manifest themselves in experiments and experimental data, and thus smear out the explanation of these data. Under the circumstance, theoretical simulations based on first-principles calculations become indispensible to provide insight into some of the physics underlying the MEG phenomenon.

In this thesis, we work on the fundamentals of the dynamics of excitons, namely the relaxation of excitons inside the semiconductor nanoclusters, including both inelastic scattering processes and nonradiative relaxation processes. More broadly, the

dynamics of the two decay mechanisms are the intrinsic characteristics of the semiconductor nanoclusters. These mechanisms are of great importance for any electricity generators based on semiconductor nanoclusters.

In this chapter, we develop the methodology for calculating excitonic inelastic scattering rates in nanoclusters. The exciton-phonon interaction will be discussed in the next chapter.

3.1.2 Methods for calculating two-particle states

Before introducing the methods for two-particle states, we show how a two-particle state is expressed. Assuming that there is a four-state system as shown in Fig. 3-1a, which has two occupied states $\varphi_1(\mathbf{r})$ and $\varphi_2(\mathbf{r})$ as the valence band, and two unoccupied states $\varphi_3(\mathbf{r})$ and $\varphi_4(\mathbf{r})$ as the conduction band. This is the ground state of the system and can be expressed as $|ground\rangle$. By neglecting the electronic spin, the system has four one-particle states as shown in Fig. 3-1b, two hole states $\varphi_1(\mathbf{r})$ and $\varphi_2(\mathbf{r})$ and two electron states $\varphi_3(\mathbf{r})$ and $\varphi_4(\mathbf{r})$. For simplicity, we write them as $|1\rangle$, $|2\rangle$, $|3\rangle$ and $|4\rangle$. The four two-particle states of the system are shown in Fig. 3-1c. They have to be expressed as the product of one valence wavefunction and one conduction wavefunction, namely $\varphi_1(\mathbf{r})\varphi_3(\mathbf{r}')$, $\varphi_1(\mathbf{r})\varphi_4(\mathbf{r}')$, $\varphi_2(\mathbf{r})\varphi_3(\mathbf{r}')$ and $\varphi_2(\mathbf{r})\varphi_4(\mathbf{r}')$, or $|1,3\rangle$, $|1,4\rangle$, $|2,3\rangle$ and $|2,4\rangle$ for short.

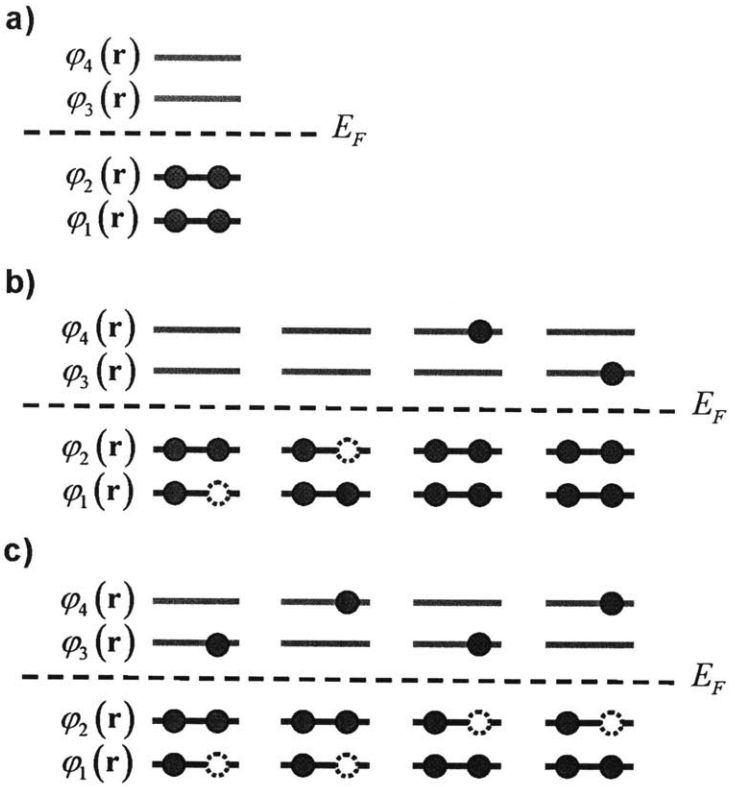

Figure 3-1. a) A four-state system with two occupied states $\varphi_1(\mathbf{r})$ and $\varphi_2(\mathbf{r})$ as the valence band, and two unoccupied states $\varphi_3(\mathbf{r})$ and $\varphi_4(\mathbf{r})$ as the conduction band. b) Two hole states $\varphi_1(\mathbf{r})$ and $\varphi_2(\mathbf{r})$ and two electron states $\varphi_3(\mathbf{r})$ and $\varphi_4(\mathbf{r})$ of the system. c) Four two-particle states $\varphi_1(\mathbf{r})\varphi_3(\mathbf{r}')$, $\varphi_1(\mathbf{r})\varphi_4(\mathbf{r}')$, $\varphi_2(\mathbf{r})\varphi_3(\mathbf{r}')$ and $\varphi_2(\mathbf{r})\varphi_4(\mathbf{r}')$ of the system.

Although $|i\rangle$ are one-particle eigenstates, $|i,j\rangle$ are not necessarily two-particle eigenstates. Only with the independent-particle approximation, where the interaction between any two particles is turned off, are $|i,j\rangle$ the true two-particle eigenstates. It should be pointed out that the independent-particle approximation is a very coarse approximation and its results poorly agree with the experimental data. In all methods with good accuracy, the interaction between $|i,j\rangle$ and $|i',j'\rangle$ has to be taken into

account. This leads to an N-by-N matrix for a system with N two-particle states. The eigenvalues and eigenvectors of the matrix are exactly the energies and wavefunctions of the true two-particle eigenstates of the system. That is to say, a two-particle eigenstate is always the linear combination of all $|i,j\rangle$. For the system shown in Fig 3-1c, we have the kth $|exciton\rangle = c^k_{1,3}|1,3\rangle + c^k_{1,4}|1,4\rangle + c^k_{2,3}|2,3\rangle + c^k_{2,4}|2,4\rangle$ for k=1...4.

As illustrated in Fig. 3-1c, an excitonic state in a multi-electron system essentially involves the particle-hole excitations (or excitons), and can not be correctly formulated by any method based on one-particle picture, including the DFT and GW methods. An economic solution for the problem is the time dependent DFT (TDDFT), a method frequently used together with the adiabatic local density approximation (TDLDA).[48] The TDLDA can produce the right excitonic energies for finite systems. Another powerful yet more cumbersome approach based on the many-body Green's-function theory is the Bethe-Salpeter equation (BSE).[48,49,50] The BSE explicitly includes the exchange and dynamic screened Coulomb interaction between the two particles considered, and is the kind of standard for the simulation of excitons in bulk materials where the TDLDA usually fails. Furthermore, the frequency-dependent kernel of the BSE enables it to capture the dynamic features of excitons, which is also beyond the scope of the TDLDA.

The excitonic energies in different semiconductor nanoclusters have been investigated by BSE,[51,52] yet so far no result has been reported on calculating excitonic inelastic scattering rates in semiconductor nanoclusters by this advanced method. A major reason is that BSE is a frequency-dependent equation, since its kernel explicitly depends on the frequency. We call this original equation as dynamic BSE (DBSE). For calculating excitonic energies, a simplification strategy which converts the frequency-dependent terms into frequency-independent terms has been proposed.[49] We call this simplified equation as the static BSE (SBSE). This strategy has been widely used in almost all BSE calculations, because now the excitonic energies can be obtained just by diagonalizing a frequency-independent matrix.

Unfortunately, the corresponding simplification strategy for calculating excitonic inelastic scattering rates has not been published. This means that we still have to use the DBSE to calculate excitonic inelastic scattering rates. As will be shown later in this chapter, solving the DBSE is extremely expensive in terms of computational cost, since there are a large number of frequency-dependent terms to be evaluated. This seriously hinders the application of the method for the simulation of excitonic inelastic scattering rates in semiconductors nanoclusters, as well as in other materials.

In this chapter, we establish our computation methodology for the excitonic inelastic relaxation rates. We demonstrate our method with a simple semiconductor cluster, Si_{20}. Our approach is aimed at a numerical simplification for use of the dynamic BSE: Instead of solving the time-consuming DBSE, our method only requires the excitonic wavefunctions obtained via TDLDA and the one-particle inelastic scattering rates obtained via $GW\Gamma$. We demonstrate that the approximation method provides results very close to those obtained by the DBSE. Our approach allows the calculation of a relatively large system with the same computational resources, or the computational cost can be reduced dramatically without significant loss of accuracy for the calculation of the excitonic inelastic scattering rates.

Another important issue usually ignored in most BSE calculations in the literature is the self-consistencies of the one-particle Green's function G and the reducible polarizability Π. The one-particle Green's function G contains energies and wavefunctions of all one-particle states. The reducible polarizability Π contains all energies and wavefunctions of all two-particle states. In many-body Green's function theory, G is a required input for the calculation of Π, and Π is a required input for the calculation of G. In this chapter, two numerical implementations for the self-consistencies of G and Π have been tested and a stable numerical program/routine has been proposed.

3.2 Many-body Green's function theory

3.2.1 Two-particle Green's function

In the previous chapter, we have introduced the one-particle Green's function Eq. (2.1) for calculation of the properties of the one-particle electron or hole. We rewrite this equation here as

$$G_1(1,2) = -i\langle N,0|T\left[\hat{\psi}_H(1)\hat{\psi}_H^{\dagger}(2)\right]|N,0\rangle \tag{3.1}$$

where 1 means $(\mathbf{r}_1,t_1)$, and the subscript '1' indicates explicitly that it is the Green's function for the one-particle case. A particle-hole excited state, also known as an exciton, essentially involves two particles and can not be described properly by the one-particle Green's function. Actually all one-particle methods, including DFT and *GW*, are not suitable for simulation of the optical properties of materials. To retain the characteristics of two-particle excitations, a two-particle Green's function has to be introduced as

$$G_2(1,2;1',2') = (-i)^2\langle N,0|T\left[\hat{\psi}_H(1)\hat{\psi}_H(2)\hat{\psi}_H^{\dagger}(2')\hat{\psi}_H^{\dagger}(1')\right]|N,0\rangle \tag{3.2}$$

where N denotes the number of particle. Due to the time-ordering operator T, $G_2(1,2;1',2')$ has 24 possible arrangements based on the relative order of t_1, t_2, $t_{1'}$ and $t_{2'}$, instead of 2 possible arrangements in the case of $G_1(1,2)$. However, not all terms are important, since some of them correspond to the states with two extra particles $|N+2,s\rangle$ or with two extra holes $|N-2,s\rangle$. Numerial comparisons show that there are only 8 important terms corresponding to the particle-hole excitations.[50]

3.2.2 Bethe-Salpeter equation

With G_1 and G_2, we can define the two particle correlation function $L(1,2;1',2')$

as

$$L(1,2;1',2') = -G_2(1,2;1',2') + G_1(1,1')G_1(2,2') \tag{3.3}$$

which satisfies the Bethe-Salpeter equation

$$L(1,2;1',2') = G(1,2')G(2,1') + \int d(33'44')G(1,3)G(3',1')\Xi(3,4';3',4)L(4,2;4',2') \tag{3.4}$$

The integral kernel $\Xi(3,4';3',4)$ in Eq (3.4) is a functional derivative

$$\Xi(3,4';3',4) = \frac{\delta\Sigma_{xc}(3,3')}{\delta G_1(4,4')} \tag{3.5}$$

Which can be approximated as

$$\Xi(3,4';3',4) \approx -i\delta(3,3')\delta(4^+,3')V(3,4) + i\delta(3,4)\delta(3',4')W(3^+,3') \tag{3.6}$$

where V is the Coulomb interaction and W is the screened Coulomb interaction introduced in Eq. (2.12c).

The Fourier transformation of the terms related to the particle-hole excitations of L can be written as[50,53]

$$L^{ph}(\mathbf{r}_1,\mathbf{r}_2;\mathbf{r}_{1'},\mathbf{r}_{2'}\,|\,t_1,t_{1'};\omega) = \int_{-\infty}^{\infty} dt_2 \exp(-i\omega t_2) L^{ph}(\mathbf{r}_1 t_1,\mathbf{r}_2 t_2;\mathbf{r}_{1'} t_{1'},\mathbf{r}_{2'} t_2^+)$$

$$= -i\exp\left(-i\omega\left(t^1 - \frac{1}{2}|\tau_1|\right)\right)\sum_q \frac{\chi_q(\mathbf{r}_1,\mathbf{r}_{1'};\tau_1)\tilde{\chi}_q(\mathbf{r}_2,\mathbf{r}_{2'};-\delta)}{\omega - \Omega_q + i\eta}\exp\left[-\frac{1}{2}i\Omega_q|\tau_1|\right]$$

$$+i\exp\left(-i\omega\left(t^1 + \frac{1}{2}|\tau_1|\right)\right)\sum_q \frac{\chi_q(\mathbf{r}_2,\mathbf{r}_{2'};-\delta)\tilde{\chi}_q(\mathbf{r}_1,\mathbf{r}_{1'};\tau_1)}{\omega + \Omega_q - i\eta}\exp\left[-\frac{1}{2}i\Omega_q|\tau_1|\right] \tag{3.7}$$

where the time-dependent variables have been reorganized as

$$t^1=\frac{t_1+t_{1'}}{2}, t^2=\frac{t_2+t_{2'}}{2}, \tau_1=t_1-t_{1'}, \tau_2=t_2-t_{2'}. \tag{3.8}$$

t_2^+ means $t_2+\delta$ with $\delta\to 0^+$. Here Ω_q and $\chi_q\left(\mathbf{r}_i,\mathbf{r}_j;t_i-t_j\right)$ denote the energy and particle-hole amplitude of the qth excitation. With the quasiparticle approximation, χ_q can be expressed as

$$\chi_q\left(\mathbf{r},\mathbf{r}';\tau\right)\approx\exp\left(\frac{i\Omega_q|\tau|}{2}\right)\sum_{v',c'}\left\{\begin{array}{l}A^q_{v'c'}\varphi_{c'}\left(\mathbf{r}\right)\varphi^*_{v'}\left(\mathbf{r}'\right)\\ \times\left\{\exp\left[-i\left(E_{c'}-i\gamma_{c'}\right)\tau\right]\theta\left(\tau\right)-\exp\left[-i\left(E_{v'}+i\gamma_{v'}\right)\tau\right]\theta\left(-\tau\right)\right\}\end{array}\right\} \tag{3.9}$$

where $\mathbf{A}^q_{vc}$ in Eq. (3.9) is the eigenvector corresponding to χ_q. Note that the finite QP lifetimes have been taken into account in Eq. (3.9). This approach has been applied to the study of the dynamics of core-excitons in semiconductors by Strinati.[54]

By substituting Eqs. (3.6), (3.7) and (3.9) into Eq. (3.4) and projecting both sides onto $\varphi_c\left(\mathbf{x}_1\right)\varphi^*_{v'}\left(\mathbf{x}_{1'}\right)\chi_r\left(\mathbf{x}_2,\mathbf{x}_{2'};-\delta\right)$, the BSE Eq. (3.4) can be converted to a complex eigenvalue problem

$$\left[\left(E_c-i\gamma_c\right)-\left(E_v+i\gamma_v\right)\right]A^q_{vc}+\sum_{v',c'}A^q_{v'c'}\left(K^x_{vcv'c'}+K^d_{vcv'c'}\right)=\left(\Omega_q-i\Gamma_q\right)A^q_{vc} \tag{3.10}$$

where Ω_q and Γ_q in the right hand side of Eq. (3.10) are the real and imaginary energies of the qth exciton. In this study, only singlet excitations are considered, and thus the exchange term $K^x_{vcv'c'}$ in Eq. (3.10) is evaluated as $2\left\langle\varphi_v\varphi_c\middle|V\middle|\varphi_{v'}\varphi_{c'}\right\rangle$. The direct interaction term $K^d_{vcv'c'}$ in Eq. (3.10) can be calculated as

$$\begin{array}{l}K^d_{vcv'c'}=-\left\langle\varphi_v\varphi_{v'}\middle|V\middle|\varphi_c\varphi_{c'}\right\rangle\\ -\sum_s\left\{\begin{array}{l}\left(\dfrac{1}{\Omega_q-i\Gamma_q-\omega_s-\left(E_{c'}-E_v\right)}+\dfrac{1}{\Omega_q-i\Gamma_q-\omega_s-\left(E_c-E_{v'}\right)}\right)\\ \times\left(\left\langle\varphi_v\varphi_{v'}\middle|V\middle|\rho_s\right\rangle\left\langle\rho_s\middle|\left(V+f_{xc}\right)\middle|\varphi_c\varphi_{c'}\right\rangle+\left\langle\varphi_v\varphi_{v'}\middle|\left(V+f_{xc}\right)\middle|\rho_s\right\rangle\left\langle\rho_s\middle|V\middle|\varphi_c\varphi_{c'}\right\rangle\right)\end{array}\right\}\end{array} \tag{3.11}$$

where the screened interaction

$$W = V + \left[(V + f_{xc}) \Pi V + V \Pi (V + f_{xc}) \right] / 2 \tag{3.12}$$

has been substituted into Eq. (3.11). Note that W (the screened Coulomb interaction defined in Chap. 2) is written in a symmetric form, since the local exchange-correlation effect f_{xc} has to be included to make Eq. (3.10) consistent with the one-particle calculation implemented with the TDLDA/*GW*Γ method. In Eq. (3.10), only the resonant part is taken into account, while the anti-resonant part is neglected. This is the Tamm-Dancoff approximation (TDA), whose effect on the excitonic energies is found to be negligible.[49] Usually ω_s and ρ_s come from the reducible polarizability Π obtained by TDLDA.

3.2.3 Feynman Diagrams

Solution of the complex eigenvalue $\Omega_q - i\Gamma_q$ through Eq. (3.10) simultaneously determines the excitation energy Ω_q and the relaxation rate Γ_q of the qth exciton. Actually Eq. (3.10) explicitly includes four terms related to the decay of the exciton, which are illustrated by the Feynman diagrams in Fig. 3-2.

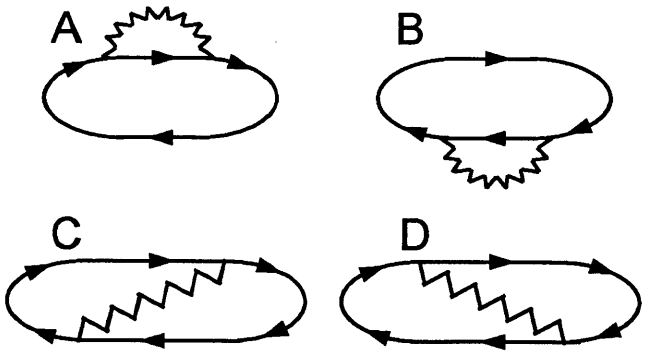

Figure 3-2. Feynman diagrams of terms in Eq. (3.10) related to the decay of the particle-hole excitations. Arrowed lines are Green's functions. Wiggled lines are screened interactions. Diagrams A and B correspond to the diagonal elements in Eq. (3.10). Diagrams C and D denote the screened particle-hole interaction in Eq. (3.11).

However, it is unfeasible to solve the DBSE Eq. (3.10) directly, since the matrix on the left hand side is explicitly dependent on the eigenvalues Ω_q to be solved. Thus Eq. (3.10) is usually simplified by taking the two approximations

$$\Gamma_q = \gamma_c = \gamma_v = 0, \tag{3.13a}$$

$$\Omega_q \approx E_{c'} - E_v \approx E_c - E_{v'}, \tag{3.13b}$$

which simplifies Eq. (3.10) to to an frequency-independent eigen-problem, as now the left hand side is not dependent on Ω_q and Γ_q any more. Thus the original equation becomes a static equation, namely the static BSE (SBSE). The reducible polarizability $\tilde{\Pi}$ obtained from SBSE can be written in the same way as that from TDLDA

$$\tilde{\Pi}(\mathbf{r},\mathbf{r}';E) = 2\sum_q \left[\frac{\tilde{\rho}_q(\mathbf{r})\tilde{\rho}_q(\mathbf{r}')}{E-(\Omega_q - i0^+)} - \frac{\tilde{\rho}_q(\mathbf{r})\tilde{\rho}_q(\mathbf{r}')}{E+(\Omega_q - i0^+)} \right] \tag{3.14}$$

where the particle-hole amplitudes $\tilde{\rho}_q(\mathbf{r}) = \chi_q(\mathbf{r},\mathbf{r};t=0)$ and the tilde distinguishes the results of the BSE from those of the TDLDA. Note that in most cases $\tilde{\Pi}$ in Eq. (3.14) is different from Π in Eq. (2.19). The issue for the self-consistency of the reducible polarizability Π will be discussed later in this chapter.

3.3 Numerical Details

In chapter 2, Mg clusters have been used as examples to illustrate the method developed for the electronic inelastic scattering rates in finite 0D nanoclusters. Whereas, in the following chapters (Chaps. 4, 5 and 6), several semiconductor nanoclusters and molecules are to be investigated. Therefore, in this chapter, a semiconductor nanocluster, Si_{20}, will be simulated to demonstrate the methods developed in Chaps. 2 and 3 for the electronic and excitonic inelastic scattering rates

in finite 0D nanoclusters. We do not choose larger clusters in this chapter, since we will solve the dynamic BSE as the benchmark for our simplification strategy. This is an extremely time consuming process and it is feasible only for small clusters.

An LDA calculation for the ground state of Si_{20} is performed using the SIESTA code.[35] The core electrons [$1s^2 2s^2 2p^6$] of Si are replaced by the nonlocal norm-conserving pseudopotential based on the Troullier-Martins scheme.[36] A triple-ζ-function and single-polarization-function (TZP) basis set of numerical atomic orbitals is used for the valance electrons of Si. Two stable geometric configurations of Si_{20} have been reported in literatures, one with the C_{3v} symmetry (Fig. 3-3a)[55,56] and the other with the C_{2h} symmetry (Fig. 3-3b)[57]. The former has been shown to be more stable by the DFT with generalized gradient approximation (GGA) functionals, the DFT with hybrid functionals and the coupled-cluster CCSD(T) method. In this work, both configurations are calculated via DFT with LDA, and we find that the energy of the C_{3v} isomer is about 0.2 eV lower than the C_{2h} one. Thus all numerical work and discussion in the remaining part of this thesis will focus on the structure as shown in Fig. 3-3a.

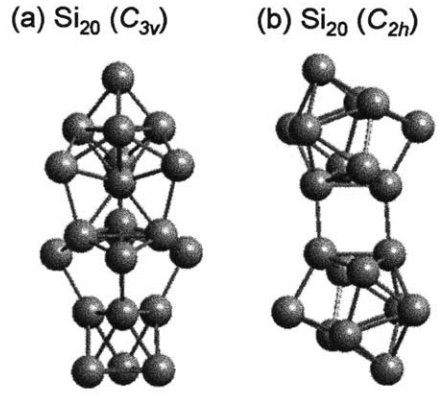

Figure 3-3. Optimized structures of two isomers of Si_{20}. The labels in parentheses correspond to the point group symmetries of the clusters.

All integrals are evaluated on a uniform grid in real space with a grid spacing of 0.5 a.u., which has been tested to give QP energies with an accuracy of 0.1 eV. The

exchange integrals $\int d\mathbf{r}\int d\mathbf{r}'\varphi_i(\mathbf{r})\varphi_j(\mathbf{r})V(\mathbf{r},\mathbf{r}')\varphi_k(\mathbf{r}')\varphi_l(\mathbf{r}')$ are evaluated by first solving Poisson equations with the multigrid method.[37] Here $V(\mathbf{r},\mathbf{r}')$ is the Coulomb interaction. The convergence of the quasiparticle calculation usually requires a large number of unoccupied states for the evaluation of the polarizability. Thus a Coulomb-hole screened-exchange (COHSEX) remainder scheme[33] has been applied to accelerate the convergence of the correlation part $\langle\varphi_i|\Sigma_c|\varphi_i\rangle$.

The properties of the one-particle states are obtained by solving the quasiparticle equation Eq. (2.9) introduced in Chap. 2

$$\left(\hat{T}+V_{ext}+V_H\right)\varphi_i(\mathbf{r})+\int d\mathbf{r}'\Sigma_{xc}(\mathbf{r},\mathbf{r}';E_i)\varphi_i(\mathbf{r}')=E_i\varphi_i(\mathbf{r}) \tag{3.15}$$

where $\hat{T}$ is the electron kinetic energy, V_{ext} is the external potential and V_H is the Hartree potential. After applying analytical continuation of $\Sigma_c(\mathbf{r},\mathbf{r}';E)$ in the complex energy plane, the energy E_i and the inelastic scattering rates γ_i of an electronic state are obtained by solving a complex equation set numerically

$$\mathrm{Re}\langle\varphi_i|\Sigma_{xc}(E_i-i\eta_i\gamma_i)|\varphi_i\rangle-\langle\varphi_i|V_{xc}|\varphi_i\rangle=E_i-\varepsilon_i \tag{3.16a}$$

$$\left|\mathrm{Im}\langle\varphi_i|\Sigma_{xc}(E_i-i\eta_i\gamma_i)|\varphi_i\rangle\right|=\gamma_i \tag{3.16b}$$

3.4 Results and discussion

3.4.1 Self-consistency of G and Π

In the last chapter, we have demonstrated that it is necessary to implement the self-consistency of one-particle Green's function G for calculation of electronic inelastic decay rates in finite systems.[58] The reason is restated briefly here. The inelastic decay rate of the ith QP can be written as a summation S_i

$$S_i = 2\left|\sum_n \sum_s \frac{a_{n,s,i}\gamma_i}{\left(E_i - E_n - \omega_s\eta_n\right)^2 + \gamma_i^2}\right|. \tag{3.17}$$

Replacing G with G_0 changes the positions of the poles from $E_n + \omega_s\eta_n$ to $\varepsilon_n + \omega_s\eta_n$, which may cause considerable error to S_i, since S_i is mostly determined by the arrangement of the poles in the vicinity of E_i. The effect is illustrated schematically in Fig. 3-4, where unoccupied (occupied) energy levels ε_n's obtained by DFT are shifted up (down) to yield the QP energy levels E_n's. Yet the poles $\varepsilon_n + \omega_s\eta_n$ are not moved together, leading to misplaced poles around a given energy level E_i.

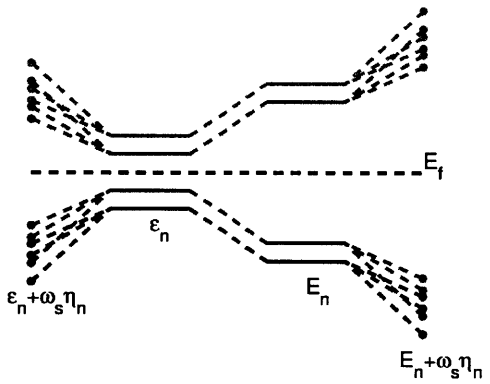

Figure 3-4. Schematic plot for the relation among the DFT energies ε_n and hence the derived poles $\varepsilon_n + \omega_s\eta_n$, the QP energies E_n and hence the derived poles $E_n + \omega_s\eta_n$. Each color defines a set including an energy level and poles accompanying the energy level. To maintain correct orders, E_n should be used together with correct poles $E_n + \omega_s\eta_n$. A mixture between E_n and $\varepsilon_n + \omega_s\eta_n$ changes the pole arrangement in the vicinity of a QP energy level, which may introduce notable errors for the QP lifetimes.

In one of our papers,[58] we only implement the iteration $(G \to \Sigma_{xc} \to G)$, with the

assumption that $\Pi \equiv \Pi_{TDLDA}$. Herein, we further extend our investigation about the self-consistency of Π. The reason for the implementation of the self-consistency of Π is similar to that of G. Since the inelastic decay rate of qth exciton can be written as a summation $\tilde{S}_q$, which also has a set of poles. Replacing Ω_s by ω_s thus changes the positions of the poles, and causes error to $\tilde{S}_q$.

Note that G is related to all one-particle properties, namely QP energies E_n in Σ_{xc}, and QP energy differences $(E_c - E_v)$ in the BSE kernel K. While Π is related to all two-particle properties, namely excitonic energies Ω_s in both Σ_{xc} and K. If two different data sets (G', Π') and (G'', Π'') are used for Σ_{xc} and K, respectively, numerical inconsistency will occur. This implies that the same G and Π shall be used in the calculation of Σ_{xc} and K, which brings about a self-consistent issue at a higher level, namely a cycle $(G,\Pi) \to (\Sigma_{xc}, K) \to (G,\Pi)$. The relation of the three self-consistent cycles are illustrated in Fig. 3-5, where the bold lines indicate the iterative steps. The left part is the G cycle, where the self-consistent G is solved with Π as an argument. The right part is the Π cycle, where the self-consistent Π is solved with G as an argument. The central part is the $G\Pi$ cycle, which indicates the convergence of all of the four quantities. This cycle is implemented in the way $G(\Pi) \to \Pi(G) \to G(\Pi) \to \Pi(G) \to \cdots$, until the simultaneous convergence of both G and Π.

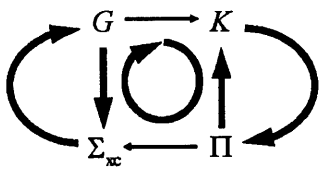

Figure 3-5. Schematic plot for the three self-consistent cycles. Bold lines indicate iterative steps. The left part $G \to \Sigma_{xc}(\Pi) \to G \to \cdots$ is the G cycle. The right part

$\Pi \to K(G) \to \Pi \to \cdots$ is the Π cycle. The central part is the $G\Pi$ cycle which is implemented in the way $G(\Pi) \to \Pi(G) \to G(\Pi) \to \Pi(G) \to \cdots$, until the simultaneous convergence of both G and Π.

The criteria for the convergence of G and Π are required for the numerical implementation. According to Eq. (2.6), G is characterized by the QP wavefunctions $\varphi_n(\mathbf{r})$ and the energies E_n. Usually the QP wavefunctions can be assumed to be identical to the LDA wavefunctions, then the convergence of G is simplified to the convergence of E_n. Similarly, the polarizability Π is characterized by the amplitudes $\rho_s(\mathbf{r})$ and the energies Ω_s. However, the convergence of Π has not been well studied. Here we test two possible implementations: the full self-consistency (FSC) and the partial self-consistency (PSC). In the FSC strategy, both the convergence of $\rho_s(\mathbf{r})$ and Ω_s are pursued, while in the PSC, only the energies Ω_s are updated in each iteration, with $\rho_s(\mathbf{r})$ fixed to the TDLDA amplitudes. The latter essentially takes the BSE kernel as a first order correction to the TDLDA kernel, which is an analogy to the assumption made in the QP calculations in Chap. 2 that the QP wavefunctions and the DFT wavefunctions are identical. Note that only the static BSE is used in both the FSC and PSC tests, since the dynamic BSE is much more time-consuming, and only has a minor effect on the excitonic energies Ω_s.

The QP energies and optical spectra obtained by the FSC implementation are shown in the top and bottom diagrams of Fig. 3-6. The arrows between the two diagrams signify the order of each numerical step. It is found that the QP energies shift toward the Fermi level as the iteration progresses. Also, the optical spectra change dramatically between two consecutive iterative steps. Both diagrams indicate that the FSC is numerically unstable. On the other hand, results obtained by the PSC implementation are more stable, as shown in Fig. 3-7 with the same style as Fig. 3-6.

In PSC both the QP energies and optical spectra change only slightly after each iterative step, and converge after 2-3 cycles. Therefore our discussion about the properties of QPs and excitons in the following sections will focus on the results calculated by the PSC method.

The difference between the PSC and FSC methods in calculation is that: the amplitudes $\rho_s(\mathbf{r})$ in PSC are fixed to TDLDA values during each iterative step, while the amplitudes are not in FSC. Thus we analyze the $\rho_s(\mathbf{r})$ calculated by TDLDA and those obtained by SBSE to reveal the crucial role of the issue. In Fig. 3-8, the weights of largest transition components of the first three excitations calculated by the TDLDA and SBSE are illustrated. It can be seen from Fig. 3-8 that both the TDLDA kernel and the SBSE kernel tend to mix the independent-particle transitions. The tendency of the mixture is much stronger in the case of SBSE, as the weight of the largest transition component of each SBSE exciton is smaller than that of the corresponding TDLDA exciton. This effect has been reported for BSE calculations of various systems.[52,59] It is speculated that the numerical instability of the FSC implementation could be attributed to the differences of the transition weights obtained by TDLDA and BSE. In fact, each amplitude $\rho_s(\mathbf{r})$ corresponds to a vector $\mathbf{R}_s$, and the reducible polarizability Π is a set composed of such vectors. This means that any quantity depending on Π is essentially a function of these vectors. Since TDLDA and BSE are based on different frameworks (independent-particle vs. quasiparticle), their vector sets also differ from each other, as can be seen in Fig. 3-8. Change from the TDLDA vector set to the BSE vector set seems to be too large for the iteration to remain in the numerical stability domain.

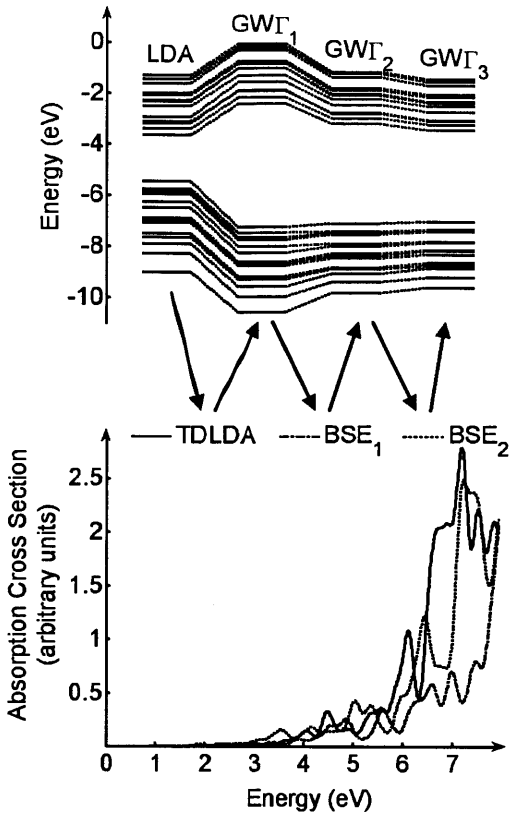

Figure 3-6. QP energies (top) and optical spectra (bottom) obtained by the FSC implementation. The arrows between the two diagrams signify the order of each numerical step, namely LDA-TDLDA-GWΓ-BSE- GWΓ-BSE-GWΓ.

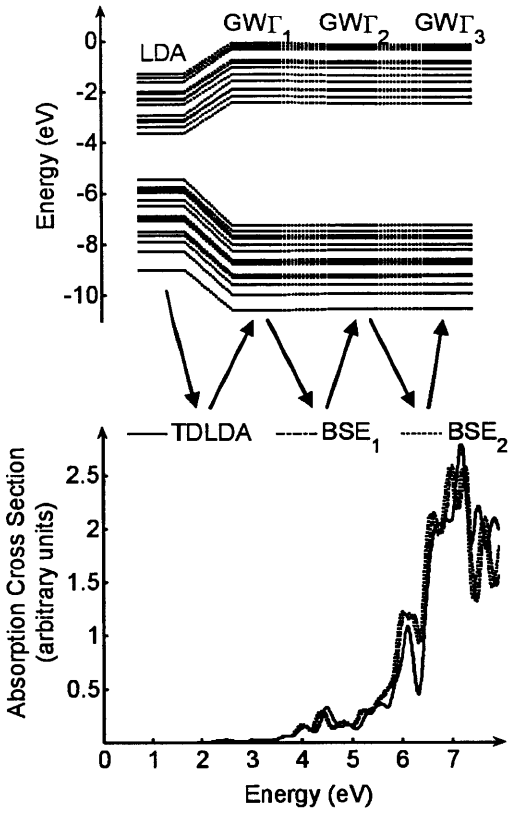

Figure 3-7. QP energies (top) and optical spectra (bottom) obtained by the PSC implementation. Plotted in the same style as Fig. 3-6.

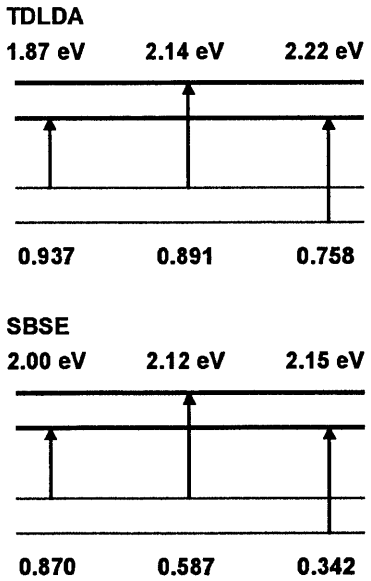

Figure 3-8. Weights of the largest transition components of the first three excitons obtained by TDLDA and static BSE. Excitonic energies are also given at the top. Bold lines stand for degenerate E states, slim lines stand for non-degenerate A_1 states.

3.4.2 QP energies and lifetimes in Si_{20}

The QP energies in Si_{20} as calculated by the *GWΓ* method have been illustrated in Fig. 3-7. The vertical ionization potential obtained by LDA is 5.46 eV, while it is adjusted to 7.22 eV by the *GWΓ* method. This number is close to the experimental data (7.46–7.53 eV).[60]

Inelastic lifetimes τ_i of hot electrons and holes in Si_{20} are plotted versus the excitation energy $|E_i - E_F|$ in Fig. 3-9a. In a high-density free electron gas (FEG), lifetimes of hot electrons with low excitation energies follow an inverse quadratic energy dependence law according to Quinn and Ferell.[19]

$$\tau_i^{QF} = 263 r_s^{-5/2} (E_i - E_F)^{-2} \text{ eV}^2 \text{ fs}. \tag{3.18}$$

where r_s is the electron-density parameter defined as $1/\bar{n} = (4/3)\pi r_s^3$, with $\bar{n}$ being the average electron density. Eq. (3.18) implies a constant scaled lifetime $\tau_i (E_i - E_F)^2$ for all hot electrons in the FEG. Therefore we plot the scaled lifetimes of both electrons and holes as a reference in Fig 3-9b, although silicon is a semiconductor with a spatially non-uniform electron gas due to covalent bonds. We find that the scaled hole lifetimes with low excitation energies ($|E_i - E_F| < 6.2$ eV) are longer than those with high excitation energies ($|E_i - E_F| \geq 6.2$ eV), and so do the scaled electron lifetimes (with one exception) behave in the same way. This feature is strikingly similar to that of the metallic cluster Mg_{40} simulated by the same method,[58] where a low energy regime (R_{LE}) and a high energy regime (R_{HE}) have also been observed. The similarity between the QP lifetimes in bulk silicon and those in the jellium model has also been demonstrated by Fleszar and Hanke.[61] The same feature has been observed for Mg_{40}, where the QP scaled lifetimes in the R_{LE} are longer than those in the R_{HE}, and the reason is also attributed to the lack of electronic states around the Fermi level available for the transitions of hot electrons (holes).

In the regime R_{HE}, the scaled lifetimes of hot electrons fluctuate in the range of 90 to 150 fs eV^2, with an average of 104 fs eV^2. The scaled lifetimes of hot holes in this regime approach 30 fs eV^2 smoothly with increasing $|E_i - E_F|$. QP lifetimes in bulk silicon have been calculated in Ref. 61 and 62. According to Fig. 2 in Ref. 62, the scaled lifetimes of electrons and holes are estimated to be 120 and 40 fs eV^2 respectively, which are close to the results obtained in this study. This implies that even in a cluster as small as Si_{20}, the scaled QP lifetimes in the R_{HE} have already approached the corresponding bulk values. The notably shorter lifetimes of hot holes than those of hot electrons with the same $|E_i - E_F|$, can be attributed to the smaller angular momentums of holes, or to the greater overlap among different hole states, which leads to more possible transitions than for electrons. This is an analogy to the behavior of the bulk, where one can attribute shorter hole lifetimes in simple *s-p* systems (no localized *d*-states) to the smaller momenta of holes.[42]

It is interesting to compare the semiconductor cluster Si_{20} simulated in this study with the metallic cluster Mg_{40} studied in Chap. 2, since both clusters have the same number of valence electrons. In Mg_{40}, the scaled lifetimes of hot electrons fluctuate in the range of 21 to 24 fs eV^2, while those of hot holes are around 12 fs eV^2 and decrease slightly with increasing excitation energy $|E_i - E_F|$. The results indicate that at the same excitation energy $|E_i - E_F|$, the scaled QP lifetimes in Mg_{40} are shorter than those in Si_{20}. One reason for this phenomenon is the larger HOMO-LUMO gap in Si_{20} than that in Mg_{40}, which leads to fewer energy states, or decaying channels, for QPs in Si_{20}. However, even if one takes this issue into account by redefining the excitation energy as $E_i - E_{LUMO}$ and $E_{HOMO} - E_i$ for electrons and holes, the QP inelastic scattering lifetimes in Si_{20} are still longer, which can be explained by the higher electron density in Si_{20} and thus the stronger screening effects. The statement can be verified by calculating the valence-electron densities in the two materials, which are 8.6×10^{22} cm^{-3} for bulk Mg, and 20.0×10^{22} cm^{-3} for bulk silicon.

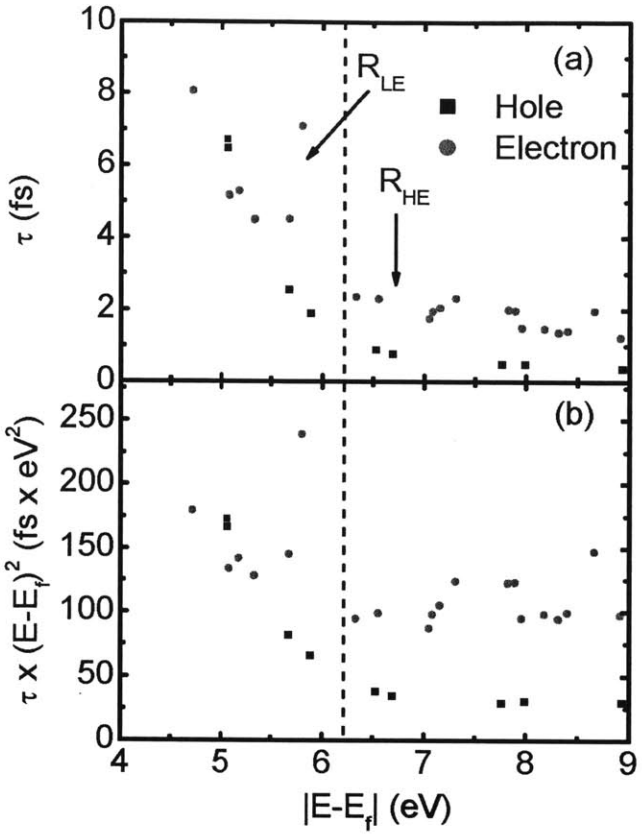

Figure 3-9. Energy dependence of both the a) QP lifetimes and b) scaled QP lifetimes in Si_{20} obtained by the self-consistent $GW\Gamma$ approach. The vertical dashed line separates both plots into a low-energy regime and a high-energy regime.

3.4.3 Excitonic energies and lifetimes in Si_{20}

The final excitonic energies and lifetimes are calculated using Eq. (3.10), in the partially self-consistent way as has been implemented in Chap. 3.4.1. Thus only complex eigenvalues are updated iteratively by the frequency-dependent DBSE matrix elements, with eigenvectors fixed to the TDLDA amplitudes. To accelerate and stabilize the self-consistency procedure, the initial guess for the imaginary part of the excitation energy Γ_r for a given exciton is taken as

$$\Gamma_r = \sum_{v,c} \left| R_{vc}^r \right|^2 (\gamma_c + \gamma_v) \tag{3.19}$$

The absorption spectra calculated by DBSE and SBSE, both with partial self-consistency, are plotted in Fig. 3-10. Since the cluster Si_{20} is a prolate cluster with C_{3v} symmetry as shown in Fig. 3-3a, it exhibits A_1 transitions (electric dipole perturbation along the z-axis) and E transitions (electric dipole perturbation within the xy-plane) with an energy dependence, which are illustrated in Figs. 3-10a and 3-10b, respectively. As shown in Fig. 3-10, the absorptive features of the A_1 transitions emerge in a lower energy regime than the E transitions, which is attributed to the larger dimension and thus less electronic confinement along the z-axis than those along the x and y-axes. On the other hand, the DBSE and SBSE absorption spectra for each irreducible representation are similar, indicating the negligible influence of the dynamic screening effect on the excitonic energies. This observation is demonstrated more clearly in Fig. 3-11 by plotting the energy differences between the DBSE and SBSE contributions arising from the second term in Eq. (3.11), where the two methods are different from each other. As shown in Fig. 3-11, the energy differences vary from -0.2 to 0.1 eV, with the average of -0.07 eV, which is negligible. These results demonstrate the feasibility of using the SBSE calculation technique, which has been widely used for simulations of excitonic energies in bulk materials (3D),[63,64] graphene (2D),[65,66] carbon nanotubes (1D),[67,68] molecules and clusters (0D).[69,70]

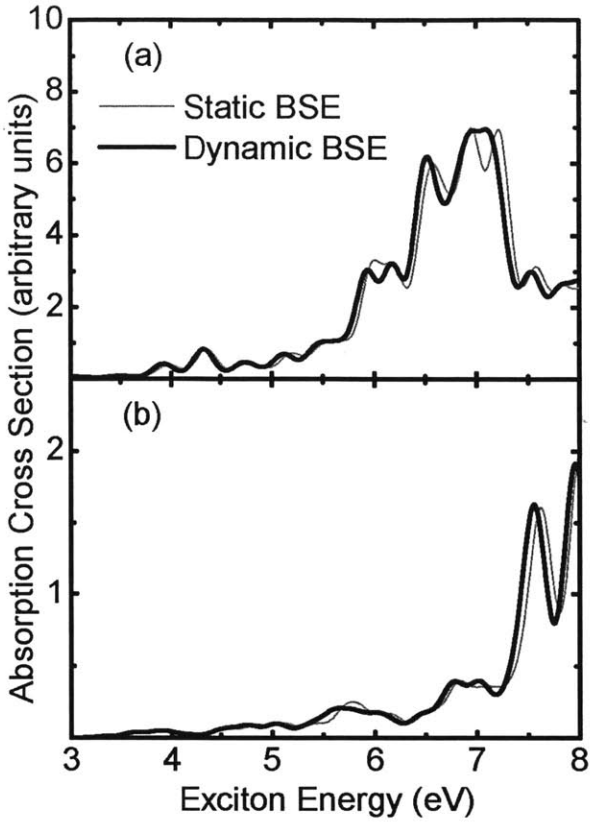

Figure 3-10. Absorption spectra of a) A1 transitions and b) E transitions calculated by the dynamic and static BSE, both with partial self-consistency. Absorption lines are broadened by Gaussian lineshapes with a spectral width of 0.1 eV.

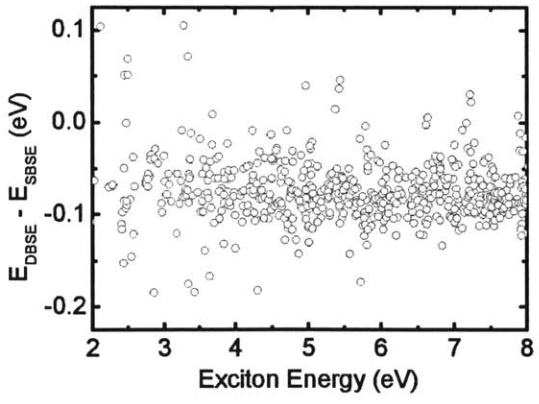

Figure 3-11. Energy differences between the DBSE and SBSE contribution arising from the second term in Eq. (3.11), with the negative sign included.

The excitonic inelastic scattering rates (MEG rates) Γ_r of A_1 and E transitions vs. excitonic energies Ω_r are plotted in log-log style in Fig. 3-12. Although the two transition modes differ in terms of the positions of major absorption peaks, their decay-rate patterns almost coincide with each other. The results indicate that the excitonic lifetimes are geometry-insensitive, and are solely determined by the excitation energy. We fit the data point with a simple rational function (Padé function P_1^2)

$$y = 2x + a + \frac{b}{x+c} \tag{3.20}$$

where x and y represent $\ln(\Omega/\mathrm{eV})$ and $\ln(\Gamma/\mathrm{eV})$, respectively. The fitting coefficients a, b and c are -4.49, -0.98 and -1.19. Here the coefficient of the linear term is fixed to be 2, since it is easy to prove that the quadratic relation between the excitonic decay rate and the excitonic energy will be approached at the high-energy limit (large x) for both single-particle excitations and collective excitations, provided that the quadratic relation between the QP decay rate and the QP energy is approached at the high-energy regime as in this case. According to Eq. (3.20), excitons with energies of 5.0, 6.0 and 7.0 eV shall have lifetimes 12, 4.2, 2.2 fs, respectively. The results provide a general picture about the multiple exciton generation rates: the process occurs on a time scale of several to several tens of femtoseconds in the silicon cluster Si_{20} that was investigated.

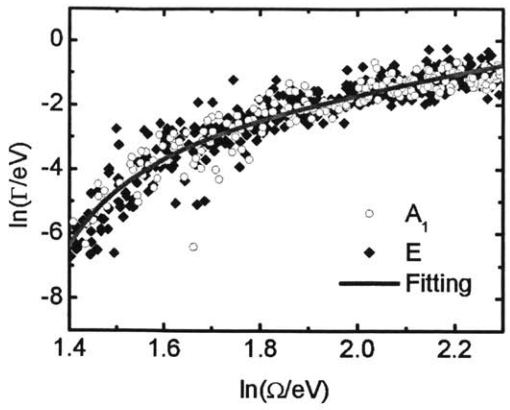

Figure 3-12. Log-Log plot of the excitonic inelastic decay rates Γ_r of A_1 and E transitions vs. excitonic energies Ω_r. The solid line is the rational curve-fitting of the data points.

The most interesting implication is how the estimated excitonic decay rates based on Eq. (3.19) differ from those obtained by solving the dynamic BSE. If the results calculated by the two approaches are close, then Eq. (3.19) can be used to replace DBSE in the calculation of excitonic lifetimes. This can reduce the computational time dramatically. Actually the difference of the two approaches can be understood in terms of Feynman diagrams: Eq. (3.19) only takes into account the first two diagrams in Fig. 3-2, while the dynamic BSE applied in this paper includes all of the four diagrams in Fig. 3-2.

The ratios of the excitonic inelastic decay rates calculated with DBSE over those obtained with Eq. (3.19) are plotted as a function of the excitonic energies in Fig. 3-12, where the ratios are again geometrically insensitive according to the patterns of the A_1 and E transitions. Furthermore, one can find that for excitons in the high-energy regime ($\Omega_r > 4.5$ eV), the ratios of their inelastic excitonic decay rates can be fitted by a constant (0.966) as shown by the horizontal solid line in that figure. The number for this ratio is close to unity, indicating that Eq. (3.19) is a very good approximation to the DBSE results for excitonic decay rates in the high-energy regime. The fitted constant is slightly smaller than unity, meaning that the inclusion of the dynamic

screening effect (the last two diagrams in Fig. 3-2) reduces the excitonic decay rates for most excitons. This is similar to the conclusion in Ref. 54, where the core-excitation width Γ is predicted to be smaller than the core-hole width γ by inclusion of the dynamic screening effects when solving the BSE. Note that the MEG effect can only be observed for incident photons with energies larger than twice the optical bandgap. For Si_{20} the optical bandgaps obtained by different methods (TDLDA, SBSE and DBSE) are around 2.0 eV, which means that the excitonic MEG energy threshold should be about 4.0 eV. Therefore the lower values in Fig. 3-13 located around 4.0 eV indicate that the approximation method tends to overestimate the excitonic inelastic scattering rates, especially near the MEG energy threshold, with the maximum factor of about 1.9 in our case.

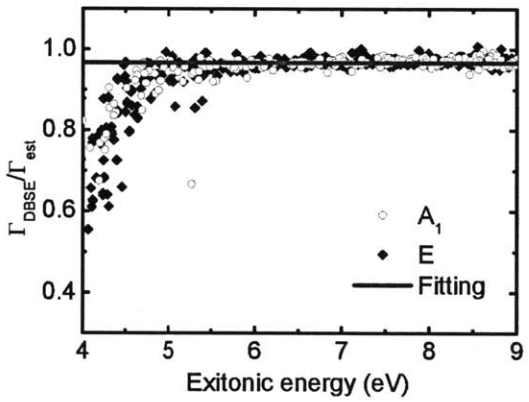

Figure 3-13. Ratios of the excitonic inelastic decay rates calculated with DBSE over those estimated by Eq. (3-19) for A_1 and E transitions. The solid line is the constant curve-fitting of the data points in the high-energy regime.

3.5 Conclusion

In this study, the excitonic inelastic decay rates in a semiconductor nanocluster Si_{20} are investigated by the dynamic Bethe-Salpeter equation (DBSE). A simplification strategy is proposed for the estimation of the excitonic inelastic scattering rates. The results obtained by the simplification strategy are demonstrated to be very close to those obtained by DBSE. With much less computational cost than DBSE, the

simplification strategy thus provides a fast way for accurate calculations of excitonic inelastic scattering rates. This simplification strategy can be widely used for calculations of excitonic inelastic scattering rates in larger systems. Without the simplification, calculations for inelastic scattering rates in such systems are essentially infeasible.

The implementations of the self-consistencies of the one-particle Green's function G and the reducible polarizability Π within the framework of the many-body Green's-function theory are discussed. The one-particle Green's function G contains energies and wavefunctions of all one-particle states. The reducible polarizability Π for excitonic transitions contains all energies and wavefunctions of all two-particle states. In many-body Green's function theory, G and Π are mutually dependent on each other. The full self-consistency of Π, where both the amplitudes $\rho_s(\mathbf{r})$ and the energies Ω_s are allowed to relax, is numerically unstable. On the other hand, the partial self-consistency of Π is stable where only the energies Ω_s are allowed to relax. Therefore the later one is suggested as a stable numerical routine.

Chapter 4

Nonradiative relaxation rates of electrons and excitons in nanoclusters

4.1 Introduction

4.1.1 Single-phonon process vs. multiple-phonon process

The energy exchange rate between electrons and phonons plays a key role for photovoltaic devices. This energy exchange rate corresponds to the heat transfer rate between the working fluid and the cylinder/piston in the heat engine analogy. Actually phonon-assisted relaxation of the electronic states is a general phenomenon observed in almost all materials, including metals, semiconductors and organic molecules. The phenomenon is of great interest and it has attracted attentions from both the physics and chemistry researchers. It should be emphasized that the term "nonradiative relaxation" may stand for different processes under different circumstances. In this chapter, it is further categorized as a single-phonon relaxation process and a multi-phonon relaxation process.

The single-phonon process means that an electron makes a phonon-assisted transition from one electronic state transits to another electronic state, with the electron emitting or absorbing a phonon at the same time. For physicists, the theoretical work on this process originates from the investigation of the temperature-dependence of the optical gaps of bulk silicon and germanium. This process leads to the broadening of the electronic states in semiconductors. The formula associated with this process was first developed by Fan in 1951.[71] Thus the derived electron-phonon self-energy term is called the "Fan" term, and the imaginary part of the Fan term is exactly the single-phonon relaxation rate. Note that the

temperature effect also manifests itself through the thermal expansion of the crystal lattice, and through a Debye–Waller term corresponding to the elastic interaction between electrons and phonons.[72] However, the thermal expansion and Debye-Waller terms only influence the real parts of the electronic energies, but do not contribute to their imaginary parts. This means that the two effects are irrelevant for describing the finite lifetimes of electronic states, and will not be covered in this thesis.

The multiple-phonon process means that an electron in one electronic state makes a transition to another electronic state, with the quantum numbers of several coupled phonon modes changed at the same time. In chemical terms, the theoretical work describing this electronic process originates from the investigation of nonradiative transitions of electronic states in large molecules.[73] Usually the energy gap between the first two electronic states is so large that it can not be matched just by the energy of one phonon. Therefore a process involving multiple phonons is the only possible relaxation mechanism. The formulas for the transition rates have been developed based on the perturbation theory. It should be pointed out that the anharmonic effect has to be taken into account for multiple-phonon processes, and such processes are attributed to the displacement of the potential energy surface during the electronic transitions.[74]

Physical and chemical researches have tackled the electron-phonon interaction from different aspects, as they are facing different problems and objectives. Now the question is which aspect should we follow for the electron-phonon interaction in a semiconductor nanocluster. A cluster is more like a bulk material so we should focus on a single-phonon process, or if it is more like a molecule then we should focus on a multiple-phonon process. The question has not been addressed in literature until the work of this thesis. In this thesis, we suggest that both mechanisms should be included. Because a nanocluster is essentially the transition form between a bulk material and a molecule, it has all features of both forms.

The fact can be understood more readily with the schematic energy diagram of a

semiconductor nanocluster as shown in Fig. 4-1. In this cluster, an electron in the electronic state on the top can jump to those states right below it through a single-phonon process, as the energy gaps between these states and the top one are smaller than the energy of one phonon ω_k. On the other hand, the electron in the electronic state on the top also can jump to those states far below it through a multiple-phonon process, since now the energy gaps between these states and the top one are so large that single-phonon process is prohibited. According to Fig. 4-1, we find that the final states available for a single-phonon process are fewer than those for a multiple-phonon process. However, the single-phonon process is usually faster than the multiple-phonon process. Therefore the contributions of the single-phonon process and multiple-phonon process to the overall nonradiative relaxation rate of a high energy state are predicted to be comparable in magnitude. This also supports our speculation that it is important to include both the single-phonon and the multiple-phonon mechanisms for the calculation of nonradiative relaxation rates of electronic states in nanoclusters.

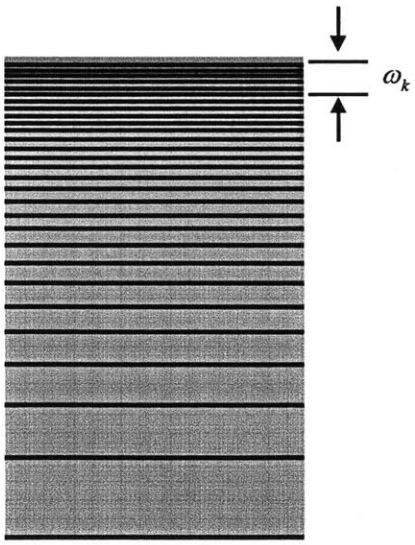

Figure 4-1. Schematic energy diagram of a semiconductor nanocluster. The top electronic state (magenta one) can jump to the states right below it (red upper zone) through a single-phonon process, or jump to the states far below it (orange lower zone) through a multiple-phonon process. The energy criterion to distinguish between the two mechanism is based on the single phonon frequency ω_k.

4.1.2 One-particle states vs. two-particle states

So far, all simulations of electron-phonon interactions are conducted in the framework of a one-particle picture. Thus the nonradiative relaxation of an excited state is always treated as the decay of an electron or a hole, even for an excitonic state. Describing electrons and holes in a one-particle picture is justified, as electrons and holes are essentially one-particle states. However, describing excitons in a one-particle picture implies the independent-particle approximation introduced in Chap. 3.1.1, where excitonic states can be written as $|i,j\rangle$, instead of the linear combination of $|i,j\rangle$. With this approximation, the decay of an excitonic state $|i,j\rangle$ does simplify to the decay of its electron component ($|i,j\rangle \rightarrow |i,j'\rangle$) or its hole component ($|i,j\rangle \rightarrow |i',j\rangle$).

The independent-particle approximation may hold for the first several excitonic states, classified according to their energies, because in most cases they can be approximated by $|i,j\rangle$. However, high-energy excitons shall always be expressed as the linear combination of $|i,j\rangle$. This means the one-particle picture is expected to break down for these excitonic states. Therefore, we suggest treating all exciton-phonon interaction in the framework of two-particle picture. Changing from the one-particle picture to the two particle picture will lead to a significant influence on the phonon-assisted relaxation rates of excitons. As will be shown in this chapter, the two-particle density of state (DOS) can be regarded as the convolution of the electron DOS and the hole DOS. Therefore the excitonic DOS is much larger than electronic DOS, which leads to a significant difference between the relaxation rates of excitons and those of electrons.

4.2 Electron-phonon interaction

4.2.1 Adiabatic approximation

The Hamiltonian of a system composed of electrons and nuclei can be expressed as

$$H = \hat{T}(\mathbf{r}) + \hat{T}(\mathbf{Q}) + U(\mathbf{r},\mathbf{Q}) \tag{4.1}$$

where $\mathbf{r}$ and $\mathbf{Q}$ are the coordinates of electrons and nuclei, respectively, $\hat{T}(\mathbf{r})$ and $\hat{T}(\mathbf{Q})$ the kinetic energy operators of the electrons and nuclei, and $U(\mathbf{r},\mathbf{Q})$ is the total potential energy among all electrons and nuclei.

Within the framework of the Born-Oppenheimer approximation, [75] the wavefunctions of electrons and nuclei are assumed to be independent. Thus the wavefunctions $\Phi_i(\mathbf{r},\mathbf{Q})$ and energies $E_i(\mathbf{Q})$ of electrons can be obtained for each nuclear configuration $\mathbf{Q}$ by solving the electronic Schrödinger equation

$$\left[\hat{T}(\mathbf{r}) + U(\mathbf{r},\mathbf{Q})\right]\Phi_i(\mathbf{r},\mathbf{Q}) = E_i(\mathbf{Q})\Phi_i(\mathbf{r},\mathbf{Q}) \tag{4.2}$$

The wavefunction $\psi(\mathbf{r},\mathbf{Q})$ of the whole system can be expanded with $\Phi_i(\mathbf{r},\mathbf{Q})$ as the basis as

$$\psi(\mathbf{r},\mathbf{Q}) = \sum_i \chi_i(\mathbf{Q})\Phi_i(\mathbf{r},\mathbf{Q}) \tag{4.3}$$

Substituting this wavefunction into the Schrödinger equation of the system

$$H\psi(\mathbf{r},\mathbf{Q}) = \left[\hat{T}(\mathbf{r}) + \hat{T}(\mathbf{Q}) + U(\mathbf{r},\mathbf{Q})\right]\psi(\mathbf{r},\mathbf{Q}) = V\psi(\mathbf{r},\mathbf{Q}) \tag{4.4}$$

and then projecting both sides onto the electronic wavefunction $\Phi_j(\mathbf{q},\mathbf{Q})$, we will obtain a set of coupled equations for $\chi_i(\mathbf{Q})$

$$\sum_i H_{ij}(\mathbf{Q})\chi_i(\mathbf{Q}) = V\chi_j(\mathbf{Q}) \tag{4.5}$$

where V is the energy of the state $\psi(\mathbf{q},\mathbf{Q})$, and $H_{ij}(\mathbf{Q})$ is the Hamiltonian

$$H_{ij}(\mathbf{Q}) = H_{ij}^0(\mathbf{Q}) + H_{ij}^1(\mathbf{Q}) \tag{4.6}$$

where the unperturbed and perturbation Hamiltonian are

$$H_{ij}^0(\mathbf{Q}) = \delta_{ij}\left[E_i(\mathbf{Q}) - \sum_k \frac{\hbar^2}{2M_k}\frac{\partial^2}{\partial Q_k^2}\right] \tag{4.7a}$$

$$H_{ij}^1(\mathbf{Q}) = -\sum_k \frac{\hbar^2}{2M_k}\left(2\left\langle \Phi_j \left| \frac{\partial}{\partial Q_k} \right| \Phi_i \right\rangle \frac{\partial}{\partial Q_k} + \left\langle \Phi_j \left| \frac{\partial^2}{\partial Q_k^2} \right| \Phi_i \right\rangle\right) \tag{4.7b}$$

where M_k are the masses of the normal coordinates Q_k.

Within the framework of the adiabatic approximation, the non-adiabatic coupling term $H_{ij}^1(\mathbf{Q})$ is neglected.[73] Therefore the Hamiltonian matrix becomes diagonal, and Eq. (4.5) is simplified to

$$\left(E_i(\mathbf{Q}) - \sum_k \frac{\hbar^2}{2M_k}\frac{\partial^2}{\partial Q_k^2}\right)\chi_i(\mathbf{Q}) = V\chi_i(\mathbf{Q}) \tag{4.8}$$

which implies the nuclei move on the adiabatic potential energy surface (PES) $E_i(\mathbf{Q})$. The nuclear wavefunctions $\chi_i(\mathbf{Q})$ can be obtained by solving Eq. (4.6).

Within the harmonic approximation, all anharmonic effects are neglected. Thus $E_i(\mathbf{Q})$ can be expressed as the linear combination of linear and quadratic terms,

$$E_i(\mathbf{Q}) = \sum_k \alpha_k^i Q_k + \sum_k \beta_k^i Q_k^2 + \sum_{k,l} \gamma_{k,l}^i Q_k Q_l \tag{4.9}$$

where α_k^i, β_k^i, $\gamma_{k,l}^i$ are coefficients. By choosing the equilibrium position as the origin $\mathbf{Q}_0$, α_k^i can be eliminated. For normal coordinates Q_k, bilinear terms vanish and $\gamma_{k,l}^i = 0$. Therefore Eq. (4.8) yields k independent one-dimensional harmonic-oscillator equations, which have analytical solutions $\theta_{i,v_k}(Q_k)$ in which v_k are the quantum numbers. Then the nuclear wavefunction $\chi_{i,v}(\mathbf{Q})$ is expressed as

$$\chi_{i,v}(\mathbf{Q}) = \prod_k \theta_{i,v_k}(Q_k) \tag{4.10}$$

where $v = (v_1, v_2, \ldots, v_k)$.

4.2.2 Perturbation theory

Within the framework of the perturbation approximation, the nonradiative transition rate $\gamma_{i\to j}$ between any two adiabatic states $\chi_{i,v'}(\mathbf{Q})\Phi_i(\mathbf{r},\mathbf{Q})$ and $\chi_{j,v''}(\mathbf{Q})\Phi_j(\mathbf{r},\mathbf{Q})$ with energies $V_{i,v'}$ and $V_{j,v''}$ can be calculated with the Fermi golden rule by taking $H_{ij}^1(\mathbf{Q})$ as the perturbation Hamiltonian,[76,77]

$$\gamma_{i\to j} = 2\pi \sum_{v',v''} P_{v'} \left| \left\langle \chi_{j,v''} \middle| H_{ij}^1 \middle| \chi_{i,v'} \right\rangle \right|^2 \delta\left(V_{j,v''} - V_{i,v'}\right) \tag{4.11}$$

where the summation is over all initial vibronic states v' weighted by the Boltzmann factor $P_{v'}$, and all final vibrational states v''. The perturbation term is

$$\left\langle \chi_{j,v''} \middle| H_{ij}^1 \middle| \chi_{i,v'} \right\rangle = -\sum_k \frac{\hbar^2}{M_k} \left\langle \Phi_j \chi_{j,v''} \middle| \frac{\partial \Phi_i}{\partial Q_k} \frac{\partial \chi_{i,v'}}{\partial Q_k} \right\rangle - \sum_k \frac{\hbar^2}{2M_k} \left\langle \Phi_j \chi_{j,v''} \middle| \chi_{i,v'} \frac{\partial \Phi_i^2}{\partial^2 Q_k} \right\rangle \tag{4.12}$$

The second term in Eq. (4.12) are usually neglected with the assumption that the electronic wavefunctions are slowly varying functions of the normal coordinates Q_k,

and Eq (4.12) becomes[78,79]

$$\left\langle \chi_{j,v'} \left| H_{ij}^{1} \right| \chi_{i,v} \right\rangle = -\sum_{k} \frac{\hbar^2}{M_k} \left\langle \Phi_j \left| \frac{\partial \Phi_i}{\partial Q_k} \right\rangle \right\langle \chi_{j,v'} \left| \frac{\partial \chi_{i,v}}{\partial Q_k} \right\rangle \tag{4.13}$$

4.2.3 Single-phonon relaxation rates

The lineshape function is the crucial issue to evaluate $\gamma_{i\to j}$ numerically, which is essentially determined by the underlying decay mechanisms. As shown in Fig. 4-1, a high-energy exciton can decay through both single-phonon and multiple-phonon processes. Both should be considered. Here we propose an energy criterion to distinguish between the two processes, $\Delta E_{ij} < \hbar\omega_k$ for single-phonon relaxation, and $\Delta E_{ij} > \hbar\omega_k$ for multiple-phonon relaxation.

For a single-phonon process, the decay only occurs between two electronic states with an energy difference smaller than that of the *k*th phonon, $\hbar\omega_k$. In this case a Lorentzian lineshape is applied and Eq. (4.11) is simplified to

$$\gamma_{i\to j}^{SP} = \sum_{k} \frac{\hbar^2}{M_k} \left| C_k^{ij} \right|^2 \hbar\omega_k \left[\frac{(n_k+1)\gamma_i^{SP}}{\left(\Delta E_{ij} - \hbar\omega_k\right)^2 + \left(\gamma_i^{SP}\right)^2} + \frac{n_k \gamma_i^{SP}}{\left(\Delta E_{ij} + \hbar\omega_k\right)^2 + \left(\gamma_i^{SP}\right)^2} \right] \tag{4.14}$$

where $C_k^{i,j} = \left\langle \varphi_j \left| \partial / \partial Q_k \right| \varphi_i \right\rangle$, $\Delta E_{ij} = E_i - E_j$, and γ_i^{SP} is the width of the Lorentzian function corresponding to the *i*th electron, which is exactly the single-phonon decay rate to be determined. Here n_k is the average quantum number of the *k*th vibrational mode at the thermal equilibrium. $\gamma_{i\to j}^{SP}$ can be found as the imaginary part of the following self-energy term

$$\Sigma_{i\to j}^{sp} = \sum_{k} \frac{\hbar^2}{M_k} \left| C_k^{ij} \right|^2 \hbar\omega_k \left[\frac{n_k + 1}{\Delta E_{ij} - \hbar\omega_k - i\gamma_i^{SP}} + \frac{n_k}{\Delta E_{ij} + \hbar\omega_k - i\gamma_i^{SP}} \right] \tag{4.15}$$

This term is close to the self-energy term in Ref. 71, with a difference in coefficients arising from different perturbation mechanisms. Note that $\Sigma^{SP}_{i\to j}$ corresponds to a Feynman diagram similar to Σ_{xc} in the *GW* case. Thus $\gamma_i^{SP} = \sum_{j,|E_j|<|E_i|} \gamma^{SP}_{i\to j}$ can be evaluated numerically in the same manner as that for the QP inelastic scattering rates in the *GWΓ* implementation.

4.2.3 Multiple-phonon relaxation rates

The multiple-phonon decay process is more complicated and can only be treated properly by including anharmonic effects. Since a small cluster can be regarded as a poly-atomic molecule, the dominant anharmonic effect is attributed to the displacement of the potential energy surface for different electronic states.[80] Within the displaced potential surface approximation, the normal coordinates Q_k and their masses M_k and frequencies ω_k are assumed to be constant for all electronic and excitonic states. Only the equilibrium positions Q_k^0 change for different states, namely $Q_k^{0,i} \neq Q_k^{0,j}$. We can define the dimensionless displacements Δ_k^{ij} as

$$\Delta_k^{ij} = \left(\frac{M_k\omega_k}{\hbar}\right)^{\frac{1}{2}}\left(Q_k^{0,i} - Q_k^{0,j}\right) \tag{4.16}$$

which measures the displacement along the *k*th normal mode when the electron changes from state *i* to state *j*.

Following Freed and Jortner,[74] the transition rate between two states through the multiple-phonon process is

$$\gamma_{i\to j}^{MP}=\sum_k \frac{\hbar^2}{M_k}\left|C_k^{ij}\right|^2 \hbar\omega_k \pi \frac{1}{\hbar D_{ij}^k \sqrt{2\pi}} \left(\begin{array}{l} (n_k+1)\exp\left(-\dfrac{\left(\Delta E_{ij}-\hbar\omega_k-E_M^{ij}\right)^2}{2\hbar^2\left(D_{ij}^k\right)^2}\right) \\ +n_k \exp\left(-\dfrac{\left(\Delta E_{ij}+\hbar\omega_k-E_M^{ij}\right)^2}{2\hbar^2\left(D_{ij}^k\right)^2}\right) \end{array} \right) \tag{4.17}$$

with

$$\left(D_{ij}^k\right)^2=\frac{1}{2}\sum_k \omega_k^2\left(\Delta_k^{ij}\right)^2\left(2n_k+1\right)$$

$$n_k=\frac{1}{\exp\left(\hbar\omega_k/k_BT\right)-1}$$

$$E_M^{ij}=\frac{1}{2}\sum_k \hbar\omega_k\left(\Delta_k^{ij}\right)^2$$

Here the rearrangement energy E_M^{ij} will be neglected without significant influence on computational results. Unlike $\gamma_{i\to j}^{SP}$ with a Lorentzian lineshape, $\gamma_{i\to j}^{MP}$ exhibits multiple Gaussian lineshapes, with spectral widths D_{ij}^k temperature-dependent. Note that both $\gamma_{i\to j}^{SP}$ and $\gamma_{i\to j}^{MP}$ share the same form as the peak intensities go to infinity and the linewidths become δ-functions.

$$\gamma_{i\to j}=\sum_k \frac{\hbar^2}{M_k}\left|C_k^{ij}\right|^2 \hbar\omega_k \pi\left[\left(n_k+1\right)\delta\left(E_i-E_j-\omega_k\right)+n_k\delta\left(E_i-E_j+\omega_k\right)\right] \tag{4.18}$$

It is the decay mechanism that determines how the delta functions are broadened.

The total relaxation rates of an electronic state through electron-phonon interaction are expressed as the sum of all decay rates between this state and states with lower energies

$$\gamma_i^{E-P} = \sum_{j,|E^{0,j}|<|E^{0,i}|} \left(\gamma_{i\to j}^{SP} + \gamma_{i\to j}^{MP}\right) \tag{4.19}$$

4.3 Numerical details

A small silicon cluster, Si_{20}, has been used in the previous chapter (Chap. 3) to demonstrate our methods developed for the electronic and excitonic inelastic relaxation rates. With the simplification strategy proposed in Chap. 3, now we can handle relatively large clusters. In this chapter, a larger silicon cluster, Si_{46} will be simulated as an example to show the approaches developed in this chapter for the calculation of the nonradiative relaxation rates of electrons and excitons in nanoclusters. There are two reasons to switch from Si_{20} to Si_{46}. Firstly, we need a large nanocluster to narrow the distribution of the data points, which will facilitate the discussion. Secondly, Si_{20} has degenerate states because of its C_{3v} symmetry. Thus the calculation of the electron-phonon interaction shall take into account the Jahn-Teller effect explicitly, which complicates the study dramatically. On the other hand, Si_{46} does not have any degenerate state because of its C_{2v} symmetry. Thus we can focus on the nonradiative relaxation rates for Si_{46}.

The ground state LDA calculation is performed using the SIESTA code.[35] The core electrons [$1s^2 2s^2 2p^6$] of Si are replaced by the nonlocal norm-conserving pseudopotential based on the Troullier-Martins scheme.[36] A quintuple-ζ double-polarization (5Z2P) basis set of numerical atomic orbitals is used for the four valence electrons of Si. The optimized structure of Si_{46} is illustrated in Fig. 4-2, which has the C_{2v} symmetry.

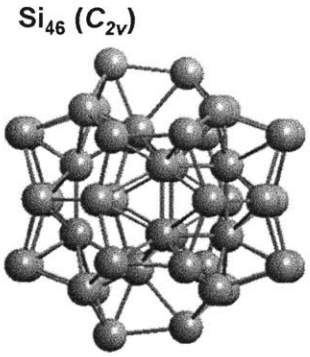

Figure 4-2. Optimized structure of Si_{46} with the C_{2v} symmetry.

All integrals are evaluated on a uniform grid in real space with a grid spacing of 0.5 a.u. The exchange integrals $\int d\mathbf{r}\int d\mathbf{r}'\varphi_i(\mathbf{r})\varphi_j(\mathbf{r})V(\mathbf{r},\mathbf{r}')\varphi_k(\mathbf{r}')\varphi_l(\mathbf{r}')$ are evaluated by first solving Poisson equations with the multigrid method.[37] The convergence of the QP calculation usually requires a large number of unoccupied states for the evaluation of the polarizability. Thus a Coulomb-hole screened-exchange (COHSEX) remainder scheme[33] has been applied to accelerate the convergence of the correlation part $\langle\varphi_i|\Sigma_c|\varphi_i\rangle$.

The properties of the one-particle states are obtained by solving the quasiparticle equation introduced in Chap. 2

$$\left(\hat{T}+V_{ext}+V_H\right)\varphi_i(\mathbf{r})+\int d\mathbf{r}'\Sigma_{xc}(\mathbf{r},\mathbf{r}';E_i)\varphi_i(\mathbf{r}')=E_i\varphi_i(\mathbf{r}) \tag{4.20}$$

After applying analytical continuation of $\Sigma_c(\mathbf{r},\mathbf{r}';E)$ in the complex energy plane, the energy E_i and the inelastic scattering rates γ_i of an electronic state are obtained by solving a complex equation set numerically

$$\mathrm{Re}\left\langle\varphi_i\left|\Sigma_{xc}(E_i-i\eta_i\gamma_i)\right|\varphi_i\right\rangle-\langle\varphi_i|V_{xc}|\varphi_i\rangle=E_i-\varepsilon_i \tag{4.21a}$$

$$\left|\mathrm{Im}\left\langle\varphi_i\left|\Sigma_{xc}(E_i-i\eta_i\gamma_i)\right|\varphi_i\right\rangle\right|=\gamma_i \tag{4.21b}$$

The inelastic scattering rates of excitons are calculated with the approximation method developed in Chap. 3 (Eq. 3.19)

$$\Gamma_s = \sum_{v,c} \left| R_s^{vc} \right|^2 (\gamma_c + \gamma_v) \tag{4.22}$$

in which R_s^{vc} are the coefficients of the linear combination of the sth exciton obtained by TDLDA, namely

$$\rho_s(\mathbf{r}) = \sum_{v,c} R_s^{vc} \varphi_v^*(\mathbf{r}) \varphi_c(\mathbf{r}) \tag{4.23}$$

The normal coordinates Q_k and frequencies ω_k are obtained by diagonalizing the mass-weighed second-order force matrix (Hessian matrix).[81] The second order derivatives $\partial^2 U / \partial X_i \partial X_j$ are calculated with a finite difference approach. Here U is the total potential energy among all electrons and nuclei. X_i are nuclear Cartesian coordinates. A unitary matrix without translational and rotational vectors is used to transform the Hessian matrix to a block diagonal matrix with each block corresponding to an irreducible representation.[81] Block off-diagonal elements are small and are thus eliminated to ensure that each Q_k belongs to a specific irreducible representation exclusively.

The force on the ith atom due to the jth electronic state is calculated as $\mathbf{f}_i^j$ by our modified version of the SIESTA code. The calculation sums up all the energy derivatives associated with the jth electronic state, namely those from the kinetic energy, the non-local pseudopotential energy, Hartree energy, exchange-correlation energy and basis overlap.[35] Then the shift of the ith atom due to the jth electronic state is estimated as $\Delta X_{i,n}^j \approx \dfrac{f_{i,n}^j}{\partial^2 U / \left(\partial X_{i,n}^j\right)^2}$, $n = 1,2,3$

Therefore the shift along the kth normal coordinate due to the jth electronic state

ΔQ_k^j can be obtained by the inner product between $\Delta \mathbf{X}^j$ and $\mathbf{Q}_k$, where $\mathbf{Q}_k$ is the vector representation of Q_k in Cartesian coordinates. Here we do not take into account the Jahn-Teller effect, since the silicon cluster investigated here does not have degenerate electronic states. The pseudo-Jahn-Teller effect is not included either. Therefore we only need to calculate those ΔQ_k belonging to the irreducible representation with the total symmetry, namely A_1 of the C_{2v} point group, since the square of each irreducible representation of the C_{2v} point group is A_1.

The derivative $\left|\langle \varphi_j | \partial / \partial Q_k | \varphi_i \rangle\right|$ is evaluated by a finite difference method, which is more accurate than the frequently used perturbation method in literature. In the SIESTA code, the molecular orbitals are expressed as the linear combination of atomic orbital (LCAO),

$$\varphi_i(\mathbf{r}) = \sum_m c_{i,m} \phi_m(\mathbf{r}) \tag{4.24}$$

where $\phi_m(\mathbf{r})$ is the mth atomic orbital. Then we have

$$\frac{\partial \varphi_i(\mathbf{r})}{\partial X} = \sum_m \frac{\partial c_{i,m}}{\partial X} \phi_m(\mathbf{r}) + \sum_m c_{i,m} \frac{\partial \phi_m(\mathbf{r})}{\partial X} \tag{4.25}$$

and

$$\langle \varphi_j | \partial / \partial X_k | \varphi_i \rangle = \sum_{m,n} c_{j,n} \frac{\partial c_{i,m}}{\partial X_k} \int \phi_n(\mathbf{r}) \phi_m(\mathbf{r}) d\mathbf{r} + \sum_{m,n} c_{j,n} c_{i,m} \int \phi_n(\mathbf{r}) \frac{\partial \phi_m(\mathbf{r})}{\partial X_k} d\mathbf{r} \tag{4.26}$$

Here we only take into account the internal conversion and neglect the intersystem crossing between singlet and triplet states arising from the spin-orbit coupling. The derivation and numerical treatment for excitonic states are similar to those of electronic states. First the force on the ith atom due to the jth excitonic state is calculated as

$$\mathbf{F}_i^j = \sum_{v,c} \left| R_{vc}^j \right|^2 \left(\mathbf{f}_i^c - \mathbf{f}_i^v \right) \tag{4.27}$$

from which $\Delta X_{i,n}^j$, ΔQ_k^j, $\Delta_k^{i,j}$ and $E_M^{i,j}$ can be obtained in exactly the same manner as in the case of electrons. The coupling term between the two excitonic states is approximated as

$$\left\langle \rho_j \left| \partial / \partial Q_k \right| \rho_i \right\rangle = \sum_{v,c} \sum_{v',c'} R_{vc}^i R_{v'c'}^j \left(\delta_{vv'} \left\langle \varphi_c \left| \partial / \partial Q_k \right| \varphi_{c'} \right\rangle + \delta_{cc'} \left\langle \varphi_v \left| \partial / \partial Q_k \right| \varphi_{v'} \right\rangle \right). \tag{4.28}$$

Then Eqs. (4.14) and (4.17) can be extended to the calculation of excitonic nonradiative transition rates.

4.4 Results and discussions

4.4.1 Electronic relaxation dynamics in Si clusters

The inelastic scattering rates γ^{IS} of electrons and holes in the cluster Si_{46} calculated by the *GWΓ* method are plotted versus the excitation energy $\left| E_i - E_F \right|$ in log-log style in Fig. 4-3. Note that all relaxation rates are given in units of eV, which can be easily converted to fs^{-1} by being divided by $\hbar = 0.658$ eV·fs. Our calculations show that the inelastic scattering rates of electrons and holes in Si_{46} are similar to Si_{20} which was presented in Chap. 3. Specifically, the electrons and holes in Si_{46} approach the quadratic law of Quinn and Ferell in the high-energy regime ($\left| E_i - E_F \right|$>6 eV)

$$\tau_i^{IS} = 263 r_s^{-5/2} \left(E_i - E_F \right)^{-2} \text{eV}^2 \text{ fs}. \tag{4.29}$$

where $\tau_i^{IS} = \left(2\gamma_i^{IS} \right)^{-1}$ is the inelastic scattering lifetime.

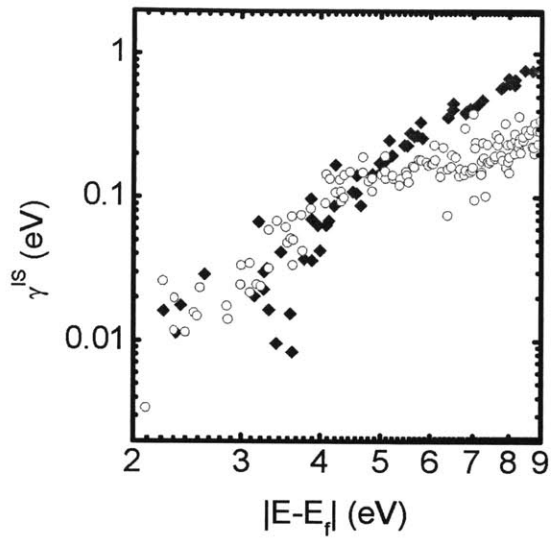

Figure 4-3. Log-log plot of inelastic scattering rates γ^{IS} of electrons (hollow circles) and holes (solid diamonds) in Si_{46} vs. energy from the Fermi level.

The single-phonon nonradiative relaxation rates γ^{SP} of electrons and holes in Si_{46} versus the excitation energy $|E_i - E_F|$ obtained at 0 K by Eq. (4.14) are plotted in Fig. 4-4a. Note that some data points in Fig. 4-3 do not have corresponding points in Fig. 4-4a, since γ^{SP} for those states vanishes. This arises from the fact that the energy gaps between two neighboring states in a confined system may be larger than the maximum phonon frequency and thus the single-phonon relaxation mechanism between such two states is strictly prohibited. The multiple-phonon nonradiative relaxation rates γ^{MP} at 0K in Si_{46} are presented in Fig. 4-4b. The pattern of γ^{MP} is quite dispersive. For some electron (or hole) states, the relaxation rates of the multiple-phonon process are even comparable to those of the single-phonon process. More importantly all electronic states (except the HOMO and LUMO) can decay through the multiple-phonon relaxation process, which is an alternative nonradiative decay pathway when the single-phonon process is absent. Therefore the multiple-phonon decay pathway is an important relaxation mechanism and should always be included for the study of nonradiative rates for finite systems.

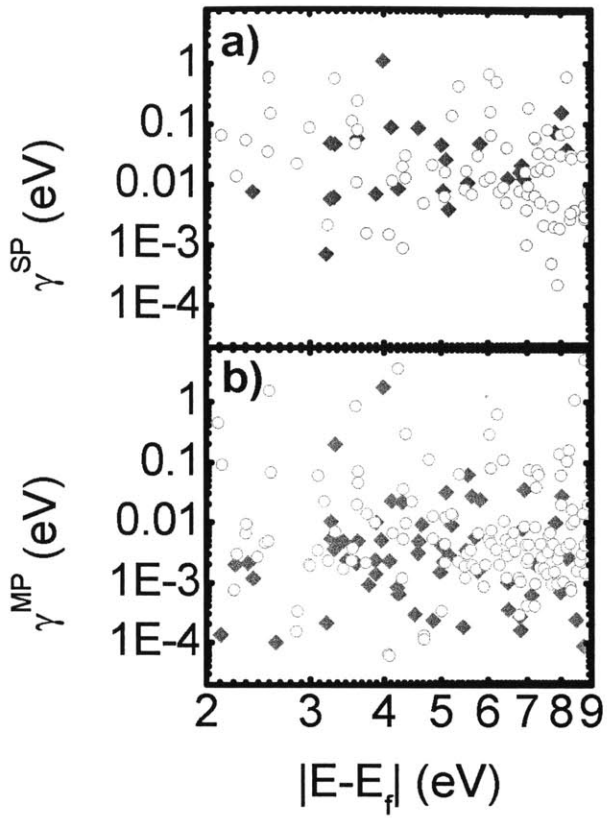

Figure 4-4. Log-log plots of a) Single-phonon nonradiative relaxation rates γ^{SP} and b) multiple-phonon nonradiative relaxation rates γ^{MP} of electrons (hollow circles) and holes (solid diamonds) in Si_{46} at 0 K.

The patterns of γ^{SP} and γ^{MP} in Figs. 4-4a and 4-4b are more dispersive than that of γ^{IS} in Fig. 4-3. The reason is that the single-phonon relaxation can only happen between a state and those states with energies below it yet not too far away (within the phonon energy $\hbar\omega_k$). Therefore an electron in a given electronic state may have many strongly coupled states available for the single-phonon relaxation and thus exhibit a large γ^{SP}. On the hand, it may only have one or two weakly coupled states and thus present a small γ^{SP}. It means that γ^{SP} is essentially a local quantity in terms of energy and is dependent upon the case being studied. This explains why the

pattern of γ^{SP} is so dispersive and even two states with close excitation energies $|E_i - E_F|$ may have quite different γ^{SP}. Note that although the multiple-phonon relaxation can happen in principle between a state and any states with energies far below it, in practice there is still an upper limit for the energy gaps, as γ^{MP} decreases exponentially with increasing energy gap. It means that γ^{SP} is a semi-local quantity in terms of energy and is also dependent upon the case being studied. Therefore the same interpretation applies to γ^{MP}. The local single-phonon relaxation and semi-local multiple-phonon relaxation processes distinguish notably from the inelastic scattering relaxation, where an electron in an electronic state can transit to those states with energies far below the initial state, namely no upper limit for energy gaps. Therefore, the higher the energy of the initial state, the larger the inelastic scattering rate is. In this case, the absolute excitation energy $|E_i - E_F|$ does matter.

The ratios $\gamma^{IS}/\gamma^{SP+MP}$ ($\gamma^{SP+MP} = \gamma^{SP} + \gamma^{MP}$) are plotted in Fig. 4-5 for the comparison of the inelastic scattering rates and the nonradiative relaxation rates of electronic states in Si_{46}. The patterns for $\gamma^{IS}/\gamma^{SP+MP}$ are even more dispersive than that of γ^{MP}, with some data points above unity and the others below. This implies that inelastic scattering is highly possible to happen for some electronic states, while nonradiative relaxation will dominate the others. However, the data in Fig. 4-5 suggest that the inelastic scattering relaxation is a more significant effect, since the logarithmic mean of data in Fig. 4-5 are larger than unity. In addition, nonradiative relaxation progresses in a cascade style. Thus an electronic state with a high excitation energy may pass through several intermediate electronic states during its nonradiative relaxation. The inelastic scattering decay will happen sooner or later, as long as one of these intermediate states favors inelastic scattering more. Therefore it is reasonable to assume that inelastic scattering can always occur for electronic states with high excitation energy.

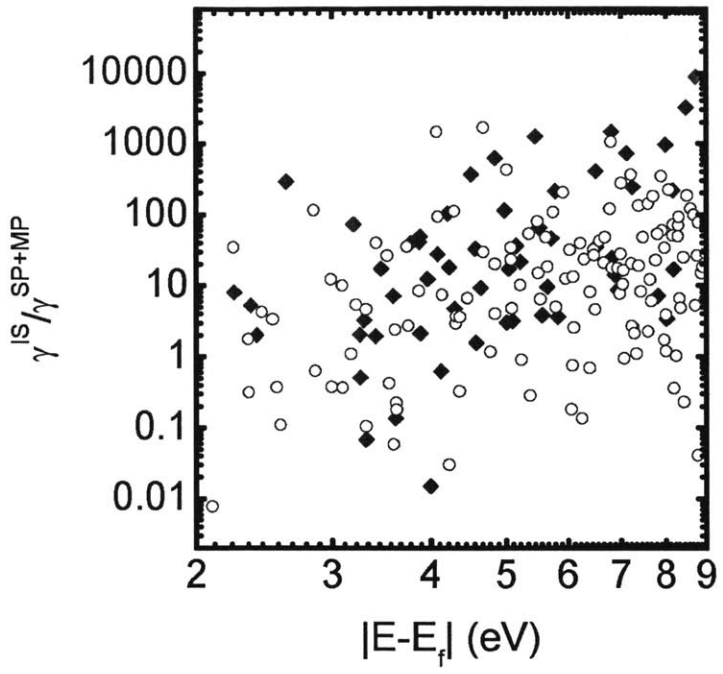

Figure 4-5. Log-log plot of the ratios $\gamma^{IS}/\gamma^{SP+MP}$ for electrons (hollow circles) and holes (solid diamonds) in Si_{46} at 0 K, where $\gamma^{SP+MP} = \gamma^{SP} + \gamma^{MP}$.

The temperature effect is studied by recalculating γ^{SP}, γ^{MP} and $\gamma^{IS}/\gamma^{SP+MP}$ at 300 K. The results are illustrated in Figs. 4-6 and 4-7. Here we assume that the electronic scattering rates are temperature-independent. As the temperature changes from 0 to 300 K, all γ^{SP} and γ^{MP} are enhanced with a factor ranging from 1 to 3. Usually the temperature enhancement of γ^{MP} is larger than the corresponding enhancement of γ^{SP}, since the increased temperature not only elevates the average quantum number n_k of each normal mode for both γ^{SP} and γ^{MP}, but also increases the thermal broadening factor D_{ij}^k in Eq. (4.17) solely for γ^{MP}. Results in Fig. 4-7 show that the ratios of $\gamma^{IS}/\gamma^{SP+MP}$ are reduced at 300K compared to the ratios of $\gamma^{IS}/\gamma^{SP+MP}$ at 0K as shown in Fig. 4-5. Yet it is still essential to include the multiple-phonon mechanism for calculations of $\gamma^{IS}/\gamma^{SP+MP}$, γ^{IS} and γ^{SP+MP}.

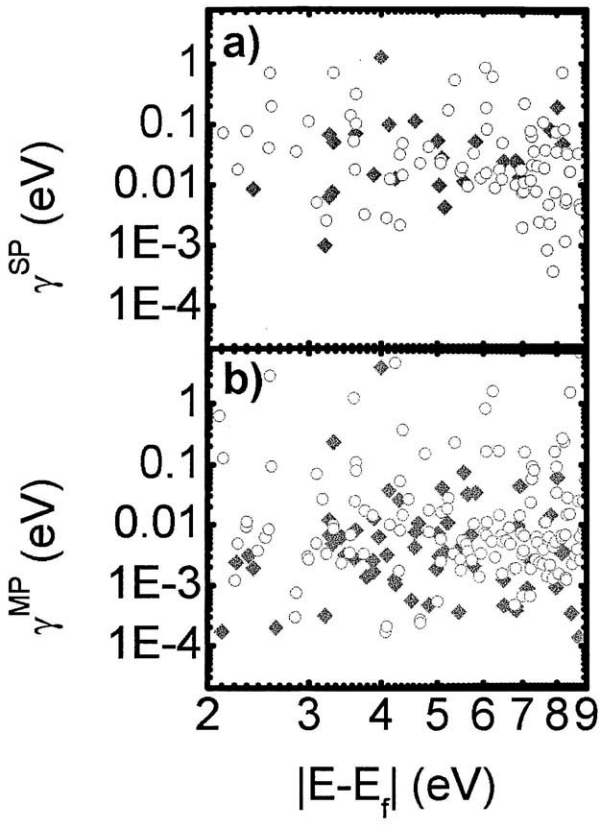

Figure 4-6. Log-log plots of a) Single-phonon nonradiative relaxation rates γ^{SP} and b) multiple-phonon nonradiative relaxation rates γ^{MP} of electrons (hollow circles) and holes (solid diamonds) in Si_{46} at 300 K.

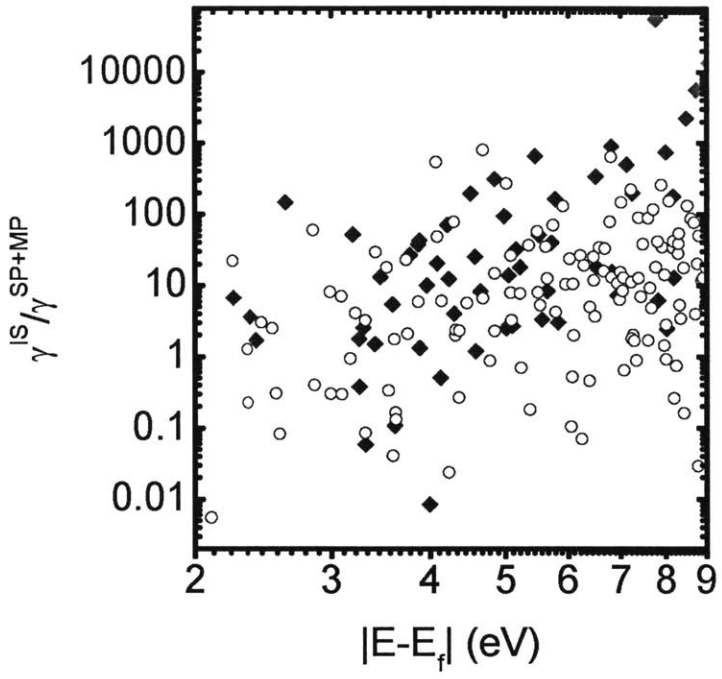

Figure 4-7. Log-log plot of the ratios $\gamma^{IS}/\gamma^{SP+MP}$ for electrons (hollow circles) and holes (solid diamonds) in Si_{46} at 300 K, where $\gamma^{SP+MP} = \gamma^{SP} + \gamma^{MP}$.

We have introduced in Chap. 1 that there are different possible ways to excite a multi-electron system. One possible way is to add an electron to the system, or remove an electron from it to excite a hole. These excitations exactly correspond to the electronic states discussed here. It should be pointed out that these electronic states are essentially charge-non-conserved one-particle excitations, which are not directly involved in most optical applications of semiconductor nanoclusters. Actually in photovoltaic systems based on semiconductor nanoclusters, most incident photons just induce charge-conserved excitonic (electron-hole) excitations. Therefore the relaxation dynamics of excitons is of greater importance, which will be addressed in the next section.

4.4.2 Excitonic relaxation dynamics in Si clusters

The inelastic scattering rates Γ^{IS} (capital letter stands for excitons) of excitons in

Si_{46} calculated by the approximation method of Eq. (4.22) are plotted versus the excitation energy Ω in log-log style in Fig. 4-8, where the solid line is the curve fitting of Γ^{IS} by a simple rational function (Padé function P_1^2)

$$y^{IS} = 2x + a + \frac{b}{x+c} \tag{4.30}$$

where x and y represent $\ln(\Omega/\text{eV})$ and $\ln(\Gamma^{IS}/\text{eV})$, respectively. The fitting coefficients a, b and c are -5.00, -0.22 and -0.40, respectively. The factor of the linear term in x is fixed to be 2, since it is easy to prove that the quadratic relation between the excitonic decay rate and the excitonic energy will be approached at the high-energy limit (large x), provided that the quadratic relation between the QP decay rate and the QP energy is approached at the high energy regime.

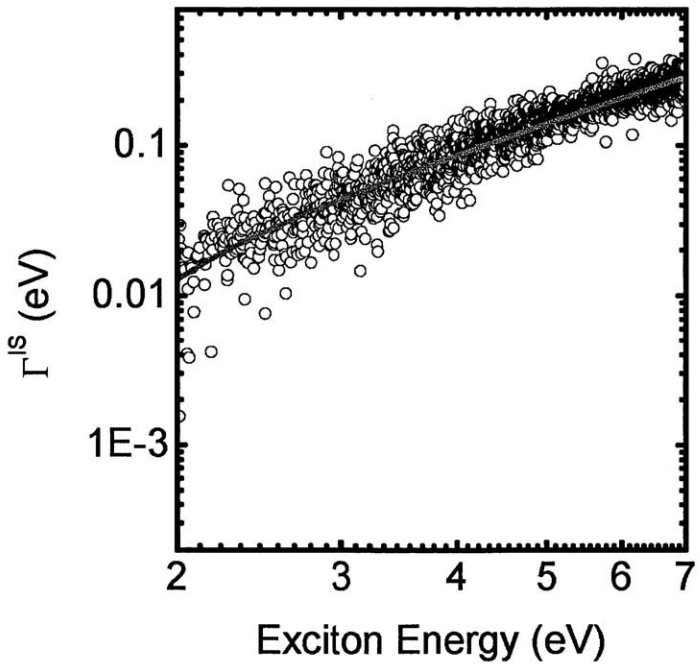

Figure 4-8 Log-log plot of the inelastic scattering rates Γ^{IS} of excitons in Si_{46} vs. exciton energy. The solid line is the curve-fitting.

The single-phonon nonradiative relaxation rates Γ^{SP} of excitons in Si_{46} at 0 K obtained by Eq. (4.14) are plotted versus the excitation energy Ω_s in Fig. 4-9a,

where the Γ^{SP} points are found to be energy-dependent in the low-energy regime. Unlike Γ^{IS} shown in Fig. 4-8, such an energy-dependence diminishes in the high-energy regime and the pattern of Γ^{SP} becomes flat, although the data distribution is still wide. This is attributed to the large excitonic density of state (DOS) in the high-energy regime that quickly saturates the exciton-phonon interaction. The effect of the excitonic DOS will be discussed with more details in the next section. According to the pattern shown in Fig. 4-8a, we fit the data with an exponential function

$$y^{SP} = y_0^{SP} + A^{SP} e^{-\left(\Omega-\Omega_0^{SP}\right)/t^{SP}} \tag{4.31a}$$

where y^{SP} represents $\log\left(\Gamma^{SP}/\text{eV}\right)$, Ω is the excitonic energy, and y_0^{SP}, A^{SP}, Ω_0^{SP} and t^{SP} are fitting parameters. The fitting curve is plotted in Fig. 4-8a as a solid line. Here $y_0^{SP} = -0.826$, which leads to the converged Γ^{SP} that is estimated to be 0.149 eV.

The multiple-phonon nonradiative relaxation rates Γ^{MP} of excitons in Si_{46} at 0 K obtained by Eq. (4.17) are presented in Fig. 4-9b. It can be seen that the pattern of Γ^{MP} is similar to that of Γ^{SP} as shown in Fig. 4-9a. Thus the data are fitted with the same equation

$$y^{MP} = y_0^{MP} + A^{MP} e^{-\left(\Omega-\Omega_0^{MP}\right)/t^{MP}} \tag{4.31b}$$

Here $y_0^{MP} = -0.767$, which yields the converged Γ^{MP} to be 0.170 eV. Note that Γ^{MP} are always comparable to Γ^{SP} in the full energy range studied. This again demonstrates the necessity to include the multiple-phonon decay mechanism for the simulation of nonradiative relaxation rates. Furthermore, both Γ^{SP} and Γ^{MP} in the two clusters range from 0.1 to 1000 meV, which correspond to nonradiative relaxation lifetimes ranging from several picoseconds to about a femtosecond. Such a fast nonradiative relaxation process implies that the phonon bottleneck does not apply in

the present structure Si_{46}. Some previous research has also predicted similar results in other semiconductor nanoclusters.[82]

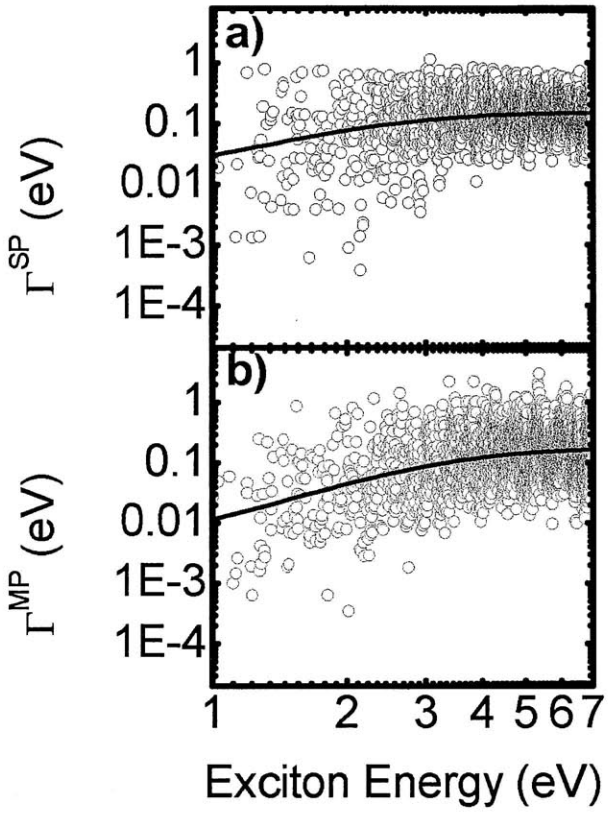

Figure 4-9. a) Single-phonon nonradiative relaxation rates Γ^{SP} and b) multiple-phonon nonradiative relaxation rates Γ^{MP} of excitons in Si_{46} at 0 K. Solid lines are curve fitting based on Eq. (4.31).

The ratios $\Gamma^{IS}/\Gamma^{SP+MP}$ ($\Gamma^{SP+MP}=\Gamma^{SP}+\Gamma^{MP}$) are plotted in Fig. 4-10 for the comparison of the inelastic scattering rates and the nonradiative relaxation rates of excitonic states in Si_{46}. The ratio $\Gamma^{IS}/\Gamma^{SP+MP}$ in Fig. 4-10 increases steadily with increasing excitonic energy. It is consistent with the fact that Γ^{IS} increases almost quadratically with increasing excitonic energy (Fig. 4-8), while Γ^{SP} and Γ^{MP} approach a constant in the high-energy regime (Fig. 4-9). It should be emphasized here that most ratios $\Gamma^{IS}/\Gamma^{SP+MP}$ for excitons are smaller than unity, which notably differs from $\gamma^{IS}/\gamma^{SP+MP}$ for electronic states (Fig. 4-5). This again can be attributed

to large excitonic DOS and will be addressed in the next section.

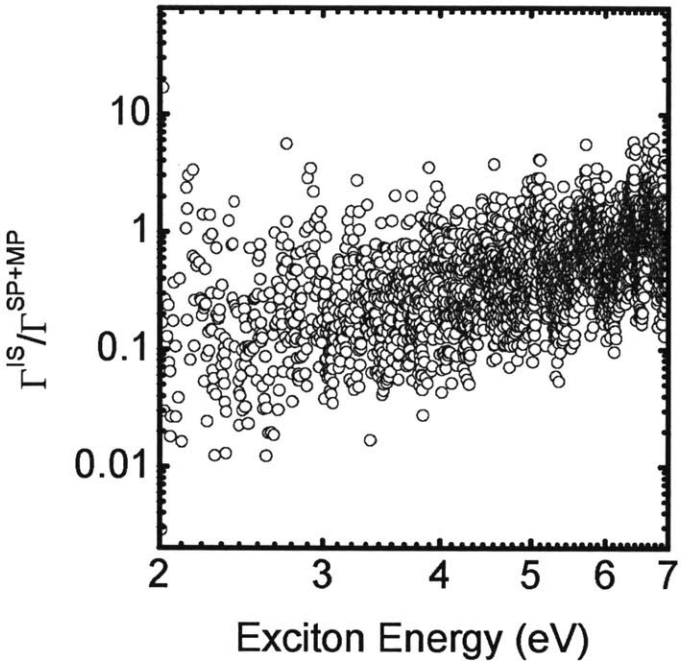

Figure 4-10. The ratios $\Gamma^{IS}/\Gamma^{SP+MP}$ for excitons in Si_{46} at 0 K, where $\Gamma^{SP+MP} = \Gamma^{SP} + \Gamma^{MP}$.

The temperature effect is investigated by recalculating Γ^{SP}, Γ^{MP} and $\Gamma^{IS}/\Gamma^{SP+MP}$ at various temperatures. The influence of the temperature on the nonradiative relaxation of excitons can be tracked as the average ratios $\overline{\Gamma_T^{SP}/\Gamma_{T=0}^{SP}}$ and $\overline{\Gamma_T^{MP}/\Gamma_{T=0}^{MP}}$, which are plotted versus temperature in Fig. 4-11. Assume that all phonon frequencies can be represented by a characteristic phonon frequency $\bar{\omega}^{SP}$ for the single-phonon relaxation process. According to Eq. (4.14), we can get

$$\overline{\Gamma_T^{SP}/\Gamma_{T=0}^{SP}} \approx \left(2\bar{n}^{SP}+1\right)^{1/2} \approx \left(\frac{2k_BT}{\hbar\bar{\omega}^{SP}}\right)^{1/2} + C^{SP} \tag{4.32a}$$

where $\bar{n}^{SP}$ is the average quantum number of the characteristic phonon frequency $\bar{\omega}^{SP}$. The last approximate equality in Eq. (4.32a) is valid only in the high

temperature limit. C^{SP} is a fitting constant and it vanishes only in the ideal case. A similar equation can be written to define the characteristic phonon frequency $\bar{\omega}^{MP}$ for the multiple-phonon relaxation process.

$$\overline{\Gamma_T^{MP}/\Gamma_{T=0}^{MP}} \approx \left(2\bar{n}^{MP}+1\right)^{1/2} \approx \left(\frac{2k_BT}{\hbar\bar{\omega}^{MP}}\right)^{1/2} + C^{MP} \tag{4.32b}$$

The two data sets in Fig. 4-11 are fitted based on Eqs. (4.32a) and (4.32b). According to the coefficients of $T^{1/2}$, the two characteristic phonon frequencies $\bar{\omega}^{SP}$ and $\bar{\omega}^{MP}$ for single-phonon and multiple-phonon relaxation processes are obtained as 319 and 95 cm^{-1}. Numerically, $\bar{\omega}^{SP}$ and $\bar{\omega}^{MP}$ are just the inverse of the weighed average of the inverse phonon frequencies, and thus have some important physical information over the selected temperature range for the cluster investigated.

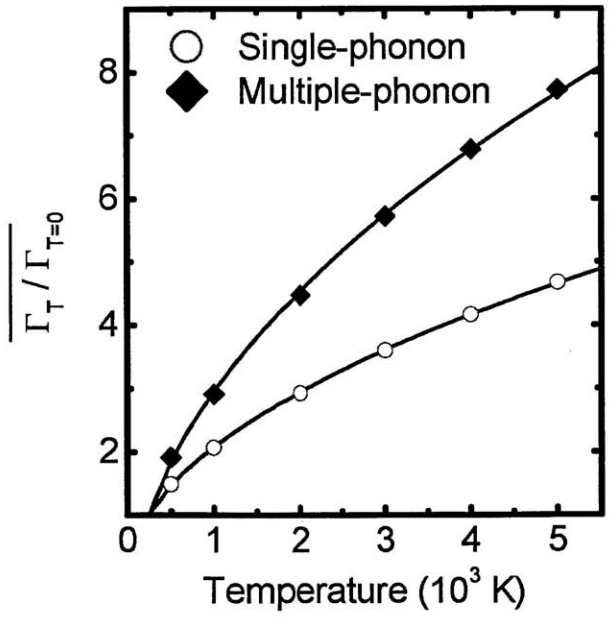

Figure 4-11. The average ratios $\overline{\Gamma_T^{SP}/\Gamma_{T=0}^{SP}}$ and $\overline{\Gamma_T^{MP}/\Gamma_{T=0}^{MP}}$ versus temperature for

Si_{46}.

The phonon density of state (DOS) of Si_{46} is plotted vs. wavenumber in Fig. 4-12, where the locations of $\bar{\omega}^{SP}$ and $\bar{\omega}^{MP}$ are also given as dashed lines. It is found that $\bar{\omega}^{SP}$ is located at the high-frequency regime of the phonon DOS spectrum. This implies that the high-frequency phonons contribute more to the single-phonon relaxation process than the low-frequency phonons. On the other hand, $\bar{\omega}^{MP}$ emerges at the low-frequency regime, close to the minimum phonon frequency. We thus speculate that the multiple-phonon relaxation proceeds mostly through the low-frequency phonons.

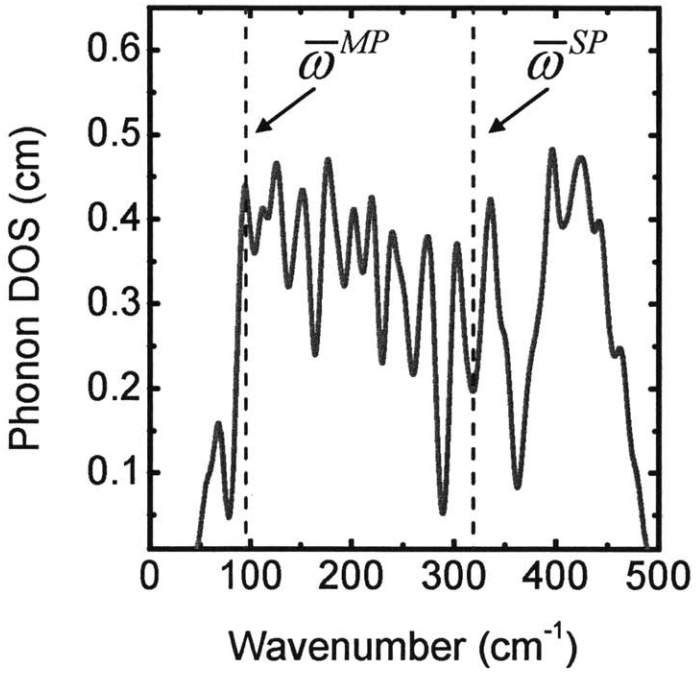

Figure 4-12. The phonon density of state (DOS) of Si_{46}, the locations of $\bar{\omega}^{SP}$ and $\bar{\omega}^{MP}$ are indicated as dashed lines.

4.4.3 Comparison between the electronic and excitonic nonradiative relaxation dynamics

The nonradiative relaxation dynamics of electronic states and excitonic states discussed in the two previous sections have demonstrated notable differences as can be seen by comparing Figs. 4-4 and 4-5 with Figs. 4-9 and 4-10. The observations are solely attributed to the difference between the electronic DOS and the excitonic DOS illustrated in Figs. 4-13a and 4-13b. It can be seen from Fig. 4-13 that the electronic DOS is in the order of tens per eV, while the excitonic DOS is around several hundreds per eV, namely one order of magnitude larger than the electronic DOS, and the excitonic DOS increases almost linearly with increasing exciton energy. The difference between the two types of DOS can be understood easily with a simple model, where the DOS of electrons is $g_c(E)$, and DOS of holes is $g_v(E)$. Then the DOS of excitons $g_{exc}(E)$ can be expressed approximately as a convolution of $g_c(E)$ and $g_v(E)$

$$g_{exc}(E) \approx \int dE' g_c(E'+E) g_v(E') \tag{4.33}$$

Eq. (4.33) explains why $g_{exc}(E)$ is a function that is one order or magnitude higher than $g_c(E)$ and $g_v(E)$, since the former is generated through the product of the later two. As a convolution, $g_{exc}(E)$ is also much smoother than $g_c(E)$ and $g_v(E)$. As long as $g_c(E)$ and $g_v(E)$ do not vary too dramatically in the energy range studied, we may further simply them as

$$g_c(E) = \begin{cases} C_1 & (E > 0) \\ 0 & (E < 0) \end{cases} \tag{4.34a}$$

$$g_v(E) = \begin{cases} 0 & (E > 0) \\ C_2 & (E < 0) \end{cases} \tag{4.34b}$$

Thus the convolution of $g_c(E)$ and $g_v(E)$ becomes a linear function C_1C_2E, which also explains the quasi-linear relation between $g_{exc}(E)$ and E shown in Fig. 4-13b.

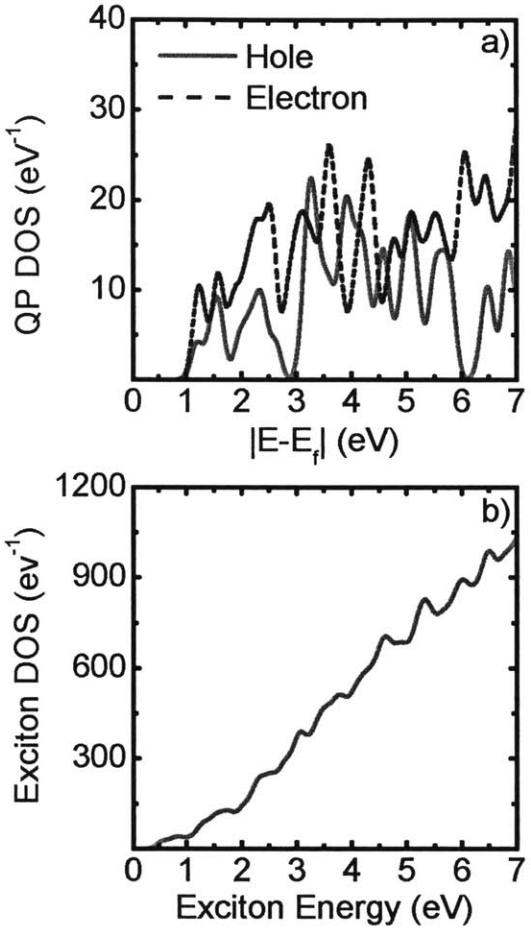

Figure 4-13. a) Electronic density of state (DOS) vs. energy deference from the Fermi level and b) Excitonic DOS of Si_{46} vs. exciton energy.

With the understanding of the difference between the electronic DOS and excitonic DOS, we revisit Fig. 4-4 and Fig. 4-9. In the case of nonradiative relaxation of electrons and holes (Fig. 4-4), the electronic DOS is not large enough to saturate every electronic state. (Here "saturate" means to provide all possible final states for the nonradiative decay of a given initial state.) Therefore, some states may present relatively low single-phonon or multiple-phonon relaxation rates due to lack of decay

pathways, which may occur even for those states with large excitation energies. In the case of nonradiative relaxation of excitons, however, the excitonic DOS increases quickly with increasing excitation energy and saturates those high-energy excitons very effectively. In summary, the calculation and analysis in the study uncover an important discovery: The nonradiative relaxation of excitons should always be investigated within the two-particle framework, otherwise the underlying physics will be missed and suspicious or plausible computational results will be presented.

4.5 Conclusion

We have established the computational methodology for electron-phonon and exciton-phonon interaction in nanoclusters. Using this method, we have investigated the dynamics of electrons and excitons in a silicon cluster of Si_{46}. The nonradiative relaxation rates of electrons and excitons are calculated. It is suggested that the single-phonon and multiple-phonon relaxation mechanisms should be studied separately, as the two mechanisms correspond to two types of physical processes and have totally different spectral lineshapes. The single-phonon relaxation mechanism shall correspond to a Lorentzian function, which can be accounted for by the imaginary part of an electron-phonon self-energy term. The multiple-phonon relaxation mechanism, on the other hand, shall be related to a Gaussian function, which corresponds to the thermal process and involves the anharmonic effect (displacement of the potential energy surface in finite systems). It is also demonstrated that the formula derived for the two relaxation mechanisms share a general form at the delta-function limit.

A simple energy criterion distinguishing the single-phonon relaxation and multiple-phonon relaxation has been proposed for practical implementation of the computation. Our numerical results show that the multiple-phonon relaxation rates always exist and are comparable to the corresponding single-phonon relaxation rates, for both electrons and excitons in the system studied (Si_{46}). Therefore it is necessary

to include the multiple-phonon relaxation mechanism when studying the nonradiative relaxation in small systems such as semiconductor nanoclusters.

Another important argument of this chapter is that the nonradiative relaxation of electronic states and that of excitonic states should always be distinguished, as the density of state (DOS) of excitons has been shown and proven to be much larger than the DOS of electrons. This leads to a significant difference between the relaxation dynamics of electrons and excitons. Electronic states, even those with high excitation energy, may present relatively slow nonradiative relaxation rates due to the lack of final states available for the decay transitions. For excitonic states, however, the nonradiative relaxation rate increases and converges quickly with increasing exciton energy, due to the large excitonic DOS.

The temperature effect of the nonradiative relaxation of excitons in Si_{46} has been investigated quantitatively. According to the average phonon frequencies derived from the data in the high-temperature regime, we speculate that both high- and low-frequency phonons contribute almost equally to the single-phonon relaxation pathway of excitons in Si_{46}, while low-frequency phonons are the major sources for the multiple-phonon relaxation mechanism.

The inelastic scattering rates of electrons and excitons are calculated using our developed code which is based on many-body Green's function theory. These results are also compared with the corresponding nonradiative relaxation rates. For the electronic states in Si_{46}, the inelastic scattering decay is predicted to be a major decay mechanism. However, nonradiative relaxation rates are larger than inelastic scattering rates for most excitonic states in Si_{46}, due to the large excitonic DOS.

Chapter 5

Relaxation dynamics of electrons and excitons in lead chalcogenide quantum dots

5.1 Introduction

The fundamentals and numerical implementation methodology for calculating nonradiative relaxation rates of electrons and excitons in semiconductor nanoclusters have been developed in the last chapter. Physically, the nonradiative relaxation rate is equivalent to the thermal exchange rate between the working fluid and the cylinder/piston system in the heat engine, an analogy discussed in Chapter 1. A practical question for a photovoltaic system is whether there is any strategy or method that can systematically minimize the energy exchange rate between electrons and phonons, so that any energy-conversion system based on this strategy can output more useful work and thus enhance the efficiency.

We start from an ideal case, where N electrons are constrained by a long stiff rod with positive charges uniformly distributed on it, as shown in Fig. 5-1a. Two schematic electronic wavefunctions are illustrated as the solid and dashed lines. The electrical potential due to the positive charges on the rod is shaded. The displacement of the rod along the x-direction can not couple the two electronic states, since the electrical potential does not change if the rod is very long. Therefore the coupling between the electrons and the movement of the rod disappear, and the rod behaves as an ideal adiabatic cylinder in the heat engine analogy.

Unfortunately such a positive charged rod does not exist in nature. What exists is a system with positive charges distributed on different nuclei as discretized particles, as shown in Fig. 5-1b. By assuming that the electronic wavefunctions do not change, the movement of one nucleus changes the local electrical potential, namely the potential term of the electronic Hamiltonian. In this case, an electron-phonon coupling can

occur due to the nonvanishing $\left\langle \varphi_j \left| \frac{\partial \varphi_i}{\partial Q_k} \right. \right\rangle$, where φ_i and φ_j are electronic wavefunctions, and the Q_k are nuclear coordinates as defined in Chap. 4. Therefore any external effects applied to drive the electrons to flow as electricity will suffer some energy loss due to the energy leakage from the electrons to the phonons.

A possible solution to this issue is to pull the electrons away from these nuclei, as shown in Fig. 5-1c. The electron-phonon coupling still exists in this case, yet the coupling strength is reduced dramatically due to the large distance between the electrons and nuclei. Practically, this strategy can be realized by introducing heavier atoms, whose core electrons push the valence electrons away from the nuclei. The valence-electron-separation effect may suppress the influence of the movement of nuclei on the valence electrons and this effect thus reduces the energy exchange rates between electrons and phonons. It is the quantum counterpart of the classical thermal insulation between the working fluids and the cylinder, and thus it can be regarded as "quantum thermal insulation".

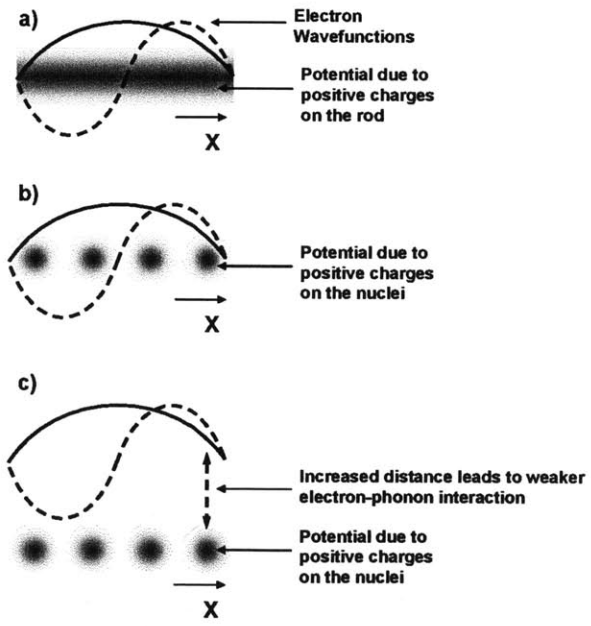

Figure 5-1. Schematic plots of a) electrons and a long stiff rod with positive charges uniformly distributed on it, b) electrons and positive charges discretized on different nuclei and c) electrons and positive charges discretized on different nuclei, but separated by a large distance, which leads to weaker electron-phonon interaction.

As an example of the valence-electron-separation, the radial wavefunctions of s- and p-orbitals of isolated sulfur, selenium and tellurium atoms obtained by the DFT code ATOM[35] are plotted in Figs. 5-2a and 5-2b. It is found that in heavier atoms, the major peaks of valence atomic orbitals are farther away from the nuclei. The molecular orbitals, which are obtained as the linear combination of these atomic orbitals, should also be farther away from the nuclei in a system composed of heavier atoms. Thus for systems with elements in the same columns of the periodic table, lower electron-phonon relaxation rates are anticipated in those containing heavier atoms due to the larger valence-electron-separation effect.

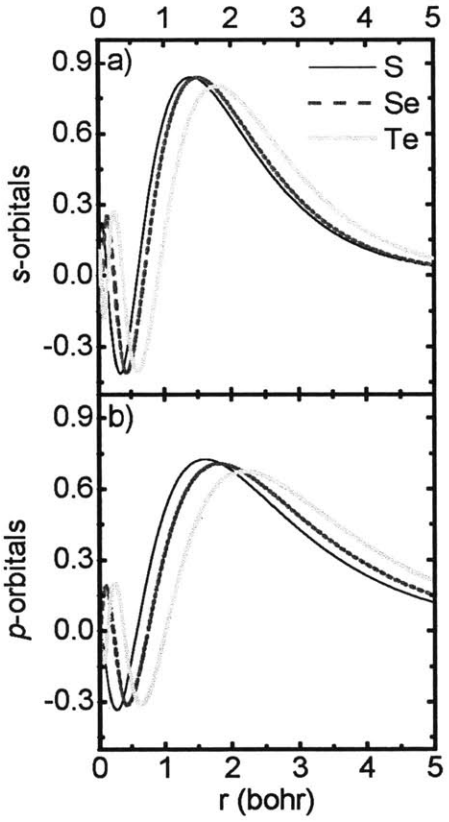

Figure 5-2. Radial wavefunctions of a) *s*- and b) *p*-orbitals of valence electrons in isolated sulfur, selenium and tellurium atoms obtained by DFT, where each of these elements are chalcogen elements.

5.2 Numerical details

All methods required for the simulation of dynamics in finite 0D nanoclusters have been developed in Chaps. 2, 3 and 4. Now we can apply the tool kit for a realistic problem: lead chalcogenide nanoclusters, which are frequently used in solar cells. Both the inelastic scattering rates and nonradiative relaxation rates of excitons in such nanoclusters are very interesting and have drawn a lot of attention. Bulk lead chalcogenides (PbS, PbSe and PbTe) have a rocksalt structure. Small cubes of this kind of lattice, such as $(PbX)_4$ and $(PbX)_{32}$ (X=S, Se and Te), exhibit T_d symmetry with triple degenerate states. To avoid any degeneracy, a structure preserves the rocksalt lattice and with only the D_{2h} symmetry, $(PbX)_{36}$ is used in this chapter. The valence-electron-separation effect proposed in the last section will be investigated by comparing the nonradiative relaxation rates of excitons in three clusters: $(PbS)_{36}$, $(PbSe)_{36}$ and $(PbTe)_{36}$.

Note that Pb itself is a heavy atom and shall also have some contribution to the valence-electron-separation effect, which can be studied by replacing Pb with Sn or even Ge. However, SnX and GeX (X=S, Se and Te) are rarely reported for multiple exciton generation applications. Therefore in this thesis, we focus on the effect of the chalcogen elements.

The ground state LDA calculation is performed using the SIESTA code.[35] The core electrons of Pb, S, Se and Te are replaced by the nonlocal norm-conserving scalar relativistic pseudopotential based on the Troullier-Martins scheme.[36] A quintuple-ζ polarization (5ZP) basis set of numerical atomic orbitals is used for the valence electrons of all elements involved in the simulation. The optimized structure of the $(PbX)_{36}$ (X=S, Se and Te) cluster is illustrated in Fig. 5-3, which has the same crystal lattice as the corresponding bulk PbX structure, namely the rocksalt structure. The structure exhibits D_{2h} symmetry and thus there are no degenerate electron, exciton, phonon states. This lack of degenerate states facilitates our study dramatically since

we can focus the discussion solely on the valence-electron-separation effect, without considering the Jahn-Teller effect arising from the degeneracy.

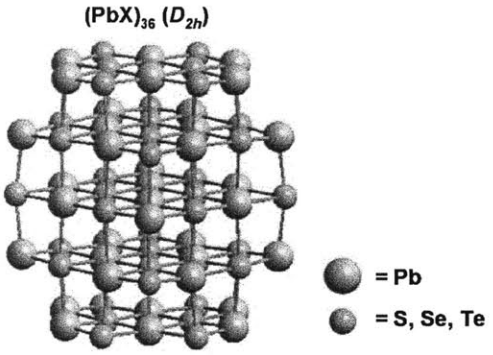

Figure 5-3. Optimized structure of $(PbX)_{36}$ with the D_{2h} symmetry.

All integrals are evaluated on a uniform grid in real space with a grid spacing of 0.5 a.u.. The exchange integrals $\int d\mathbf{r}\int d\mathbf{r}'\varphi_i(\mathbf{r})\varphi_j(\mathbf{r})V(\mathbf{r},\mathbf{r}')\varphi_k(\mathbf{r}')\varphi_l(\mathbf{r}')$ are evaluated by first solving Poisson equations with the multigrid method.[37] A Coulomb-hole screened-exchange (COHSEX) remainder scheme[33] has been applied to accelerate the convergence of the correlation part $\langle\varphi_i|\Sigma_c|\varphi_i\rangle$.

The properties of the one-particle states are obtained by solving the quasiparticle equation introduced in Chap. 2

$$\left(\hat{T}+V_{ext}+V_H\right)\varphi_i(\mathbf{r})+\int d\mathbf{r}'\Sigma_{xc}(\mathbf{r},\mathbf{r}';E_i)\varphi_i(\mathbf{r}')=E_i\varphi_i(\mathbf{r}) \tag{5.1}$$

After applying analytical continuation of $\Sigma_c(\mathbf{r},\mathbf{r}';E)$ in the complex energy plane, the energy E_i and the inelastic scattering rates γ_i of an electronic state are obtained by solving a complex equation set numerically

$$\mathrm{Re}\langle\varphi_i|\Sigma_{xc}(E_i-i\eta_i\gamma_i)|\varphi_i\rangle-\langle\varphi_i|V_{xc}|\varphi_i\rangle=E_i-\varepsilon_i \tag{5.2a}$$

$$\left|\mathrm{Im}\langle\varphi_i|\Sigma_{xc}(E_i-i\eta_i\gamma_i)|\varphi_i\rangle\right|=\gamma_i \tag{5.2b}$$

The inelastic scattering rates of excitons are calculated with the approximation method developed in Chap. 3:

$$\Gamma_s = \sum_{v,c} \left| R_s^{vc} \right|^2 \left(\gamma_c + \gamma_v \right) \tag{5.3}$$

where R_s^{vc} are the coefficients of the linear combination of the sth exciton obtained by TDLDA, namely

$$\rho_s(\mathbf{r}) = \sum_{v,c} R_s^{vc} \varphi_v^*(\mathbf{r}) \varphi_c(\mathbf{r}) \tag{5.4}$$

Following the methods in Chap. 4, the single-phonon relaxation rates of electrons are calculated by

$$\gamma_i^{SP} = \sum_{j,|E_j|<|E_i|} \sum_k \frac{\hbar^2}{M_k} \left| C_k^{ij} \right|^2 \hbar\omega_k \left[\frac{(n_k+1)\gamma_i^{SP}}{\left(\Delta E_{ij} - \hbar\omega_k\right)^2 + \left(\gamma_i^{SP}\right)^2} + \frac{n_k \gamma_i^{SP}}{\left(\Delta E_{ij} + \hbar\omega_k\right)^2 + \left(\gamma_i^{SP}\right)^2} \right] \tag{5.5}$$

where M_k are the masses of the normal coordinates Q_k, while $C_k^{i,j} = \left\langle \varphi_j \left| \partial / \partial Q_k \right| \varphi_i \right\rangle$, and $\Delta E_{ij} = E_i - E_j$. γ_i^{SP} is the width of the Lorentzian function corresponding to the ith electron, which is exactly the single-phonon decay rate to be determined. The multiple-phonon relaxation rates of electrons are evaluated as

$$\gamma_i^{MP} = \sum_{j,|E_j|<|E_i|} \sum_k \frac{\hbar^2}{M_k} \left| C_k^{ij} \right|^2 \hbar\omega_k \pi \frac{1}{\hbar D_{ij}^k \sqrt{2\pi}} \left(\begin{array}{l} (n_k+1) \exp\left(-\dfrac{\left(\Delta E_{ij} - \hbar\omega_k\right)^2}{2\hbar^2 \left(D_{ij}^k\right)^2} \right) \\ + n_k \exp\left(-\dfrac{\left(\Delta E_{ij} + \hbar\omega_k\right)^2}{2\hbar^2 \left(D_{ij}^k\right)^2} \right) \end{array} \right) \tag{5.6}$$

with

$$\left(D_{ij}^{k}\right)^2 = \frac{1}{2}\sum_{k}\omega_k^2\left(\Delta_k^{ij}\right)^2\left(2n_k+1\right)$$

$$n_k = \frac{1}{\exp\left(\hbar\omega_k/k_BT\right)-1}$$

For excitonic states,

$$C_k^{i,j} = \left\langle \rho_j \left| \partial/\partial Q_k \right| \rho_i \right\rangle = \sum_{v,c}\sum_{v',c'} R_{vc}^{i} R_{v'c'}^{j}\left(\delta_{vv'}\left\langle \varphi_c \left| \partial/\partial Q_k \right| \varphi_{c'} \right\rangle + \delta_{cc'}\left\langle \varphi_v \left| \partial/\partial Q_k \right| \varphi_{v'} \right\rangle\right) \quad (5.7)$$

5.3 Results and discussion

5.3.1 Electronic relaxation dynamics in $(PbX)_{36}$ clusters

The inelastic scattering rates γ^{IS} of electrons and holes in $(PbX)_{36}$ (X=S, Se and Te) calculated by the *GWT* method are plotted versus the excitation energy $|E_i - E_F|$ in log-log style in Figs. 5-4a to 5-4c. In general, the γ^{IS} values of the three clusters are close to each other in the energy range of 3.5 ~ 6.0 eV, because the three clusters have the same number of valence electrons (360) and similar lattice arrangements. The only difference is that γ^{IS} of the clusters with heavier elements can extend into the lower energy regime.

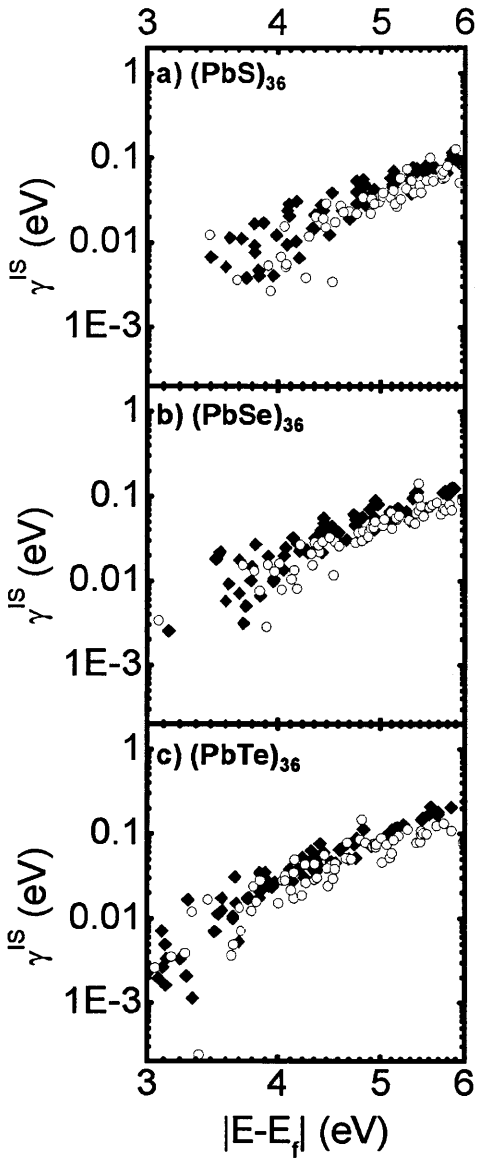

Figure 5-4. The inelastic scattering rates γ^{IS} of electrons (hollow circles) and holes (solid diamonds) vs. excitation energy for the three clusters a) $(PbS)_{36}$, b) $(PbSe)_{36}$ and c) $(PbTe)_{36}$.

The single-phonon nonradiative relaxation rates γ^{SP} of electrons and holes in $(PbX)_{36}$ (X=S, Se and Te) at 0 K obtained by Eq. (5.5) are plotted versus the excitation energy $|E_i - E_F|$ in Figs. 5-5a to 5-5c. Sparser data points can be found for

clusters with heavier atoms, implying that more electronic states have vanishing γ^{SP}. This result is attributed to the lower phonon frequencies of clusters with heavier atoms, which are less capable of covering the gap between any two neighboring electronic states for the single-phonon decay pathway. Note that this is just an additional effect of using heavy atoms, which is a different effect from the valence-electron-separation mechanism discussed in Chap. 5.1.

The multiple-phonon nonradiative relaxation rates γ^{MP} at 0K for the three clusters are presented in Figs. 5-5d to 5-5f. Since the patterns of γ^{MP} are quite largely dispersive, it is difficult to compare γ^{MP} in the three clusters quantitatively. However, Figs. 5-3d to 5-3f still demonstrate two reasons to include the multiple-phonon decay pathway for the study of nonradiative rates for finite systems. Firstly, the relaxation rates of the multiple-phonon process are comparable to those of the single-phonon process for some electronic states. Secondly, and more importantly, all electronic states (except for the HOMO and LUMO levels of each cluster) can decay through the multiple-phonon relaxation pathway, which is an alternative nonradiative decay pathway when the single-phonon relaxation process is absent due to large energy gaps.

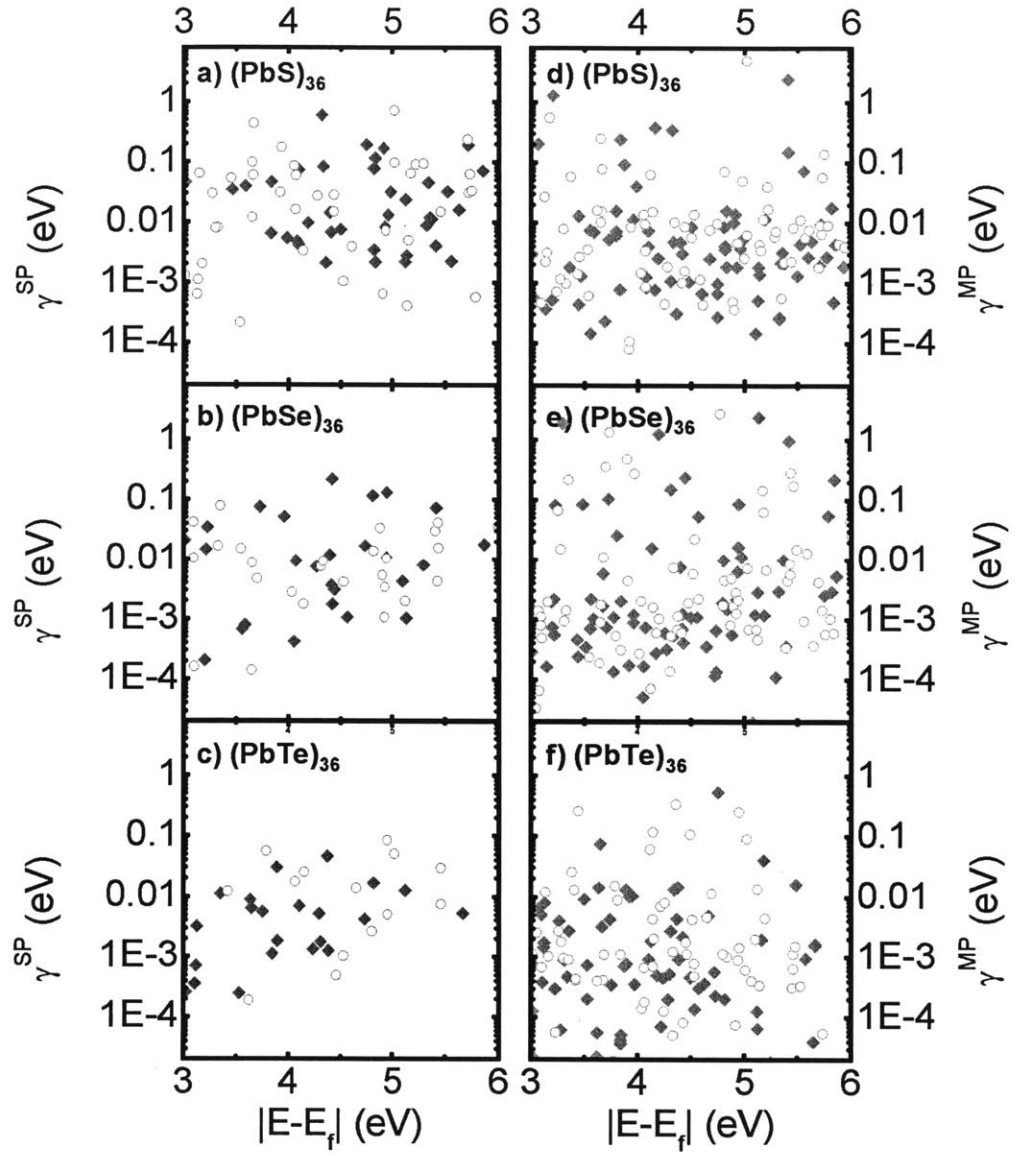

Figure 5-5. Single-phonon nonradiative relaxation rates γ^{SP} of electrons (hollow circles) and holes (solid diamonds) at 0 K vs. excitation energy in a) $(PbS)_{36}$, b) $(PbSe)_{36}$ and c) $(PbTe)_{36}$. Multiple-phonon nonradiative relaxation rates γ^{MP} of electrons (hollow circles) and holes (solid diamonds) at 0 K vs. excitation energy in d) $(PbS)_{36}$, e) $(PbSe)_{36}$ and f) $(PbTe)_{36}$.

The corresponding ratios $\gamma^{IS}/\gamma^{SP+MP}$ ($\gamma^{SP+MP} = \gamma^{SP} + \gamma^{MP}$) in the three clusters are plotted in Figs. 5-6a to 5-6c for the comparison of the inelastic scattering rates and the

nonradiative relaxation rates of electronic states. The patterns of $\gamma^{IS}/\gamma^{SP+MP}$ of the three clusters are similar to that of Si_{46} shown in Fig. 4-5, and so are the conclusions. Furthermore, the valence-electron-separation effect can be found by comparing Figs. 5-6a through 5-6c: the figures show that $\gamma^{IS}/\gamma^{SP+MP}$ of $(PbTe)_{36}$ are approximately one order of magnitude higher than those of $(PbS)_{36}$. This implies that γ^{SP+MP} in $(PbTe)_{36}$ are indeed smaller than those in $(PbS)_{36}$, since γ^{IS} in the two clusters are close to each other. The valence-electron-separation effect as well as the temperature effect will be further discussed in the next subsection, 5.3.2.

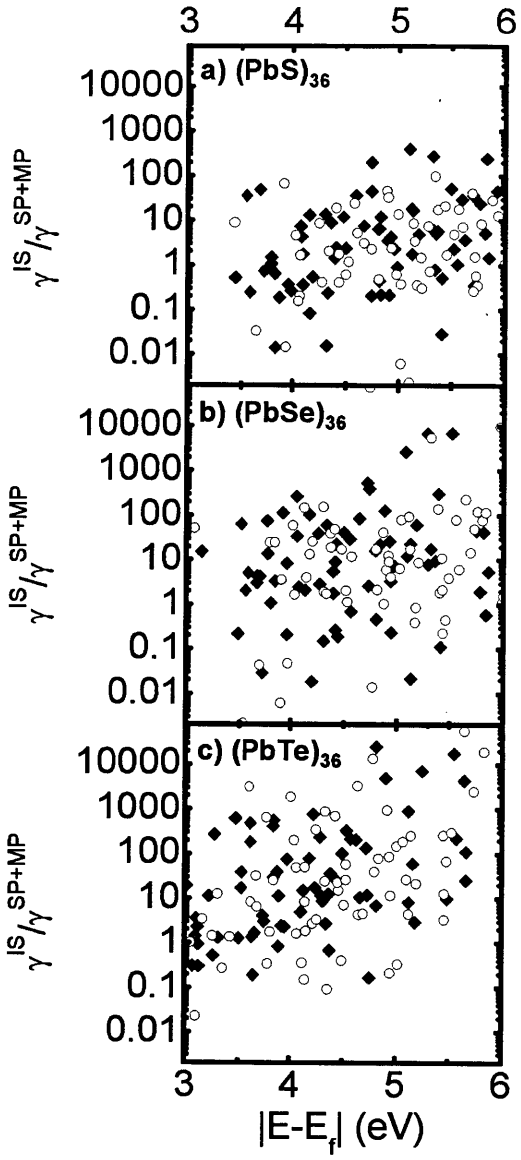

Figure 5-6. The ratios $\gamma^{IS}/\gamma^{SP+MP}$ for electrons (hollow circles) and holes (solid diamonds) vs. excitation energy in a) $(PbS)_{36}$, b) $(PbSe)_{36}$ and c) $(PbTe)_{36}$ at 0 K, where $\gamma^{SP+MP} = \gamma^{SP} + \gamma^{MP}$.

5.3.2 Excitonic relaxation dynamics in $(PbX)_{36}$ clusters

The inelastic scattering rates Γ^{IS} of excitons in $(PbX)_{36}$ (X=S, Se and Te) calculated by the approximation method given by Eq. (5.3) are plotted versus the

exciton energy Ω in log-log style in Figs. 5-7a to 5-7c, where the solid lines are the curve fitting of Γ^{IS} by a simple rational function (Padé function P_1^2)

$$y^{IS} = 2x + a + \frac{b}{x+c} \tag{5.8}$$

where x and y represent $\ln(\Omega/\mathrm{eV})$ and $\ln(\Gamma^{IS}/\mathrm{eV})$, respectively. The fitting coefficients a, b and c are given in Table 5.1.

Table 5.1. Fitting coefficients a, b and c in $(PbX)_{36}$ (X=S, Se and Te) for Eq. (5.8)

	$(PbS)_{36}$	$(PbSe)_{36}$	$(PbTe)_{36}$
a	-2.32	-2.40	-2.27
b	-0.22	-0.14	-0.16
c	-0.35	-0.40	-0.39

For the comparison of Γ^{IS} in the three clusters, the three fitting curves in Fig. 5-7 are re-plotted in Fig. 5-8, where we can see that the Γ^{IS} values for these three clusters, like γ^{IS}, are again very close to each other over the full energy range of interest.

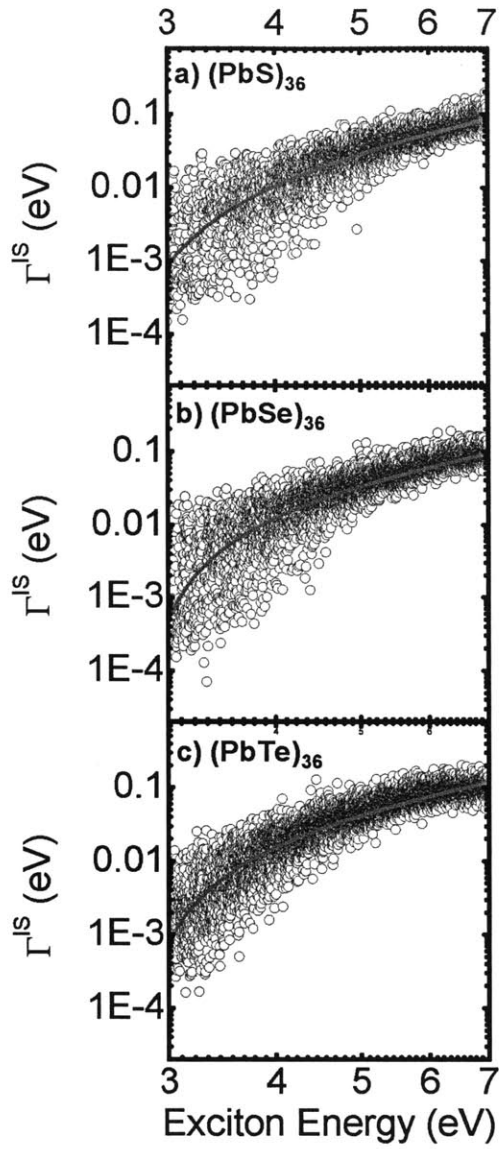

Figure 5-7. Exciton energy dependence of inelastic scattering rates Γ^{IS} of excitons in a) $(PbS)_{36}$, b) $(PbSe)_{36}$ and c) $(PbTe)_{36}$. The solid lines are the curve-fittings based on Eq. (5.8).

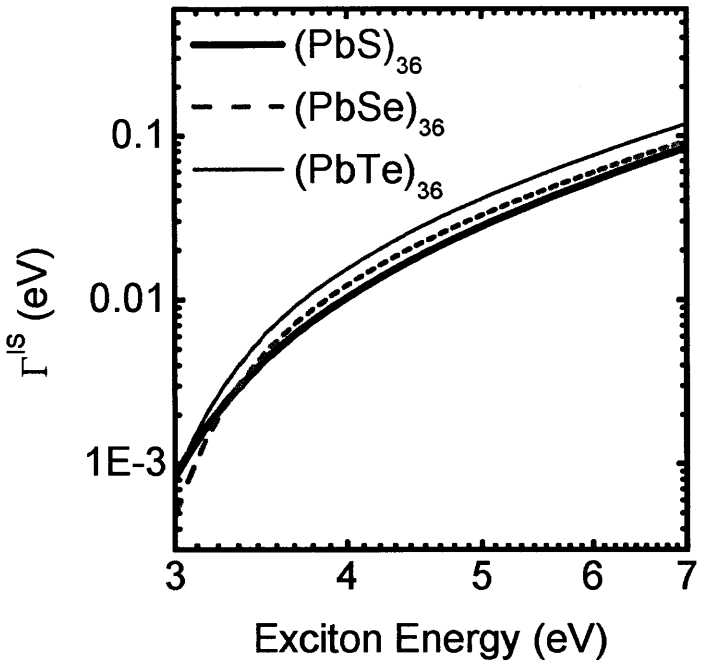

Figure 5-8. Fitted inelastic scattering rates Γ^{IS} of excitons vs. exciton energy for $(PbS)_{36}$, $(PbSe)_{36}$ and $(PbTe)_{36}$.

The single-phonon nonradiative relaxation rates Γ^{SP} of excitons in $(PbX)_{36}$ (X=S, Se and Te) at 0 K obtained by Eq. (5.5) are plotted versus the excitation energy Ω_s in Figs. 5-9a to 5-9c. The multiple-phonon nonradiative relaxation rates Γ^{MP} of excitons in these three clusters at 0 K are plotted in Figs. 5-9d to 5-9f. Similar to Si_{46} discussed in the last chapter, all three $(PbX)_{36}$ clusters exhibit energy-dependent Γ^{SP} and Γ^{MP} in the low-energy regime. The energy-dependence diminishes in the high-energy regime and the patterns of Γ^{SP} and Γ^{MP} become flat due to the large excitonic density of state (DOS) that saturates the exciton-phonon relaxation pathways. The patterns of both Γ^{SP} and Γ^{MP} are fitted numerically with an exponential function

$$y^{SP} = y_0^{SP} + A^{SP} e^{-(\Omega-\Omega_0^{SP})/t^{SP}} \tag{5.9a}$$

$$y^{MP} = y_0^{MP} + A^{MP} e^{-(\Omega-\Omega_0^{MP})/t^{MP}} \tag{5.9b}$$

where y^{SP} and y^{MP} represent $\log(\Gamma^{SP}/\text{eV})$ and $\log(\Gamma^{MP}/\text{eV})$, while Ω is the excitonic energy. The quantities y_0^{SP}, A^{SP}, Ω_0^{SP}, t^{SP} and their multiple-phonon counterparts are fitting parameters. The fitting curves are also plotted in Figs. 5-9a to 5-9f as solid lines.

The converged relaxation rates at 0 K, namely $\Gamma_0^{SP} = 10^{y_0^{SP}}$ for single-phonon decay and $\Gamma_0^{MP} = 10^{y_0^{MP}}$ for multiple-phonon decay, are listed in Table 5.2 for all three clusters. According to Figs. 5-9a to 5-9f and Table 5.2, Γ^{MP} are always comparable to Γ^{SP} over the full energy range which is important for all three clusters. The results demonstrate again that it is necessary to include the multiple-phonon decay mechanism for the simulation of nonradiative relaxation rates. Valence-electron-separation effect is also proved, as clusters with heavier atoms exhibit lower Γ^{SP} and Γ^{MP} values.

Table 5.2. Converged relaxation rates Γ_0^{SP} and Γ_0^{MP} in $(PbX)_{36}$ (X=S, Se and Te) at 0K

	$(PbS)_{36}$	$(PbSe)_{36}$	$(PbTe)_{36}$
Γ_0^{SP} (eV)	0.133	0.0514	0.0189
Γ_0^{MP} (eV)	0.234	0.0665	0.0199

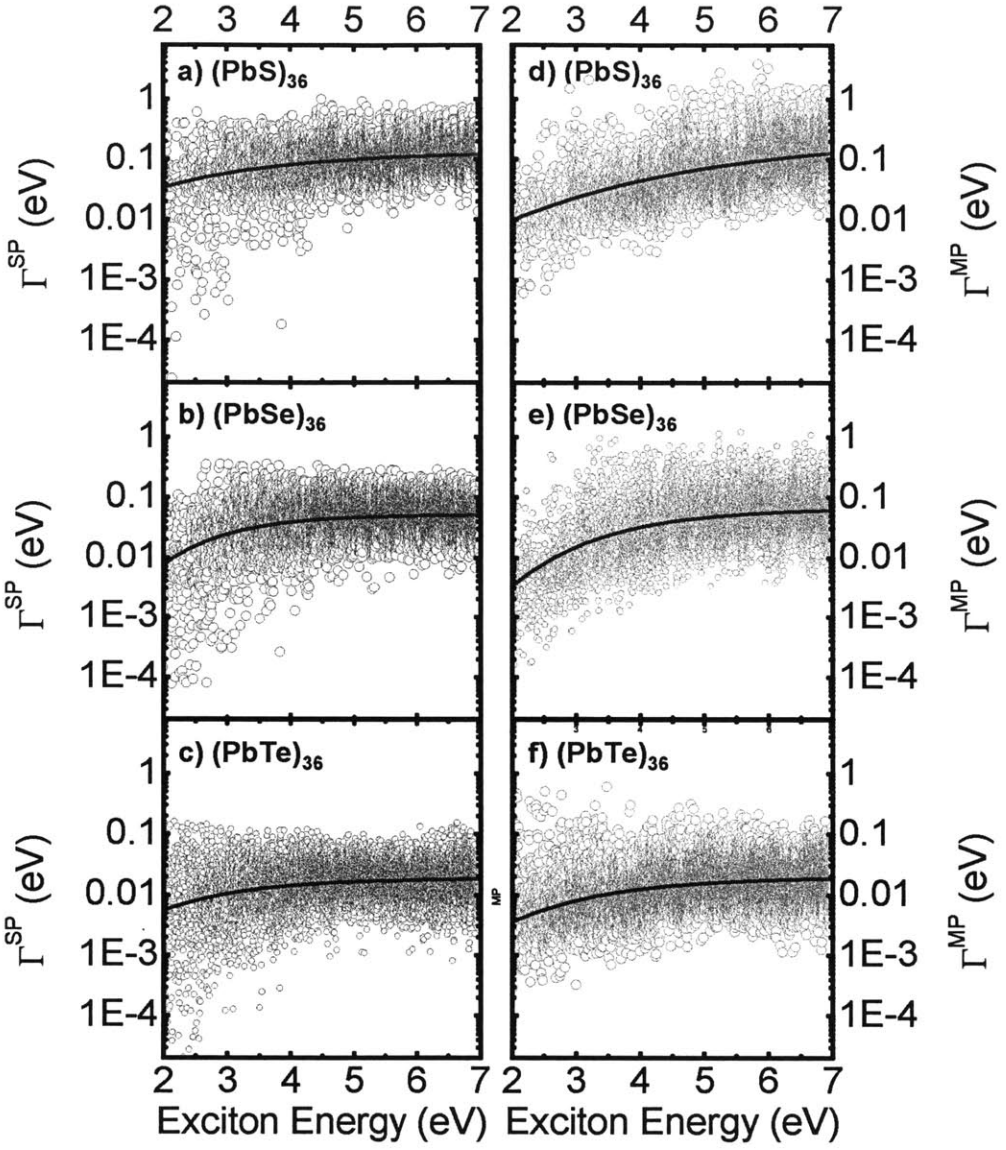

Figure 5-9. Single-phonon nonradiative relaxation rates Γ^{SP} of excitons at 0 K vs. exciton energy in a) $(PbS)_{36}$, b) $(PbSe)_{36}$ and c) $(PbTe)_{36}$. Multiple-phonon nonradiative relaxation rates Γ^{MP} of excitons at 0 K vs. exciton energy in d) $(PbS)_{36}$, e) $(PbSe)_{36}$ and f) $(PbTe)_{36}$. Solid lines are fitting curves based on Eq. (5.9).

The ratios $\Gamma^{IS}/\Gamma^{SP+MP}$ ($\Gamma^{SP+MP}=\Gamma^{SP}+\Gamma^{MP}$) are plotted in Figs. 5-10a to 5-10c vs. exciton energy for the comparison of the inelastic scattering rates and the nonradiative relaxation rates of excitonic states in the three clusters. From Figs. 5-10a and 5-10c, one can find that the ratio $\Gamma^{IS}/\Gamma^{SP+MP}$ of $(PbTe)_{36}$ is approximately one order of

magnitude higher than that of $(PbS)_{36}$, which is mostly due to smaller Γ^{SP+MP} of $(PbTe)_{36}$. The ratios here, however, are notably smaller than those in Figs. 5-6a to 5-6c. This is attributed to the significantly larger DOSs of the excitonic states than those of the electronic states. The detailed analysis for the DOS effect has been discussed in the last chapter for Si_{46}.

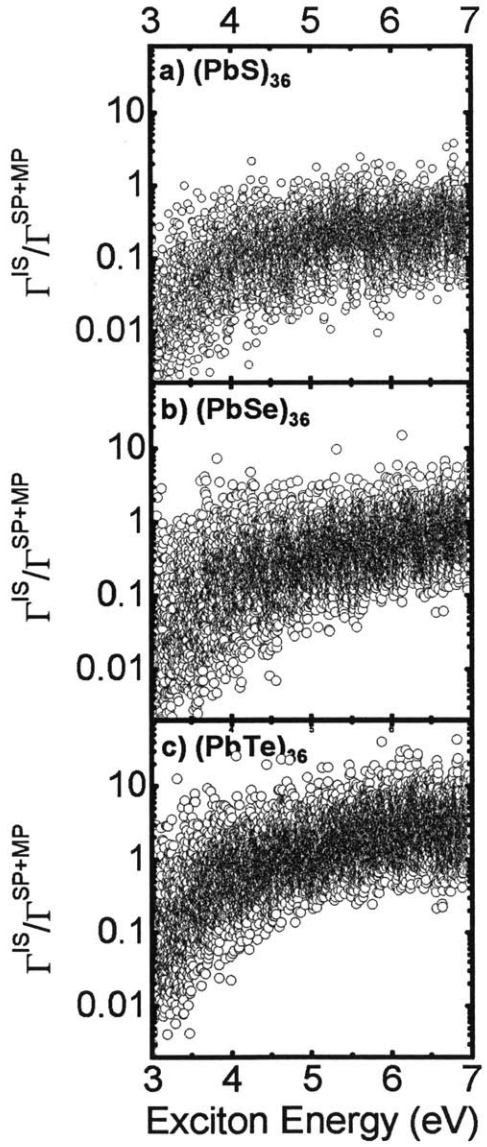

Figure 5-10. The ratios $\Gamma^{IS}/\Gamma^{SP+MP}$ for exctions vs. exciton energy in a) $(PbS)_{36}$, b) $(PbSe)_{36}$ and c) $(PbTe)_{36}$ at 0 K, where $\Gamma^{SP+MP} = \Gamma^{SP} + \Gamma^{MP}$.

The temperature effects are investigated by re-calculating Γ^{SP} and Γ^{MP} at

various temperatures. Similar to the case of Si_{46}, we here focus our study on the temperature dependence of the average ratios $\overline{\Gamma_T^{SP}/\Gamma_{T=0}^{SP}}$ and $\overline{\Gamma_T^{MP}/\Gamma_{T=0}^{MP}}$, which are plotted versus temperature for the three clusters in Figs. 5-11a to 5-11c. According to Eqs. (5.5) and (5.6),

$$\overline{\Gamma_T^{SP}/\Gamma_{T=0}^{SP}} \approx \left(2\bar{n}^{SP}+1\right)^{1/2} \approx \left(\frac{2k_BT}{\hbar\bar{\omega}^{SP}}\right)^{1/2} + C^{SP} \qquad (5.10a)$$

$$\overline{\Gamma_T^{SP}/\Gamma_{T=0}^{SP}} \approx \left(2\bar{n}^{MP}+1\right)^{1/2} \approx \left(\frac{2k_BT}{\hbar\bar{\omega}^{MP}}\right)^{1/2} + C^{MP} \qquad (5.10b)$$

where the last approximate equality is valid only in the high temperature limit.

The characteristic phonon frequencies, $\bar{\omega}^{SP}$ and $\bar{\omega}^{MP}$ for single-phonon and multiple-phonon relaxation processes, can be determined through the coefficients of the $T^{1/2}$ terms in Eqs. (5.10a) and (5.10b). Estimated $\bar{\omega}^{SP}$ and $\bar{\omega}^{MP}$ in the three clusters are listed in Table 5.3. The phonon DOSs of the three clusters are plotted in Figs. 5-12a to 5-12c, where the locations of $\bar{\omega}^{SP}$'s and $\bar{\omega}^{MP}$'s are also given as dashed lines. It is found that the maximum phonon frequencies are lower for clusters with heavier chalcogen atoms as expected. Also, the relative positions of $\bar{\omega}^{SP}$'s and $\bar{\omega}^{MP}$'s suggest that the single-phonon relaxation process is more dominated by the high-frequency phonons while the multiple-phonon relaxation process is more dominated by the low-frequency phonons.

Table 5.3. Characteristic phonon frequencies $\bar{\omega}^{SP}$ and $\bar{\omega}^{MP}$ in $(PbX)_{36}$ (X=S, Se and Te)

	$(PbS)_{36}$	$(PbSe)_{36}$	$(PbTe)_{36}$
$\bar{\omega}^{SP}$ (cm^{-1})	229	132	75.1
$\bar{\omega}^{MP}$ (cm^{-1})	75.0	37.1	19.6

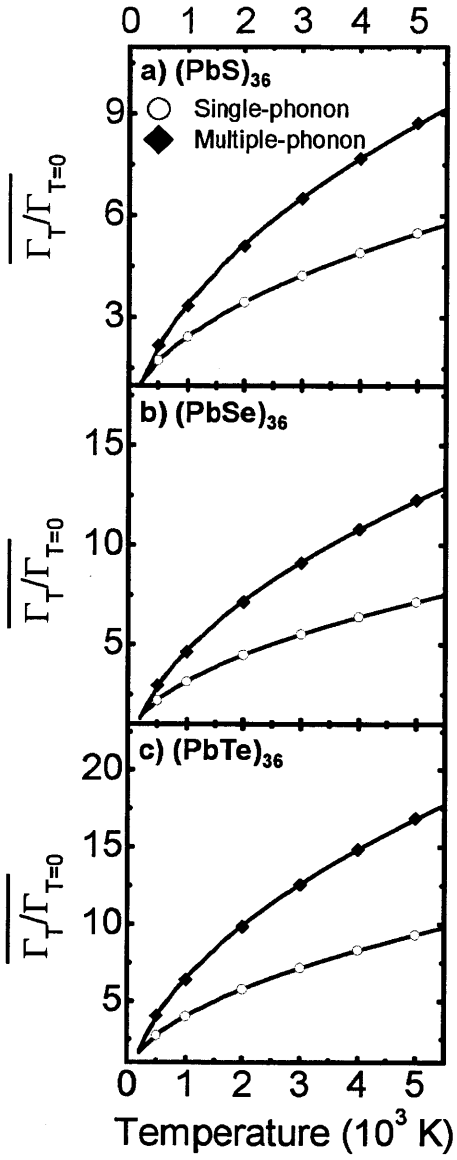

Figure 5-11. The average ratios $\overline{\Gamma_T^{SP}/\Gamma_{T=0}^{SP}}$ and $\overline{\Gamma_T^{MP}/\Gamma_{T=0}^{MP}}$ versus temperature for a) $(PbS)_{36}$, b) $(PbSe)_{36}$ and c) $(PbTe)_{36}$.

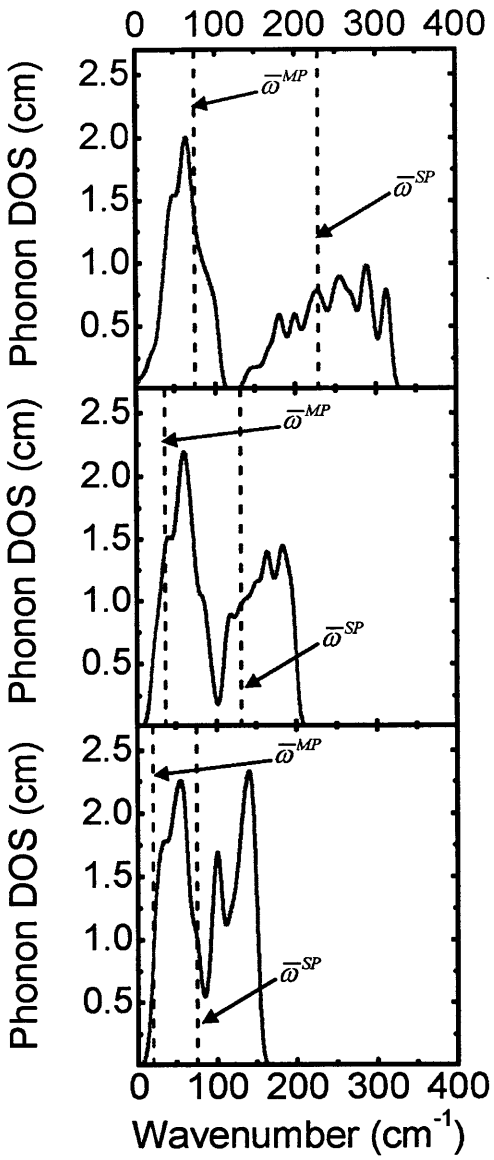

Figure 5-12. Phonon DOSs of a) $(PbS)_{36}$, b) $(PbSe)_{36}$ and c) $(PbTe)_{36}$ vs. wavenumber and the locations of $\bar{\omega}^{SP}$ and $\bar{\omega}^{MP}$ are indicated as dashed lines.

5.4 Conclusion

We have presented a possible mechanism for reducing the electron-phonon coupling in semiconductor nanoclusters. The strategy is based on the physics that the valence electrons in heavier atoms are pushed farther away from the nuclei by the core electrons and thus are less sensitive to the movement of nuclei. This may

suppress the energy exchange rate between the electrons and phonons, and lead to "quantum thermal insulation".

Electronic and excitonic nonradiative relaxation rates in lead chalcogenide nanoclusters $(PbX)_{36}$ (X=S, Se and Te) have been calculated by our numerical methods developed in Chap. 4. Our simulation results show that the electronic and excitonic nonradiative relaxation rates are lower in clusters with heavier atoms, and that they thus demonstrate the valence-electron-separation effect. As a by-product, heavier atoms also exhibit a mass effect by reducing the maximum phonon frequency. This effect makes the single-phonon relaxation decay process unlikely for electronic states due to the relatively large energy gaps. For excitonic states, on the other hand, such an effect is insignificant.

The results obtained in this chapter (chapter 5) are consistent with the conclusions drawn in the last chapter (chapter 4). Firstly, the multiple-phonon relaxation rates always exist and are comparable to the corresponding single-phonon relaxation rates, for both electronic and excitonic states in nanoclusters. Secondly, the nonradiative relaxation of electronic states and that of excitonic states should always be distinguished, due to the significant difference between the electronic DOS and excitonic DOS. Thirdly, two characteristic phonon frequencies $\bar{\omega}^{SP}$ and $\bar{\omega}^{MP}$ can be defined according to the temperature-dependence of the nonradiative relaxation rates. It is speculated that the single-phonon relaxation process in nanoclusters is always dominated by high-frequency phonons while this is not the case for the multiple-phonon relaxation process.

The inelastic scattering rates of electrons and excitons in the lead chalcogenide nanoclusters $(PbX)_{36}$ (X=S, Se and Te) are calculated by the many-body Green's function theory discussed in Chaps. 2 and 3. The electronic and excitonic inelastic scattering rates do not differ too much in clusters with different chalcogen elements, since the three clusters have the same number of valence electrons (360) and similar

lattice arrangements. The results imply that the valence-electron-separation effect has a negligible effect on the energy exchange rates among electrons and excitons.

Chapter 6

Relaxation dynamics of excitons in porphyrin and a porphyrin derivative

6.1 Introduction

In Chaps. 3 and 4, we developed simulation methods for calculating the inelastic scattering rates and nonradiative relaxation rates of excitons in nanoclusters. In Chap. 5, we demonstrated that the energy exchange rates between excitons and phonons in semiconductor nanoclusters can be reduced by introducing heavier atoms into the system. The physics behind this idea is to push the valence electrons away from the nuclei by core electrons, so that the movements of these nuclei can not couple any two valence electronic states effectively.

In addition to inorganic semiconductor nanoclusters, there is another nature type of semiconductor system at the nanoscale, namely organic semiconductor molecules. In this chapter, we apply our computational approach to a typical organic semiconductor molecule, porphyrin. As shown in Fig. 6-1, there are fourteen H atoms in a porphyrin molecule. Here twelve side H atoms can be substituted by halogen atoms. The two H atoms at the center act like protons in sulfuric acid and can be dissociated in alkaline solution. After the dissociation of these two H atoms, the porphyrin structure can be coordinated with metal cations, such as Zn^{2+}, Mg^{2+}.

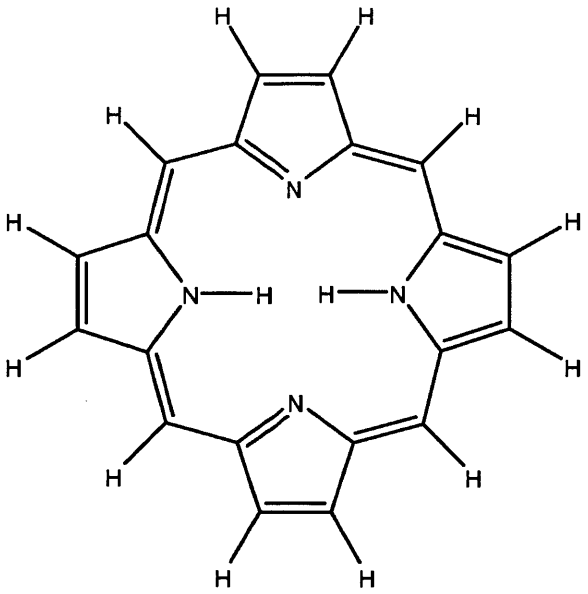

Figure 6-1. Chemical structure of a porphyrin molecule.

By replacing the 12 side H atoms with halogen atoms and the 2 central H atoms with a metal atom, a porphyrin derivative structure is produced. Investigations of the nonradiative relaxation rates of excitons in a pristine porphyrin molecule and a porphyrin derivative uncovers the exciton-phonon interaction in organic molecules and could lead to methods to reduce the phonon effect in organic semiconductor molecules with the strategy proposed in Chap. 5.

6.2 Numerical details

The ground state LDA calculation is performed using the SIESTA code.[35] The core electrons of C, N, F, Cl and Zn are replaced by the nonlocal norm-conserving pseudopotential based on the Troullier-Martins scheme.[36] A quadruple-ζ polarization (4ZP) basis set of numerical atomic orbitals is used for the valence electrons of all elements involved in the simulation. The optimized structures of porphyrin and a porphyrin derivative, whose side H atoms are replaced by F and Cl atoms, and the center H atoms are replaced by a Zn ion, are illustrated in Fig. 6-2. The two structures are denoted by Por and ZnPorFCl in later discussions. Both structures exhibit the D_{2h}

symmetry and thus there are no degenerate electron, exciton, or phonon states. This facilitates our study dramatically since we can focus the discussion solely on the valence-electron-separation effect, without considering the Jahn-Teller effect arising from the degeneracy.

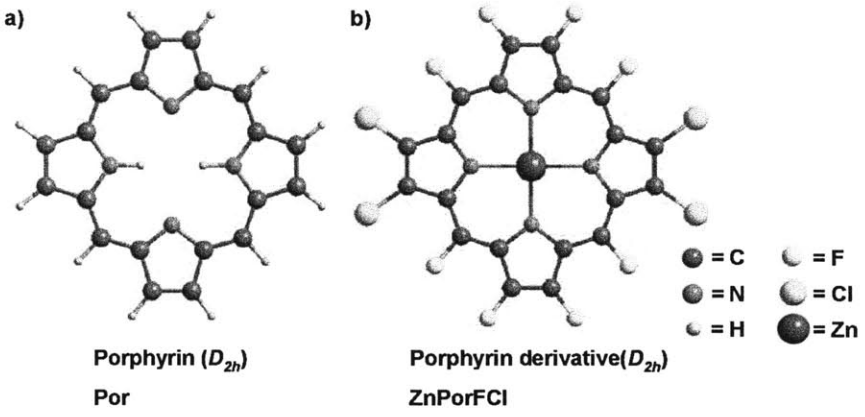

Figure 6-2. Optimized structure of a porphyrin molecule and a porphyrin derivative, both with the D_{2h} symmetry.

All integrals are evaluated on a uniform grid in real space with a grid spacing of 0.3 a.u.. The exchange integrals $\int d\mathbf{r}\int d\mathbf{r}'\varphi_i(\mathbf{r})\varphi_j(\mathbf{r})V(\mathbf{r},\mathbf{r}')\varphi_k(\mathbf{r}')\varphi_l(\mathbf{r}')$ are evaluated by first solving Poisson equations with the multigrid method.[37] A Coulomb-hole screened-exchange (COHSEX) remainder scheme[33] has been applied to accelerate the convergence of the correlation part $\langle\varphi_i|\Sigma_c|\varphi_i\rangle$.

The properties of the one-particle states are obtained by solving the quasiparticle equation introduced in Chap. 2

$$\left(\hat{T}+V_{ext}+V_H\right)\varphi_i(\mathbf{r})+\int d\mathbf{r}'\Sigma_{xc}(\mathbf{r},\mathbf{r}';E_i)\varphi_i(\mathbf{r}')=E_i\varphi_i(\mathbf{r}) \qquad (6.1)$$

After applying the condition of analytical continuation of $\Sigma_c(\mathbf{r},\mathbf{r}';E)$ in the complex energy plane, the energy E_i and the inelastic scattering rates γ_i of an electronic state are obtained by solving a complex equation set numerically

$$\mathrm{Re}\left\langle \varphi_i \left| \Sigma_{xc}\left(E_i - i\eta_i\gamma_i\right) \right| \varphi_i \right\rangle - \left\langle \varphi_i \left| V_{xc} \right| \varphi_i \right\rangle = E_i - \varepsilon_i \tag{6.2a}$$

$$\left| \mathrm{Im}\left\langle \varphi_i \left| \Sigma_{xc}\left(E_i - i\eta_i\gamma_i\right) \right| \varphi_i \right\rangle \right| = \gamma_i \tag{6.2b}$$

The inelastic scattering rates of excitons are calculated with the approximation method developed in Chap. 3

$$\Gamma_s = \sum_{v,c} \left| R_s^{vc} \right|^2 \left(\gamma_c + \gamma_v\right) \tag{6.3}$$

where R_s^{vc} are the coefficients of the linear combination of the sth exciton obtained by TDLDA, namely

$$\rho_s(\mathbf{r}) = \sum_{v,c} R_s^{vc} \varphi_v^*(\mathbf{r}) \varphi_c(\mathbf{r}) \tag{6.4}$$

Following the methods in Chap. 4, the single-phonon relaxation rates of electrons are calculated by

$$\gamma_i^{SP} = \sum_{j,|E_j|<|E_i|} \sum_k \frac{\hbar^2}{M_k} \left| C_k^{ij} \right|^2 \hbar\omega_k \left[\frac{\left(n_k + 1\right)\gamma_i^{SP}}{\left(\Delta E_{ij} - \hbar\omega_k\right)^2 + \left(\gamma_i^{SP}\right)^2} + \frac{n_k \gamma_i^{SP}}{\left(\Delta E_{ij} + \hbar\omega_k\right)^2 + \left(\gamma_i^{SP}\right)^2} \right] \tag{6.5}$$

where M_k are the masses of the normal coordinates Q_k, while $C_k^{i,j} = \left\langle \varphi_j \left| \partial / \partial Q_k \right| \varphi_i \right\rangle$, and $\Delta E_{ij} = E_i - E_j$. γ_i^{SP} is the width of the Lorentzian function corresponding to the ith electron, which is exactly the single-phonon decay rate to be determined. The multiple-phonon relaxation rates of electrons are evaluated as

$$\gamma_i^{MP} = \sum_{j,|E_j|<|E_i|} \sum_k \frac{\hbar^2}{M_k} \left| C_k^{ij} \right|^2 \hbar\omega_k \pi \frac{1}{\hbar D_{ij}^k \sqrt{2\pi}} \left(\begin{array}{l} \left(n_k + 1\right) \exp\left(-\dfrac{\left(\Delta E_{ij} - \hbar\omega_k\right)^2}{2\hbar^2 \left(D_{ij}^k\right)^2} \right) \\ + n_k \exp\left(-\dfrac{\left(\Delta E_{ij} + \hbar\omega_k\right)^2}{2\hbar^2 \left(D_{ij}^k\right)^2} \right) \end{array} \right) \tag{6.6}$$

with

$$\left(D_{ij}^{k}\right)^{2}=\frac{1}{2}\sum_{k}\omega_{k}^{2}\left(\Delta_{k}^{ij}\right)^{2}\left(2n_{k}+1\right)$$

$$n_{k}=\frac{1}{\exp\left(\hbar\omega_{k}/k_{B}T\right)-1}$$

For excitonic states,

$$C_{k}^{i,j}=\left\langle\rho_{j}\left|\partial/\partial Q_{k}\right|\rho_{i}\right\rangle=\sum_{v,c}\sum_{v',c'}R_{vc}^{i}R_{v'c'}^{j}\left(\delta_{vv'}\left\langle\varphi_{c}\left|\partial/\partial Q_{k}\right|\varphi_{c'}\right\rangle+\delta_{cc'}\left\langle\varphi_{v}\left|\partial/\partial Q_{k}\right|\varphi_{v'}\right\rangle\right) \quad (6.7)$$

for valence and conducton band constituent states v and c.

6.3 Results and discussions

As the electronic density of states of Por and ZnPorFCl are very low and discontinuous, we only discuss the excitonic density of states of these two compounds. The absorption spectra of Por and ZnPorFCl are given in Fig. 6-3a, where we can see that the absorption spectra of the two compounds only slightly differ in terms of the positions and strengths of the major peaks in these spectra, which can be attributed to the similarity of the structures of the two compounds. The excitonic DOSs of the two compounds are plotted in Fig. 6-3b. It can be seen that the excitonic DOS of ZnPorFCl is larger than that of Por, as there are more valence electrons in ZnPorFCl.

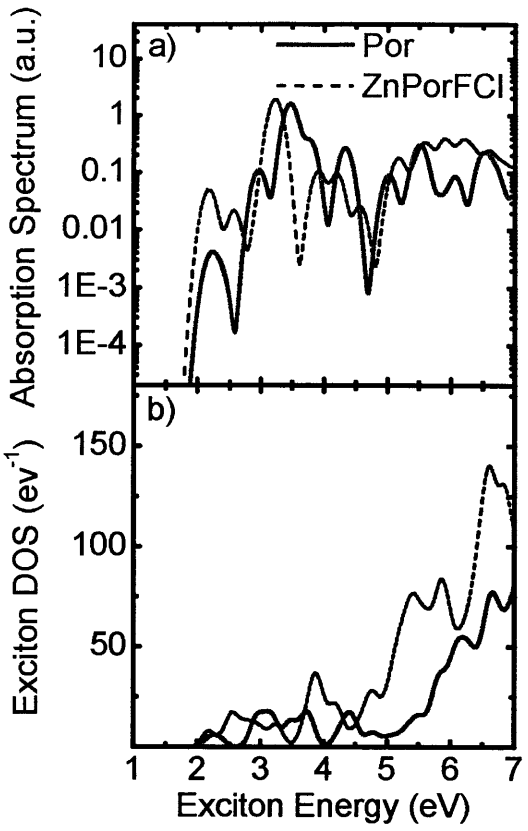

Figure 6-3. a) Absorption spectra and b) excitonic DOSs of Por and ZnPorFCl plotted vs. exciton energy.

The single-phonon nonradiative relaxation rates Γ^{SP} of excitons in Por and ZnPorFCl at 0 K obtained by Eq. (6.5) are plotted versus the excitation energy Ω_s in Figs. 6-4a and 6-4b. The multiple-phonon nonradiative relaxation rates Γ^{MP} of excitons in these three clusters at 0 K are plotted in Figs. 6-4c to 6-4d. It can be seen that the patterns of Γ^{SP} and Γ^{MP} for the two compounds are even more dispersive than those of Si_{46} (Fig. 4-9) and $(PbX)_{36}$ (Fig. 5-9). This is attributed to the fact that the excitonic DOSs of the two organic compounds are smaller and less regular than those for the inorganic quantum dots. In spite of the large data dispersion, the values of Γ^{SP} and Γ^{MP} for ZnPorFCl are found to be lower than those for Por, especially in the high-energy regime where nonradiative relaxation are close to be saturated. The results thus further demonstrate the concept of reducing the electron-phonon interaction by the valence-electron-separation effect.

The temperature effect on the relaxation rates has also been investigated by recalculating Γ^{SP} and Γ^{MP} for the excitons in the two compounds at 300 K. The results are given in Figs. 6-5a to 6-5d. Being different from Si_{46} and $(PbX)_{36}$, the Γ^{SP} and Γ^{MP} of the two compounds are not sensitive to the temperature. Increasing the temperature from 0 to 300 K has negligible effect on nonradiative relaxation rates. This is attributed to the higher phonon frequencies of the two organic structures compared to those of inorganic nanoclusters. Thus the occupation numbers of most phonon modes still remain 0 at 300 K.

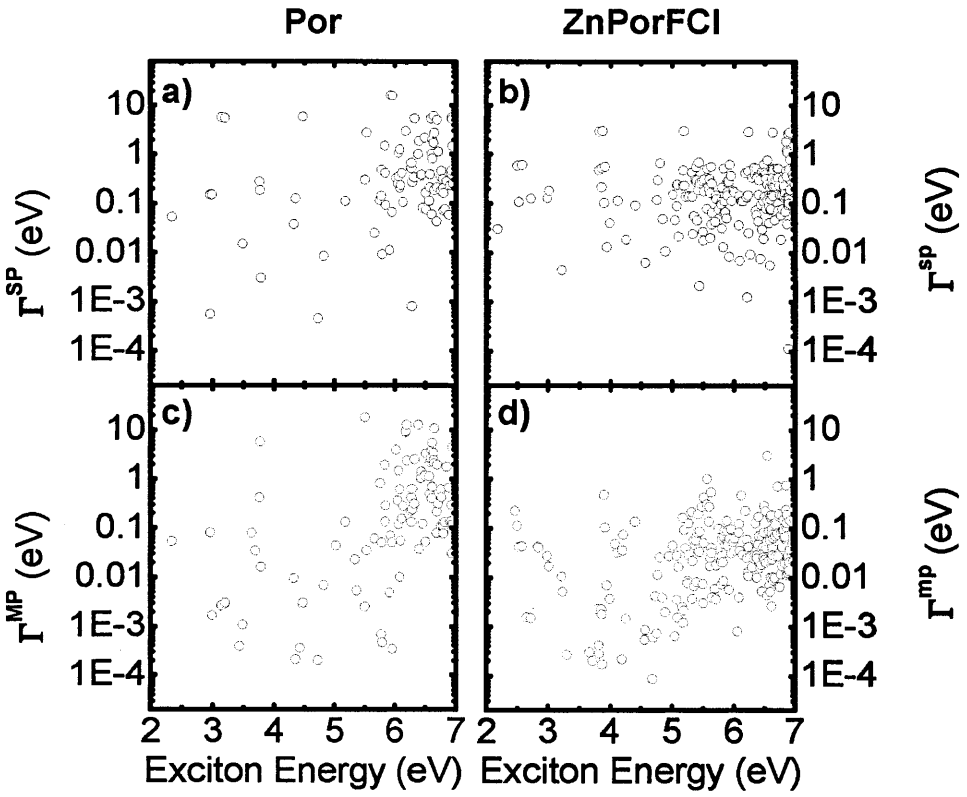

Figure 6-4. Single-phonon nonradiative relaxation rates Γ^{SP} of excitons as a function of exciton energy at 0 K in a) Por and b) ZnPorFCl. Multiple-phonon nonradiative relaxation rates Γ^{MP} of excitons as a function of exciton energy at 0 K in c) Por and d) ZnPorFCl.

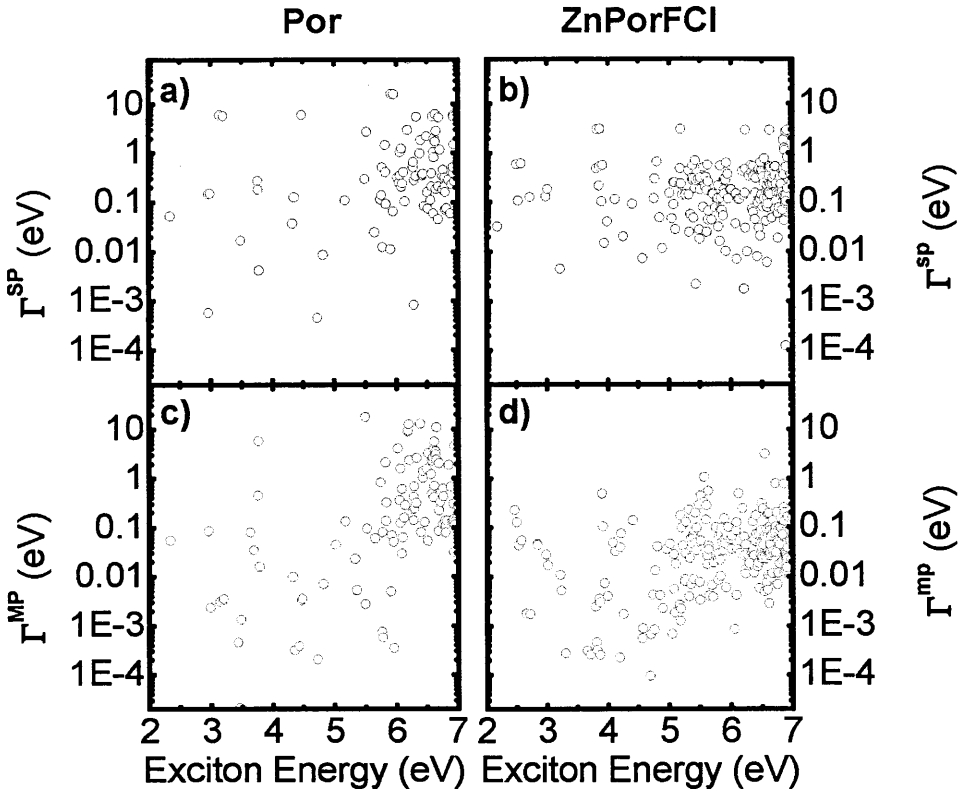

Figure 6-5. Single-phonon nonradiative relaxation rates Γ^{SP} of excitons as a function of exciton energy at 300 K in a) Por and b) ZnPorFCl. Multiple-phonon nonradiative relaxation rates Γ^{MP} of excitons as a function of exciton energy at 300 K in c) Por and d) ZnPorFCl.

The phonon DOSs of Por and ZnPorFCl are plotted vs. wavenumber in Figs. 6-6a and 6-6b. The two type of spectra exhibit significant differences in the high-frequency regime. As shown in Fig. 6-6a, Por has two groups of vibrational peaks in the high-frequency regime (> 3000 cm^{-1}), the left one is for the in-plane stretch modes of the side H atoms, the right one is for in-plane stretch modes of the center H atoms. With the H atoms being replaced by heavier atoms, these peaks shift to the low-frequency regime, as shown in Fig. 6-6b. This is due to the mass effect discussed in Chap. 5. The effect, in principle, suppresses the single-phonon process due to the fewer excitonic states available for single-phonon decay pathway. However, relatively large excitonic DOS of ZnPorFCl will enhance the single-phonon process by providing more excitonic states per unit energy range. This means that the effects of

the reduced phonon frequencies and increased excitonic DOS are opposite to each other. Thus the reduction of Γ^{SP} is mostly attributed to the valence-electron-separation effect, which is the only possible reason for the reduction of Γ^{MP}.

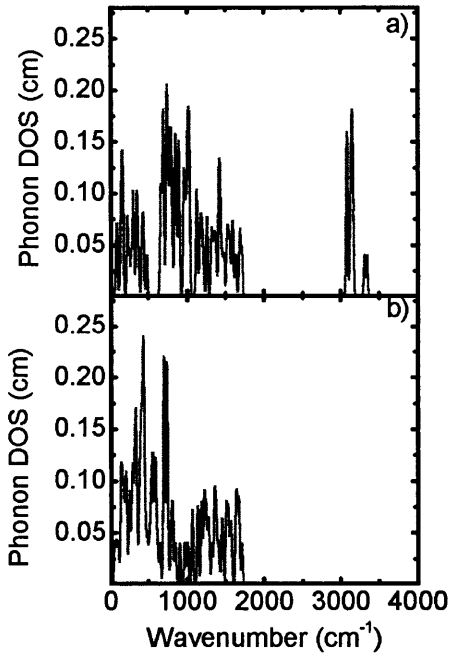

Figure 6-6. Phonon DOSs of a) Por and b) ZnPorFCl as a function of wavenumber.

The inelastic scattering rates Γ^{IS} of excitons in Por and ZnPorFCl calculated by the approximation method Eq. (6.3) are plotted versus the excitation energy Ω in Figs. 6-7a to 6-7b. Both patterns are very dispersive. Excitons with close exciton energies may have Γ^{IS} varying over three orders of magnitude, which are quite different from those of Si_{46} (Fig. 4-7) and $(PbX)_{36}$ (Fig. 5-8). No curve-fitting can be made, but qualitatively, the inelastic scattering relaxation dynamics in the two compounds are close to each other.

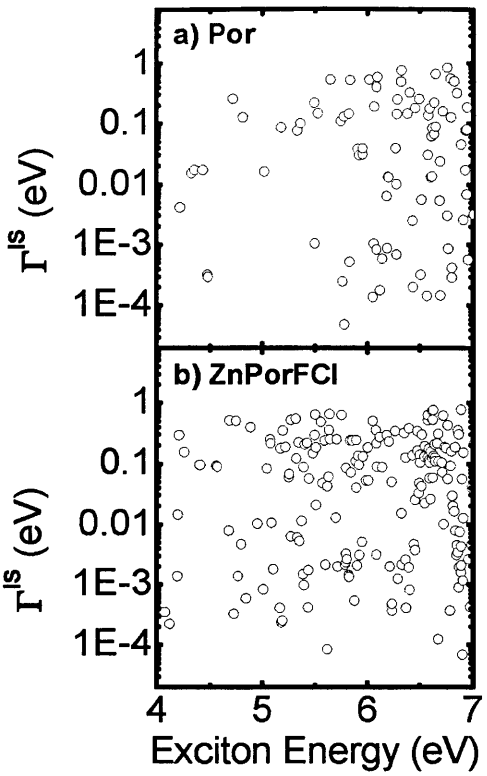

Figure 6-7. Inelastic scattering rates Γ^{IS} of excitons in a) Por and b) ZnPorFCl as a function of exciton energy.

6.4 Conclusion

Excitonic nonradiative relaxation rates in a porphyrin molecule and in a porphyrin derivative have been calculated by the numerical methods developed in Chap. 4. Our simulation results show that the excitonic nonradiative relaxation rates in a porphyrin derivative with heavier atoms are lower than those in a porphyrin molecule. The results here further demonstrate the strategy proposed in Chap. 5 that the exciton-phonon interaction can be reduced by pushing the valence electrons away from the nuclei with more core electrons being contained in heavier atoms.

Chapter 7

Summary

The dynamics of electrons and excitons in semiconducting nanoclusters are of increasing interest and importance, owing to their various applications or potential applications for solar energy harvesting, such as in multiple exciton generation and hot-electron capture. Although the theories and numerical approaches for bulk semiconductors have been long established, the theoretical research and computational research focusing on semiconductor nanoclusters are much less developed. For some important physical processes, even the calculation methods have not been well established. Thus it becomes urgent to build up a comprehensive theoretical tool kit covering the two important physics issues, namely the dynamic properties of the electrons and excitons and their interaction with phonons.

In chapters 2, 3 and 4, the computational approaches and methods for each processes are developed. In chapter 2, the numerical implementations for the calculation of the electronic inelastic scattering rates in nanoclusters are developed based on the many-body Green's function theory. In chapter 3, a computational approach and strategy for the calculation of the excitonic inelastic scattering rates in nanoclusters is developed. This strategy simplifies the calculation effectively, and augments the capability of computational resources significantly, which is demonstrated by some computational tasks that are essentially infeasible without these simplifications. In chapter 4, a method or strategy is developed to include both the single-phonon and the multiple-phonon nonradiative relaxation mechanisms for the nonradiative relaxation rates of the electronic and excitonic states in nanoclusters. We demonstrate that the nonradiative relaxation of one-particle states and two-particle states are strictly,distinctive due to the significant difference between the DOSs of one-particle states and two-particle states.

In chapters 5 and 6, a strategy is proposed to reduce the electron-phonon coupling in nanoclusters by pushing the valence electron away from the nuclei with the core electrons in heavy atoms. With the methods developed in Chaps. 2-4, the strategy is demonstrated with the numerical simulations of lead chalcogenide nano clusters, and is further demonstrated with the numerical simulations of the porphyrin molecule and a porphyrin derivative.

The strategy proposed in Chaps. 5 and 6 may some day be applied to build photovoltaics such as multi exciton generation (MEG) systems with higher efficiencies. More broadly, the methods developed in Chaps. 2-4 are very fundamental and they shall benefit more areas and applications involving photons, electrons, excitons and phonons in zero-dimensional materials.

Bibliography

[1] S. Gunes, H. Neugebauer, and N. S. Sariciftci, Chem. Rev. 107, 1324 (2007).

[2] X. Chen and S. S. Mao, Chem. Rev. 107, 2891 (2007).

[3] P. V. Kamat, J. Phys. Chem. C 112, 18737 (2008).

[4] W. Shockley and H. J. Queisser, *J. Appl. Phys.* **32**, 510 (1961).

[5] O. D. Miller, E. Yablonovitch, S. R. Kurtz, arXiv:1106.1603v3.

[6] R. R. King, D. C. Law, K. M. Edmondson, C. M. Fetzer, G. S. Kinsey, H. Yoon, R. A. Sherif, and N. H. Karam, Appl. Phys. Lett. 90, 183516 (2007).

[7] A. J. Nozik, *Physica E* **14**, 115 (2002).

[8] W. A. Tisdale, K. J. Williams, B. A. Timp, D. J. Norris, E. S. Aydil, and X.-Y. Zhu, *Science* **328**, 1543 (2010).

[9] L. A. Padilha, I. Robel, D. C. Lee, P. Nagpal, J. M. Pietryga, and V. I. Klimov, *ACS Nano* **5**, 5045 (2011).

[10] O. E. Semonin, J. M. Luther, S. Choi, H.-Y. Chen, J. Gao, A. J. Nozik and M. C. Beard, *Science* **3334**, 1530 (2011).

[11] R. J. Ellingson, M. C. Beard, J. C. Johnson, P. Yu, O. I. Micic, A. J. Nozik, A. Shabaev, and A. L. Efros, *Nano Lett.* **5**, 865 (2005).

[12] H. Petek and S. Ogawa, *Prog. Surf. Sci.* **56**, 239 (1997).

[13] J. Bokor, *Science* **246**, 1130 (1989).

[14] P. M. Echenique, J. M. Pitarke, E. V. Chulkov, and A. Rubio, *Chem. Phys.* **251**, 1 (2000).

[15] E. V. Chulkov, A. G. Borisov, J. P. Gauyacq, D. Sanchez-Portal, V. M. Silkin, V. P. Zhukov, and P. M. Echenique, *Chem. Rev.* **106**, 415 (2006).

[16] W. A. de Heer, *Rev. Mod. Phys.* **65**, 611 (1993).

[17] C. Voisin, D. Christofilos, N. Del Fatti, F. Vallee, B. Prevel, E. Cottancin, J. Lerme, M. Pellarin, and M. Broyer, *Phys. Rev. Lett.* **85**, 2200 (2000).

[18] R. M. Martin, *Electronic Structure, Basic Theory and Practical Methods* (Cambridge University Press, Cambridge, 2004).

[19] J. J. Quinn and R. A. Ferrell, *Phys. Rev.* **112**, 812 (1958).

[20] L. Hedin, *Phys. Rev.* **139**, A796 (1965).

[21] W. G. Aulbur, L. Jonsson, and J.W.Wilkins, in *Solid State Physics*, edited by F. Seitz, D. Turnbull, and H. Ehrenreich (Academic, New York, 2000), Vol. 54, p. 1.

[22] F. Aryasetiawan and O. Gunnarsson, *Rep. Prog. Phys.* **61**, 237 (1998).

[23] M. S. Hybertsen and S. G. Louie, *Phys. Rev. B* **34**, 5390 (1986).

[24] R.W. Godby, M. Schluter, and L. J. Sham, *Phys. Rev. B* **37**, 10159 (1988).

[25] P. E. Trevisanutto, C. Giorgetti, L. Reining, M. Ladisa, and V. Olevano, *Phys. Rev. Lett.* **101**, 226405 (2008).

[26] C. H. Park, F. Giustino, M. L. Cohen, and S. G. Louie, *Phys. Rev. Lett.* **99**, 086804 (2007).

[27] R. Saito, M. Hofmann, G. Dresselhaus, A. Jorio, and M. S. Dresselhaus, *Adv. Phys.* **60**, 413 (2011).

[28] M. Quijada, R. D´ıez Muino, A. G. Borisov, J. A. Alonso, and P. M. Echenique, *New J. Phys.* **12**, 053023 (2010).

[29] A. L. Fetter and J. D. Walecka, *Quantum Theory of Many-Particle Systems* (McGraw-Hill, New York, 1971).

[30] G. D. Mahan, *Many-Particle Physics*, 3rd ed. (Kluwer/Plenum, New York, 2000).

[31] M. E. Casida, in *Recent Advances in Density-Functional Methods, Part I*, edited by D. P. Chong (World Scientific, Singapore, 1995), p. 155.

[32] R. Del Sole, L. Reining, and R. W. Godby, *Phys. Rev. B* **49**, 8024 (1994).

[33] M. L. Tiago and J. R. Chelikowsky, *Phys. Rev. B* **73**, 205334 (2006).

[35] J. M. Soler, E. Artacho, J. D. Gale, A. Garcia, J. Junquera, P. Ordejon, and D. Sanchez-Portal, *J. Phys. Condens. Matter* **14**, 2745 (2002).

[36] N. Troullier and J. L. Martins, *Phys. Rev. B* **43**, 1993 (1991).

[37] U. Trottenberg, C. W. Oosterlee, and A. Schuller, *Multigrid* (Academic, San Diego, 2001).

[38] B. Holm and U. von Barth, *Phys. Rev. B* **57**, 2108 (1998).

[39] O. C. Thomas, W. J. Zheng, S. J. Xu, and K. H. Bowen, *Phys. Rev. Lett.* **89**, 213403 (2002).

[40] J. Jellinek and P. H. Acioli, *J. Phys. Chem.* A **106**, 10919 (2002).

[41] I. Campillo, V. M. Silkin, J. M. Pitarke, E. V. Chulkov, A. Rubio, and P. M. Echenique, *Phys. Rev. B* **61**, 13484 (2000).

[42] I. Campillo, A. Rubio, J. M. Pitarke, A. Goldmann, and P. M. Echenique, *Phys. Rev. Lett.* **85**, 3241 (2000).

[43] Z. J. Yi, Y. C. Ma, M. Rohlfing, V. M. Silkin, and E. V. Chulkov, *Phys. Rev. B* **81**, 125125 (2010).

[44] R. D. Schaller and V. I. Klimov, *Phys. Rev. Lett.* **92**, 186601 (2004).

[45] M. C. Beard, K. P. Knutsen, P. Yu, J. M. Luther, Q. Song, W. K. Metzger, R. J. Ellingson, andA. J.Nozik, *Nano Lett.* 7, 2506 (2007).

[46] G. Nair, L. Y. Chang, S. M. Geyer, and M. G. Bawendi, *Nano Lett.* **11**, 2145 (2011).

[47] M. T. Trinh, A. J. Houtepen, J. M. Schins, T. Hanrath, J. Piris, W. Knulst, A. P. L. M. Goossens, and L. D. A. Siebbeles, *Nano Lett.* **8**, 1713 (2008).

[48] G. Onida, L. Reining, and A. Rubio, *Rev. Mod. Phys.* **74**, 601 (2002).

[49] M. Rohlfing and S. G. Louie, *Phys. Rev. B* **62**, 4927 (2000).

[50] G. Strinati, Riv. *Nuovo Cimento* **11**, 1 (1988).

[51] L. X. Benedict, A. Puzder, A. J. Williamson, J. C. Grossman, G. Galli, J. E. Klepeis, J.-Y. Raty, and O. Pankratov, *Phys. Rev. B* **68**, 085310 (2003).

[52] M. Lopez del Puerto, M. L. Tiago, and J. R. Chelikowsky, *Phys. Rev. B* **77**, 045404 (2008).

[53] C. Csanak, H. S. Taylor, and R. Yaris, *Adv. At. Mol. Phys.* **7**, 287 (1971).

[54] G. Strinati, *Phys. Rev. B* **29**, 5718 (1984).

[55] I.Rata, A. A. Shvartsburg, M. Horoi, T. Frauenheim, K.W. Michael Siu, and K. A. Jackson, *Phys. Rev. Lett.* **85**, 546 (2000).

[56] S. Yoo and X. C. Zeng, *J. Chem. Phys.* **123**, 164303 (2005).

[57] L. Mitas, J. C. Grossman, I. Stich, and J. Tobik, *Phys. Rev. Lett.* **84**, 1479 (2000).

[58] Y. He and T. F. Zeng, *Phys. Rev. B* **84**, 035456 (2011).

[59] M. Rohlfing and S. G. Louie, *Phys. Rev. Lett.* **80**, 3320 (1998).

[60] K. Fuke, K. Tsukamoto, F. Misaizu, and M. Sane, *J. Chem. Phys.* **99**, 7807 (1993).

[61] A. Fleszar and W. Hanke, *Phys. Rev. B* **56**, 10228 (1997).

[62] B. Arnaud, S. Lebegue, and M. Alouani, *Phys. Rev. B* **71**, 035308 (2005).

[63] R. Laskowski, N. E. Christensen, G Santi, and C. Ambrosch-Draxl, *Phys. Rev. B* **72**, 035204 (2005).

[64] M. Rohlfing and S. G Louie, *Phys. Rev. Lett.* **81**, 2312 (1998).

[65] L. Yang, J. Deslippe, C.-H. Park, M. L. Cohen, and S. G Louie, *Phys. Rev. Lett.* **103**, 186802 (2009).

[66] P. E. Trevisanutto, M. Holzmann, M. Cote, and V. Olevano, *Phys. Rev. B* **81**, 121405(R) (2010).

[67] M. Dresselhaus, G Dresselhaus, R. Saito, and A. Jorio, *Annu. Rev. Phys. Chem.* **58**, 719 (2007).

[68] C.-H. Park, C. D. Spataru, and S. G Louie, *Phys. Rev. Lett.* **96**, 126105 (2006).

[69] M. Rohlfing and S. G. Louie, *Phys. Rev. Lett.* **80**, 3320 (1998).

[70] Y. Ma, M. Rohlfing, C. Molteni, and E. M. Gonzalez, *J. Chem. Theory Comput.* **6**, 257 (2010).

[71] H. Y. Fan, *Phys. Rev.* **82**, 900 (1951).

[72] M. Cardona, *Solid State Commun.* **133**, 3 (2005).

[73] S. H. Lin, *J. Chem. Phys.* **44**, 3759 (1966).

[74] K. F. Freed and J. Jortner, *J. Chem. Phys.* **52**, 6272 (1970).

[75] M. Born and R. Oppenheimer, *Ann. Physik* **84**, 457 (1927).

[76] K. Huang and A. Rhys, *Proc. Roy. Soc.* **A204**, 406 (1950).

[77] R. Kubo, *Phys. Rev.* **86**, 929 (1952).

[78] M. Lax, *J. Chem. Phys.* **20**, 1752 (1952).

[79] M. Bixon and J. Jortner, *J. Chem. Phys.* **48**, 715 (1968).

[80] R. Englman and J. Jortner, *Mol. Phys.* **18**, 145 (1970).

[81] E. B. Wilson, Jr., J. C. Decius, and P. C. Cross, *Molecular Vibrations: The Theory of Infrared and Raman Vibrational Spectra* (Dover, New York, NY 1980).

[82] S. V. Kilina, D. S. Kilin, and O. V. Prezhdo, *ACS Nano* **3**, 93 (2009).